

Calculations of multi-particle processes at the one-loop level: precise predictions for the LHC

Dissertation zur Erlangung des
naturwissenschaftlichen Doktorgrades
der Julius-Maximilians-Universität Würzburg

vorgelegt von
Stefan Karg
aus Neumarkt

Würzburg 2007

Eingereicht am: 28. September 2007
bei der Fakultät für Physik und Astronomie

1. Gutachter: Prof. Dr. Reinhold Rückl
2. Gutachter: Prof. Dr. Thomas Trefzger
der Dissertation.

1. Prüfer: Prof. Dr. Reinhold Rückl
2. Prüfer: Prof. Dr. Thomas Trefzger
3. Prüfer: Prof. Dr. Carsten Honerkamp
im Promotionskolloquium.

Tag des Promotionskolloquiums: 14. Mai 2008

Doktorurkunde ausgehändigt am:

Abstract

The Standard Model (SM) of elementary particle physics provides a uniform framework for the description of three fundamental forces, the electromagnetic and weak forces, describing interactions between quarks and leptons, and the strong force, describing a much stronger interaction between the coloured quarks. Numerous experimental tests have been performed in the last thirty years, showing a spectacular agreement with the theoretical predictions of the Standard Model, even at the per mille level, therefore validating the model at the quantum level. An important cornerstone of the Standard Model is the Higgs mechanism, which provides a possible explanation of electroweak symmetry breaking, responsible for the masses of elementary fermions and the W and Z bosons, the carriers of the weak force. This mechanism predicts a scalar boson, the Higgs boson, which has escaped its discovery so far. If the Higgs mechanism is indeed realised in nature, the upcoming Large Hadron Collider (LHC) at CERN will be able to find the associated Higgs boson. The discovery of a Higgs boson by itself is not sufficient to establish the Higgs mechanism, the basic ingredient being the Higgs potential which predicts trilinear and quartic couplings. These have to be confirmed experimentally by the study of multi-Higgs production.

We therefore present a calculation of the loop-induced processes $gg \rightarrow HH$ and $gg \rightarrow HHH$, and investigate the observability of multi-Higgs boson production at the LHC in the Standard Model and beyond. While the SM cross sections are too small to allow observation at the LHC, we demonstrate that physics beyond the SM can lead to amplified, observable cross sections. Furthermore, the applicability of the heavy top quark approximation in two- and three-Higgs boson production is investigated. We conclude that multi-Higgs boson production at the SuperLHC is an interesting probe of Higgs sectors beyond the SM and warrants further study.

Despite the great success of the SM, it is widely believed that this model cannot be valid for arbitrarily high energies. The LHC will probe the TeV scale and theoretical arguments indicate the appearance of physics beyond the SM at this scale. The search for new physics requires a precise understanding of the SM. Precise theoretical predictions are needed which match the accuracy of the experiments. For the LHC, most analyses require next-to-leading order (NLO) precision. Only then will we be able to reliably verify or falsify different models. At the LHC, many interesting signatures involve more than two particles in the final state. Precise theoretical predictions for

such multi-leg processes are a highly nontrivial task and new efficient methods have to be applied.

The calculation of the process $PP \rightarrow VV + \text{jet}$ at NLO is an important background process to Higgs production in association with a jet at the LHC. We compute the virtual corrections to this process which form the “bottleneck” for obtaining a complete NLO prediction. The resulting analytic expressions are generated with highly automated computer routines and translated into a flexible Fortran code, which can be employed in the computation of differential cross sections of phenomenological interest. The obtained results for the virtual corrections indicate that the QCD corrections are sizable and should be taken into account in experimental studies for the LHC.

Zusammenfassung

Das Standardmodell der Teilchenphysik bietet einen einheitlichen Rahmen zur Beschreibung dreier fundamentaler Kräfte. Die elektromagnetische und schwache Kraft beschreibt die Wechselwirkung zwischen Quarks und Leptonen, während die weit stärkere starke Kraft nur auf die farbgeladenen Quarks wirkt. Die zahlreichen experimentellen Tests, die in den vergangenen 30 Jahren durchgeführt wurden, sind in spektakulärer Übereinstimmung mit den theoretischen Vorhersagen des Standardmodells, sogar auf dem pro mille Niveau und bestätigen damit das Modell auf dem Quantenniveau. Ein Grundpfeiler des Standardmodells ist der Higgsmechanismus, der eine mögliche Erklärung für die elektro-schwache Symmetriebrechung liefert, die verantwortlich ist für die beobachteten Massen elementarer Fermionen und der W und Z Bosonen, den Trägern der schwachen Kraft. Dieser Mechanismus sagt ein skalares Boson, das Higgs Boson, voraus, das bisher noch nicht entdeckt wurde. Falls dieser Mechanismus wirklich in der Natur realisiert ist, wird der Large Hadron Collider (LHC) am CERN in der Lage sein, das zugehörige Higgs Boson zu entdecken. Die Entdeckung des Higgs Bosons für sich alleine gestellt reicht nicht aus, um den Higgsmechanismus zu etablieren, dessen zentraler Bestandteil das Higgspotential ist, welches trilineare und quartische Selbstkopplungen vorhersagt. Diese müssen im Experiment durch die Analyse von multipler Higgsproduktion bestätigt werden.

Wir präsentieren daher die Berechnung der schleifen-induzierten Prozesse $gg \rightarrow HH$ und $gg \rightarrow HHH$ und untersuchen die Observierbarkeit von multipler Higgsproduktion am LHC im Rahmen des Standardmodells und darüber hinaus. Da die Standardmodell-Wirkungsquerschnitte zu klein sind, um die Produktion von drei Higgs Bosonen am LHC zu beobachten, zeigen wir, dass Physik jenseits des Standardmodells zu verstärkten und damit beobachtbaren Wirkungsquerschnitten führen kann. Darüber hinaus wird die Anwendbarkeit der Näherung eines schweren top Quarks auf die Produktion von zwei und drei Higgs Bosonen untersucht. Wir kommen zu dem Schluss, dass multiple Higgsproduktion am Super-LHC eine interessante Sonde des Higgs Sektors ist und weitere Untersuchungen rechtfertigt.

Trotz des großartigen Erfolgs des Standardmodells wird weithin vermutet, dass dieses Modell seine Gültigkeit nicht bis zu beliebig hohen Energieskalen behält. Theoretische Argumente deuten auf Anzeichen neuer Physik jenseits des Standardmodells auf der TeV Skala hin, die der LHC untersuchen wird. Die Suche nach neuer Physik erfordert ein detailliertes Verständnis des Standardmodells. Präzise theoretische

Vorhersagen sind nötig, die der experimentellen Genauigkeit der Experimente entsprechen. Für den LHC sind die meisten Analysen in nächst-führender Ordnung (NLO) erforderlich. Nur dann werden wir verlässlich erweiterte Modelle bestätigen oder falsifizieren können. Am LHC sind viele interessante Signaturen verknüpft mit Endzuständen, die mehr als zwei Teilchen beinhalten. Präzise theoretische Vorhersagen für solche Multiple-Teilchen-Prozesse stellen eine sehr große Herausforderung dar, für die neue und effiziente Methoden verwendet werden müssen.

Die Berechnung des Prozesses $PP \rightarrow VV + \text{jet}$ in nächst-führender Ordnung ist ein wichtiger Hintergrundprozess für die Higgsproduktion in Assoziation mit einem Jet am LHC. Wir berechnen die virtuellen Korrekturen zu diesem Prozess, welche die größte Schwierigkeit darstellt, eine Vorhersage mit NLO Präzision zu erhalten. Die resultierenden analytischen Ausdrücke wurden weitgehend automatisiert erzeugt und in einen flexiblen Fortran Code übersetzt, der für die Berechnung von totalen und differentiellen Wirkungsquerschnitten von phänomenologischem Interesse verwendet werden kann. Die erzielten Ergebnisse für die virtuellen Korrekturen deuten auf große QCD Korrekturen hin, die in experimentellen Studien für den LHC berücksichtigt werden sollten.

Contents

1	Introduction	1
2	Higgs Physics at the LHC	5
2.1	Higgs mechanism	5
2.2	Higgs mass constraints	10
2.2.1	Perturbative Unitarity	11
2.2.2	Triviality and vacuum stability	13
2.2.3	Experimental constraints	14
2.3	Higgs Bosons at Hadron Colliders	17
2.3.1	Higgs boson production	17
2.3.2	Higgs boson decay	19
2.3.3	Search strategies and backgrounds	22
2.4	Summary	26
3	Hadron collider cross sections	29
3.1	Parton model	30
3.2	Phase space integration	33
3.2.1	Two-particle phase space	35
3.2.2	Three-particle phase space	35
4	Calculation of multi-leg one-loop amplitudes	39
4.1	Quantum number management	39
4.1.1	Spinor Helicity formalism	40
4.1.2	Colour decomposition	44
4.2	Dimensional regularisation and Renormalisation	45
4.3	Reduction method for scalar integrals	49
4.4	Reduction method for tensor integrals	54
4.4.1	Form factor representation for tensor integrals	54
4.4.2	Tensor reduction through recursion relations	54
5	Gluon induced multi-Higgs production	59
5.1	Introduction	59
5.2	Higgs boson properties	60

5.3	Calculation	62
5.3.1	Structure of the amplitude	62
5.3.2	Evaluation of the amplitude coefficients	65
5.3.3	Numerical implementation	66
5.4	Results	66
5.4.1	Multi-Higgs boson production in the SM	67
5.4.2	Quality of the heavy-top approximation	70
5.4.3	Multi-Higgs boson production beyond the SM	71
5.5	Summary	75
6	NLO QCD Cross section for $PP \rightarrow VV + \text{jet}$	79
6.1	Introduction	79
6.2	Amplitude organisation	80
6.3	Checks of the calculation	85
6.4	Results from the virtual contribution	85
6.4.1	Total cross sections	86
6.4.2	Distributions	86
7	Summary	95
A	Analytical evaluation of a one-loop scalar integral	99
B	Feynman diagrams for $q\bar{q} \rightarrow ZZg$	107
	Bibliography	111

List of Figures

2.1	Higgs potential	7
2.2	Feynman diagrams for $W^+ + W^- \rightarrow W^+ + W^-$	11
2.3	Triviality vacuum stability bound on the SM Higgs boson mass	14
2.4	The production mechanism for SM Higgs bosons in e^+e^- collisions	15
2.5	$\Delta\chi^2$ of the fit to the electroweak precision data as a function of M_H	16
2.6	Feynman diagrams of the four dominant Higgs production channels	18
2.7	LO production cross sections for a SM Higgs boson as a function of the Higgs boson mass at the LHC	19
2.8	Gluon fusion production cross section for a SM Higgs boson at the LHC with higher order QCD corrections	20
2.9	$t\bar{t}H$ production cross section at the LHC as a function of μ	21
2.10	NLO production cross sections for a SM Higgs boson as a function of the Higgs boson mass at the LHC	22
2.11	SM Higgs decay branching ratios	23
2.12	Decay widths of the SM Higgs boson	23
2.13	ATLAS simulation of $gg \rightarrow H \rightarrow \gamma\gamma$	24
2.14	Tagging jet rapidity and separation for VBF Higgs production vs. $t\bar{t}$ background events	25
2.15	ATLAS simulations of $H \rightarrow WW$ and $q\bar{q}H \rightarrow q\bar{q}WW$ events	26
2.16	ATLAS sensitivity for the discovery of the SM Higgs boson	27
3.1	The parton model description of a hard scattering process	31
3.2	Parton distribution functions	34
4.1	Scalar self-energy	45
4.2	N -point graph	49
4.3	Graphical representation of pinch integrals	51
5.1	Illustration of different topologies to the process $gg \rightarrow HHH$	63
5.2	Total Higgs pair production cross section vs. m_H	67
5.3	Total 3-Higgs boson production cross section vs. m_H	68
5.4	Scale dependence of the $gg \rightarrow HH, HHH$ cross section	69

5.5	Comparison of the total cross section for 2-Higgs and 3-Higgs boson production with the heavy-top approximation	71
5.6	Total cross section for 2-Higgs and 3-Higgs production vs. m_q	71
5.7	Contour plot showing the variation of the cross section with λ_3 and λ_4 for 3-Higgs boson production	72
5.8	Contour plot showing the variation of the cross section with m_H and λ_3 for 3-Higgs boson production	73
5.9	Contour plot showing the variation of the cross section with m_H and λ_3 for 2-Higgs boson production	73
5.10	Variation of the cross section for 3-Higgs boson production with λ_3	74
5.11	Cross section for 3-Higgs boson production vs. m_h in the MSSM	75
5.12	Cross section for 2-Higgs boson production vs. m_h in the MSSM	76
5.13	Normalised Higgs- and Yukawa-couplings of the CP-even MSSM neutral Higgs bosons	78
6.1	Leading order Feynman diagrams for $q\bar{q} \rightarrow ZZg$	81
6.2	Feynman diagrams contributing to the virtual corrections for $q\bar{q} \rightarrow ZZg$	82
6.3	Gluon transverse momentum distribution for $q\bar{q} \rightarrow ZZg$	87
6.4	Transverse momentum distribution for the Z boson	88
6.5	Pseudo-rapidity distribution for the gluon	88
6.6	Pseudo-rapidity distribution for a Z boson	89
6.7	Invariant mass distribution for ZZg	89
6.8	Invariant mass distribution for ZZ	90
6.9	Invariant mass distribution for Zg	90
6.10	Distribution of the distance ΔR_{ZZ}	91
6.11	Distribution of the distance ΔR_{Zg}	91
6.12	Distribution of the azimuthal angle ϕ_{Zg}	92
6.13	Distribution of the polar angle θ_g	92
6.14	Distribution of the polar angle θ_Z	93
A.1	Scalar box integral	99

List of Tables

1.1	Wishlist of desired processes at NLO	4
4.1	Number of tree-level Feynman diagrams contributing to $gg \rightarrow ng$	39
4.2	Definitions of regularisation prescriptions in dimensional regularisation	48
5.1	Cross sections for triple Higgs boson production at the LHC and VLHC	68
5.2	Contributions of different topologies to triple Higgs boson production	69
5.3	Scale dependence of the $gg \rightarrow HHH$ cross section	69
5.4	3-Higgs boson production cross sections for extreme choices of the Higgs couplings	74
6.1	Total cross sections for $q\bar{q} \rightarrow ZZg$	86

Acronyms

EWSB	Electro-weak symmetry breaking
V_{ev}	Vacuum expectation value
LHC	Large Hadron Collider
LO	Leading order
NLO	next-to-leading order
NNLO	next-to-next-to-leading order
SM	Standard Model
SUSY	Supersymmetry
MSSM	Minimal supersymmetric Standard Model
Pdf	Parton distribution function
PP	Proton-proton
$P\bar{P}$	Proton-antiproton
QCD	Quantum Chromodynamics
QED	Quantum Electrodynamics
RGE	Renormalisation Group equation
VBF	Vector boson fusion

1

Introduction

The quest for discovering the fundamental laws of nature and a deeper understanding of the world surrounding us has always been a strong motivation of mankind. Already more than 2500 years ago, Democritos, an ancient greek philosopher, expressed the idea that nature consists of tiny indivisible constituents, the so-called atoms. Only “recently”, in the nineteenth century, has this idea found its revival and has been put into a modern scientific context.

Scientific research has taken us from chemical atoms to electrons and protons, and even smaller substructures, the quarks, which are confined in the proton. Quarks and electrons have a radius smaller than 10^{-18}m and are described as pointlike, indivisible particles. The quest for a deeper understanding of the laws of nature so far has found its culmination in the formulation of the so-called Standard Model of elementary particle physics (SM). According to this model, matter consists of twelve elementary particles, six different quarks and six leptons, like the electron or the electron-neutrino. Their interactions are mediated by three fundamental forces: the electromagnetic force is carried by the exchange of photons, the strong force by gluons, which is responsible for the adhesiveness of the quarks inside the proton, and finally the weak force, mediated by the massive vector bosons W^+ , W^- and Z , e.g. responsible for the fusion of hydrogen atoms to helium atoms in the sun. The much weaker gravitational force is not included, but its effect on elementary particles is negligible. A final ingredient of the Standard Model is the Higgs boson. The associated mechanism, the Higgs mechanism, allows for a consistent treatment of the question why elementary particles have mass in terms of a quantum field theoretical approach. Almost all elementary particles of the Standard Model have been discovered, and all experiments performed in the last thirty years are in excellent agreement with the predictions of the Standard Model. Only one particle has escaped its discovery until now: the Higgs boson. This is one of the main motivations for the construction of the Large Hadron Collider (LHC), a circular particle collider with a circumference of 27 km and a center-of-mass energy of 14 TeV of the colliding protons. The scheduled start of operation is July 2008. If the Higgs boson, responsible for the observed particle masses, is not only a theoretical prejudice, but really exists in nature, the LHC will be able to find

it.

The discovery of a Higgs boson alone is not sufficient to establish the mechanism of mass generation, the so-called Higgs mechanism. All interactions to the other particles of the SM have to be confirmed experimentally, including the trilinear and quartic Higgs self-interactions. The SM prediction for the self-interactions is studied in this thesis and allows in principle to reconstruct the Higgs potential, the basic ingredient of the Higgs mechanism.

Despite the great success of the SM, there are serious doubts that this model is valid for arbitrarily high energies. The gravitational force is not included and cannot be neglected for sufficiently high energies. Astrophysical observations tell us that the largest part of matter is not visible. In the SM, there is no suitable candidate for this “dark matter”. Another open question is the fact that fermions can be grouped in three families, the second and third families being just heavier copies of the first. Since they are unstable, the members of the heavy copies can decay into members of the lightest family. The reason for the existence of these copies is unknown. The most obvious problem of the SM is the asymmetry between anti-matter and matter. Our universe consists only of matter, but in the SM anti-matter and matter are treated on the same footing, up to small effects. It is not clear if these are sufficient to explain the observed asymmetry. These and further problems indicate that the SM is only an intermediate step towards a more fundamental theory, and there is no lack of speculative models beyond the SM. Experimental data so far do not give conclusive hints of how such a theory should look like. The LHC will hopefully improve this situation.

The search for new physics requires a precise understanding of the SM. Precise theoretical predictions are needed which match the accuracy of the experiments. For the LHC, most analyses require next-to-leading order (NLO) precision. Only then will we be able to reliably verify or falsify different models. At the LHC, many interesting signatures involve more than two particles in the final state. Theoretical predictions at NLO for such processes is a highly nontrivial task. Divergences from tree Feynman diagrams with an additional massless particle and from loop diagrams appear and only the merging of these divergences leads to a finite result. Complicated self-interactions, a factorial growth of Feynman diagrams and more kinematic invariants for a higher number of final particles lead to arbitrarily complicated expressions. In addition, spurious numerical instabilities appear in the calculation of loop diagrams which can spoil the convergence of a Monte-Carlo integration. New methods have to be applied to overcome these problems.

This thesis is organised as follows: In chapter 2, we review the Higgs mechanism of the SM. We discuss theoretical and experimental constraints on the mass of the Higgs boson, indicating that its discovery is in the reach of the LHC. We briefly review the production and the decay modes of the Higgs boson at the LHC.

Chapter 3 deals with the calculation of hadronic cross sections. The underlying theory, the parton model is briefly introduced. The modifications needed for comput-

ing cross sections at NLO precision are discussed and explicit formulae are given. The parametrisation of the two- and three-particle phase space integrals is shown, as it is used for the scattering processes considered in this thesis.

In chapter 4 we introduce in detail the techniques used for the calculation of one-loop matrix elements. The spinor helicity formalism and the colour decomposition, applicable also at leading order, allow for an efficient decomposition of the transition amplitude into simpler, gauge-invariant pieces, which helps to keep the size of intermediate expressions under control. At the loop level, a conceptual and technical difficulty appears. Loop diagrams are in general divergent. These divergences have to be regularised, e.g. by dimensional regularisation. Subsequently, a redefinition of the original parameters, a renormalisation, is needed. Different prescriptions within dimensional regularisation are described. The last two sections introduce a reduction formalism for one-loop multi-leg integrals, which has the potential to circumvent the deficiencies of standard reduction algorithms.

In chapter 5 we apply this new reduction technique to the loop-induced process $gg \rightarrow HH$ and $gg \rightarrow HHH$. We investigate the observability of multi-Higgs production at the LHC in the Standard Model and beyond. These processes probe the trilinear and quartic Higgs self-couplings which are needed to establish the Higgs mechanism and to confirm the Higgs sector of the Standard Model. Furthermore, the applicability of the heavy-top approximation is studied for multi-Higgs production. The results have been published in [1, 2].

In chapter 6 we present first results for the production of a pair of electroweak vector bosons in association with a jet in hadron-hadron collisions at NLO precision, which is a background process to Higgs boson production in association with a jet and a further decay of the Higgs boson into a pair of vector bosons. It is considered as one of the most important processes for LHC phenomenology and is part of the experimental “NLO wishlist” of processes, shown in Table 1.1, for which QCD corrections are desired and feasible. A process at NLO is made of two parts: real emission of an additional unobserved parton and virtual corrections, which in our case involves the evaluation of one-loop integrals with up to five propagators in the loop (pentagon integrals). The high complexity of the latter is the bottleneck for obtaining NLO predictions. The first section explains the setup of the calculation of the one-loop matrix elements, using the techniques introduced in chapter 4. The impact of calculated virtual contributions is shown for several differential distributions which are often used in phenomenological studies.

Chapter 7 finally concludes this thesis with a brief summary. The calculation of a scalar box integral, needed for the process considered in chapter 6, and Feynman diagrams for $q\bar{q} \rightarrow ZZg$ are presented in the appendices.

process ($V \in \{Z, W, \gamma\}$)
1. $PP \rightarrow VV \text{ jet}$
2. $PP \rightarrow t\bar{t}b\bar{b}$
3. $PP \rightarrow t\bar{t} + 2 \text{ jets}$
4. $PP \rightarrow WWW$
5. $PP \rightarrow VVb\bar{b}$
6. $PP \rightarrow VV + 2 \text{ jets}$
7. $PP \rightarrow V + 3 \text{ jets}$
8. $PP \rightarrow b\bar{b}b\bar{b}$
9. $PP \rightarrow 4 \text{ jets}$
10. $gg \rightarrow W^*W^*$ (NLO, 2 loops)
11. NNLO for $t\bar{t}$
11. NNLO for $Z\gamma + \text{jet}$

Table 1.1: The Les Houches wishlist 2007 of processes for which a NLO calculation is both desired and feasible in the near future

Higgs Physics at the LHC

2

Although remarkable progress has been made in recent years to formulate possible explanations for unresolved fundamental problems like the weakness of gravity relative to other forces, the nature of dark matter and dark energy, the smallness of neutrino masses or a possible unification of all gauge forces, we still have not discovered the mechanism of electroweak symmetry breaking (EWSB). What exactly is the mechanism which gives mass to the weak gauge bosons and known fermions? This is one of the most important questions of particle physics today and it is possible that the understanding of this mechanism sheds light also on some of the open questions mentioned above.

In this chapter we will introduce the mechanism of spontaneous symmetry breaking known as the *Higgs mechanism* [3], which is a possible explanation of EWSB. This has become part of the Standard Model (SM) of particle physics, which is in excellent agreement with numerous experimental measurements. A doublet of complex scalar fields is introduced, and a single neutral scalar particle, the Higgs boson remains after symmetry breaking. We will describe how Higgs bosons can be produced and detected at the Large Hadron Collider (LHC) at CERN, where proton proton collisions will be studied at a center of mass energy $\sqrt{s} = 14$ TeV. The discovery of one or more Higgs bosons is indeed among the most important goals of this collider. Since the methods of detecting the Higgs boson depend crucially on the decay channels which are available for a given mass, these will be discussed in some detail. Furthermore, we discuss the theoretical and experimental constraints on the mass of the Higgs boson.

2.1 Higgs mechanism

The gauge invariance in Yang-Mills theories forbids to have explicit mass terms for the gauge vector bosons in the Lagrangian. This is acceptable for theories like Quantum Electrodynamics (QED) and Quantum Chromodynamics (QCD), where both the photon and the gluons are massless. However, the gauge bosons of the gauge theory of electroweak interactions, the charged W^\pm and the neutral Z boson, are massive ($M_W \approx 80$ GeV, $M_Z \approx 91$ GeV), and therefore in conflict with gauge invariance.

A possible solution to this problem is the Higgs mechanism. The Standard Electroweak Model is a spontaneously broken Yang-Mills theory based on the non-abelian $SU(2)_L \times U(1)_Y$ symmetry group. The Higgs mechanism is implemented by introducing a complex scalar field ϕ , which transforms as a doublet under $SU(2)$ which has hypercharge $Y_\phi = 1$,

$$\phi = \begin{pmatrix} \phi^+ \\ \phi^0 \end{pmatrix}. \quad (2.1)$$

The upper and lower components will later be identified as having electric charge (Q) one and zero respectively. For the moment, the superscripts only distinguish the two fields. The Lagrangian of the electroweak SM initially contains three massless bosons W^i , associated to the group $SU(2)$ and one massless boson B , associated to $U(1)$ and is written as

$$\mathcal{L}_V = -\frac{1}{4}W^{i,\mu\nu}W_{\mu\nu}^i - \frac{1}{4}B^{\mu\nu}B_{\mu\nu}, \quad (2.2)$$

where the field strength tensors are

$$W_{\mu\nu}^i = \partial_\mu W_\nu^i - \partial_\nu W_\mu^i - g_W \epsilon^{ijk} W_\mu^j W_\nu^k \quad (2.3)$$

$$B_{\mu\nu} = \partial_\mu B_\nu - \partial_\nu B_\mu, \quad (2.4)$$

g_W being the $SU(2)$ coupling. The scalar field ϕ is added via the Lagrangian

$$\mathcal{L}_\phi = (D^\mu \phi)^\dagger D_\mu \phi - V(\phi), \quad V(\phi) = \mu^2 \phi^\dagger \phi + \lambda (\phi^\dagger \phi)^2 \quad (2.5)$$

with $\lambda > 0$ for the scalar potential to be bounded from below and the covariant derivative, which minimally couples matter fields to the gauge fields,

$$D^\mu = \delta_{ij} \partial^\mu + ig_W (\tau_{ij}^a W^{a,\mu}) + ig'_W \frac{Y_\phi}{2} \delta_{ij} B^\mu, \quad (2.6)$$

and g'_W being the $U(1)$ coupling. The matrices τ^a , $a = 1, 2, 3$ are representations of the $SU(2)$ weak isospin algebra and satisfy the commutation relation $[\tau^a, \tau^b] = i\epsilon^{abc} \tau^c$, $\epsilon^{123} = 1$. The full Lagrangian

$$\mathcal{L} = \mathcal{L}_V + \mathcal{L}_\phi \quad (2.7)$$

is invariant under the $SU(2) \times U(1)$ gauge transformation of the form:

$$\phi_i(x) \rightarrow (1 + i\alpha^a(x)\tau^a)_{ij} \phi_j(x) + i\beta \phi_i(x), \quad (2.8)$$

$$W_\mu^a(x) \rightarrow W_\mu^a(x) + \frac{1}{g_W} \partial_\mu \alpha^a(x) + \epsilon^{abc} W_\mu^b(x) \alpha^c(x), \quad (2.9)$$

$$B^\mu(x) \rightarrow B^\mu(x) + \frac{1}{g'_W} \partial_\mu \beta(x). \quad (2.10)$$

If we now add explicit mass terms, $\frac{1}{2}M_V^2 W^\mu W_\mu$, for the gauge bosons in the above Lagrangian, this will violate local $SU(2) \times U(1)$ gauge invariance. This can be seen by taking the example of QED where the photon is massless due to the local $U(1)_Q$ local symmetry,

$$\frac{1}{2}M_A^2 A_\mu A^\mu \rightarrow \frac{1}{2}M_A^2 (A_\mu + \frac{1}{e}\partial_\mu \alpha)(A^\mu + \frac{1}{e}\partial^\mu \alpha) \neq \frac{1}{2}M_A^2 A_\mu A^\mu. \quad (2.11)$$

The incorporation of mass terms by brute force for gauge bosons therefore leads to a manifest breakdown of the local $SU(2) \times U(1)_Y$ gauge invariance of the SM¹.

The conclusion is, that we have to give up the idea of exact or unbroken gauge symmetry. But as has been shown in [3], there is an elegant way how to generate gauge boson and fermion masses without completely breaking local gauge invariance. Consider the potential term in (2.5): if the mass term μ^2 is positive, the potential $V(\phi)$ is also positive and the minimum of the potential is obtained for $\langle 0|\phi|0\rangle \equiv \phi_0 = 0$. Eq. (2.5) is simply the description of a Lagrangian of spin-zero particles with mass μ .

If $\mu^2 < 0$, the potential $V(\phi)$ has a minimum when $\partial V/\partial \phi = \mu^2 \phi + \lambda \phi^3 = 0$, i.e. when

$$\langle 0|\phi^2|0\rangle \equiv -\frac{\mu^2}{2\lambda} \equiv \frac{v^2}{2} \quad (2.12)$$

and not at $\phi_0^2 = 0$, as shown in Fig. 2.1. The quantity $v \sim \langle 0|\phi|0\rangle$ is called the vacuum expectation value (vev) of the scalar field ϕ . Transitions between the field configurations on the circle of degenerate minima cost no energy and correspond to massless excitations. The particle interpretation of a Lagrangian with a negative mass

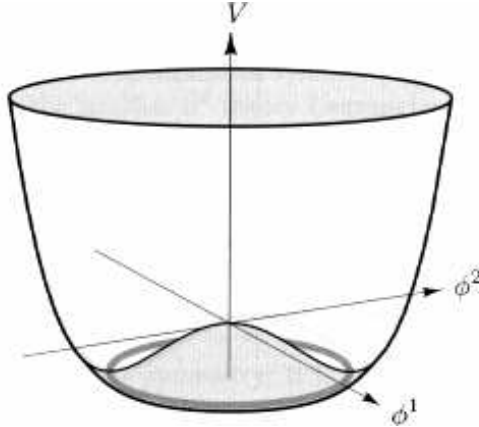


Figure 2.1: Scalar potential $V(\phi)$ which gives rise to spontaneous symmetry breaking in the Standard Model [4].

¹this is also true for fermions in the SM, since only the left-handed fermion fields are grouped in weak isospin doublets and their mass term contain a product of left- and righthanded fermion fields.

term is no longer clear. In order to correctly interpret the Lagrangian, we have to expand around one of the minima v . Since we want to preserve $U(1)_Q$, we choose the neutral component of the doublet field ϕ to develop a vev. We make the particular choice in the internal $SU(2)$ space for the minimum of ϕ ,

$$\langle 0|\phi|0\rangle = \frac{1}{\sqrt{2}} \begin{pmatrix} 0 \\ v \end{pmatrix}. \quad (2.13)$$

This choice leaves the vev invariant under transformations generated by $\tau^3 + \frac{1}{2}Y$, i.e.

$$\left(\tau^3 + \frac{1}{2}Y \right) \langle 0|\phi|0\rangle = 0. \quad (2.14)$$

This combination is the single unbroken generator which is identified with the electric charge,

$$Q = \tau^3 + \frac{1}{2}Y = \begin{pmatrix} 1 & 0 \\ 0 & 0 \end{pmatrix}. \quad (2.15)$$

The choice of a specific ground state in (2.13) breaks the $SU(2) \times U(1)$ symmetry, since it identifies a particular direction in the internal group space. As we will see below, this transforms the Lagrangian in such a way that the original gauge symmetry is now hidden or spontaneously broken. We need to consider the fluctuations around this new minimum, so we introduce a reparametrisation of the Higgs field in terms of the four fields $\theta_{1,2,3}(x)$ and $H(x)$ at first order,

$$\phi(x) = \begin{pmatrix} \theta_2 + i\theta_1 \\ \frac{1}{\sqrt{2}}(v + H) - i\theta_3 \end{pmatrix} = e^{i\theta_a \tau^a(x)/v} \begin{pmatrix} 0 \\ \frac{1}{\sqrt{2}}(v + H(x)) \end{pmatrix}. \quad (2.16)$$

Note that we still have four real degrees of freedom, equivalent to the two complex fields. We now make a specific local gauge transformation with $\alpha(x) = -\theta(x)/v$ in (2.8), and the scalar field transforms as

$$\phi(x) \rightarrow e^{-i\theta_a \tau^a(x)/v} \phi(x) = \frac{1}{\sqrt{2}} \begin{pmatrix} 0 \\ v + H(x) \end{pmatrix}. \quad (2.17)$$

The θ degrees of freedom no longer appear in the Higgs Lagrangian (2.5)². As we will see below, these modes reappear as the longitudinal modes of the massive gauge bosons. This gauge, where the unphysical degrees of freedom are “gauged away”, is called *unitary* gauge, since in it, the unitarity of the S -matrix is evident. The Higgs

²In a *global* (continuous) gauge theory, this choice is not possible and these degrees of freedom do not disappear. This is the famous Goldstone theorem [5] which states that for every spontaneously broken continuous symmetry, massless scalar spin-0 particles emerge, the so-called Goldstone bosons. The number of Goldstone bosons is equal to the number of broken generators.

boson H is the only dynamical remaining field. The Higgs Lagrangian now becomes

$$\mathcal{L} = \frac{1}{2} \partial_\mu H \partial^\mu H - V \left(\frac{(v + H)^2}{2} \right) + \frac{(v + H)^2}{8} (0 \ 1) (2 g_W \tau \cdot W_\mu + g'_W B_\mu) (2 g_W \tau \cdot W^\mu + g'_W B^\mu) \begin{pmatrix} 0 \\ 1 \end{pmatrix}. \quad (2.18)$$

We therefore have three generators of the $SU(2) \times U(1)$ symmetry, which are spontaneously broken. Only the symmetry generated by the combination $\tau^3 + \frac{1}{2}Y$ remains unbroken. According to Goldstone's theorem, we would expect three massless scalar bosons. However, these Goldstone modes are unphysical degrees of freedom which decouple from the physical S -matrix.³ They provide the extra longitudinal degree of freedom necessary to change the quanta of the vector fields from massless to massive vector bosons. The transmutation of Goldstone modes into longitudinal polarisation states of massive vector bosons is known as the *Higgs mechanism*.

To see how this works in practice, we examine the quadratic terms in the vector boson fields. Defining

$$W_\mu^\pm = \frac{1}{\sqrt{2}} (W_\mu^1 \mp i W_\mu^2), \quad T^\pm = T^1 \pm iT^2, \quad (2.19)$$

we have $W_\mu \cdot \tau = W_\mu^3 T_3 + \frac{1}{\sqrt{2}} (W_\mu^+ T^+ + W_\mu^- T^-)$. The usual commutation relations for the weak isospin raising and lowering operators T^+ and T^- read

$$[T^+, T^-] = 2T^3, \quad [T^3, T^\pm] = \pm T^\pm. \quad (2.20)$$

The quadratic terms in the vector boson fields are therefore given by

$$\mathcal{L}_M = \frac{v^2}{8} [(g_W W_\mu^3 - g'_W B_\mu)(g_W W^{3\mu} - g'_W B^\mu) + 2g_W^2 W_\mu^- W^{+\mu}]. \quad (2.21)$$

To diagonalise the propagator for the B and the W^3 field, we further define electrically neutral fields A and Z which propagate independently,

$$\begin{pmatrix} W_\mu^3 \\ B_\mu \end{pmatrix} = \begin{pmatrix} \cos \theta_w & \sin \theta_w \\ -\sin \theta_w & \cos \theta_w \end{pmatrix} \begin{pmatrix} Z_\mu \\ A_\mu \end{pmatrix}, \quad (2.22)$$

where the electroweak mixing angle θ_w is given by the relative strengths of the cou-

³According to the so-called quartet mechanism [6] unphysical states appear always as quartets and only zero norm states can appear in the physical space. The Goldstone mode in a local gauge theory, the so-called would-be Goldstone boson, is one member of this quartet. The other three modes, the ghost, the antighost and the B -mode arise during the quantisation procedure of Yang-Mills theories. For an elegant canonical treatment, we refer to [7].

pling constants,

$$\sin^2 \theta_W = \frac{g_W'^2}{g_W^2 + g_W'^2}. \quad (2.23)$$

After this rotation, (2.21) becomes

$$\mathcal{L}_M = \frac{g_W^2 v^2}{4} W_\mu^+ W^{-\mu} + \frac{(g_W^2 + g_W'^2) v^2}{8} Z_\mu Z^\mu + 0 \cdot A_\mu A^\mu. \quad (2.24)$$

The W and the Z bosons have acquired masses, while the photon remains massless,

$$M_W = \frac{1}{2} g_W v, \quad M_Z = \frac{1}{2} (g_W^2 + g_W'^2) v, \quad M_A = 0. \quad (2.25)$$

We summarise the important points of the concept of spontaneous symmetry breaking. The Lagrangian (2.7) is gauge invariant. Only the necessity of choosing one of the physically equivalent ground states as basis for the perturbation theory hides the gauge invariance. Spontaneous symmetry breaking introduces mass terms for gauge bosons, the necessary extra degree of freedom is obtained by “eating” the degree of freedom of the unphysical Goldstone boson. In the SM, only one neutral scalar particle remains as a physical particle, the Higgs boson, and the electroweak gauge bosons W^+ , W^- , and the electrically neutral Z -boson become massive.

The mass and the self-couplings of the Higgs boson are derived by inserting (2.17) in (2.5),

$$\mathcal{L}_\phi = \frac{1}{2} \partial_\mu H \partial^\mu H - \mu^2 H^2 - \lambda v H^3 - \frac{1}{4} \lambda H^4. \quad (2.26)$$

Its mass M_H and self-couplings are given by

$$M_H = \sqrt{2\lambda} v, \quad g_{HHH} = 3i \frac{M_H^2}{v}, \quad g_{HHHH} = 3i \frac{M_H^2}{v^2}. \quad (2.27)$$

One combination of the parameters in the Higgs potential in (2.5), $\mu^2/\lambda = v^2$ is related to the measured parameter G_F , the Fermi constant and therefore fixed. The other parameter, related to the Higgs mass, is essentially arbitrary. The existence of the Higgs boson has to be proven in collider experiments and its properties have to be measured in order to confirm the mechanism of spontaneous symmetry breaking.

2.2 Higgs mass constraints

Higgs boson phenomenology is the study of how the particle can be detected experimentally in various ways. One of the main difficulties is the arbitrariness of the Higgs mass, which leads to many different production and decay scenarios. However, there are experimental and theoretical constraints on the Higgs mass.

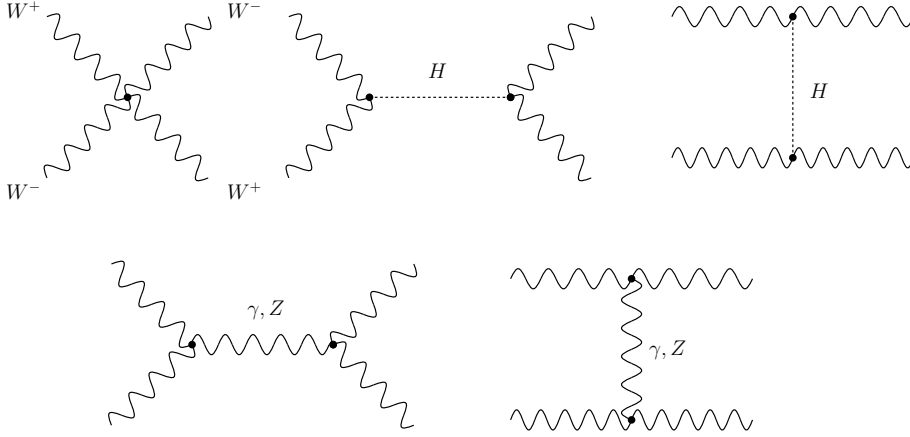


Figure 2.2: Feynman diagrams for $W^+ + W^- \rightarrow W^+ + W^-$

2.2.1 Perturbative Unitarity

The underlying gauge theory structure of the SM leads to strong cancellations in the high-energy behaviour of amplitudes for the scattering of gauge bosons. Here we consider the scattering of W -bosons. The contributing Feynman diagrams are shown in Fig. 2.2. The vector bosons can have longitudinal or transverse polarisations. In the high energy limit (i.e. for energies $s \gg M_W^2$) the scattering amplitude is dominated by the scattering of the longitudinal bosons. It can be easily calculated by using the electroweak equivalence theorem [4], which states that the scattering amplitudes for longitudinal gauge bosons V_L^i are expressible in terms of scattering amplitudes for the corresponding would-be Goldstone bosons ω^i . For instance, the scattering amplitude for $W_L^+ W_L^- \rightarrow W_L^+ W_L^-$ satisfies

$$\mathcal{M}(W_L^+ W_L^- \rightarrow W_L^+ W_L^-) = \mathcal{M}(\omega^+ \omega^- \rightarrow \omega^+ \omega^-) + \mathcal{O}\left(\frac{M_W^2}{s}\right) \quad (2.28)$$

where

$$\mathcal{M}(\omega^+ \omega^- \rightarrow \omega^+ \omega^-) = -\frac{M_H^2}{v^2} \left(\frac{s}{s - M_H^2} + \frac{t}{t - M_H^2} \right). \quad (2.29)$$

Although the leading-order WW scattering amplitude does not diverge at high energy, it still could be too large to be consistent with the bound imposed by the unitarity of the scattering matrix. To see this explicitly, we perform a partial wave expansion,

$$\mathcal{M} = 16\pi \sum_{l=0}^{\infty} (2l+1) P_l(\cos\theta) a_l, \quad (2.30)$$

where the P_l are the Legendre polynomials for a given orbital angular momentum l , and θ being the scattering angle. The differential cross section, neglecting particle masses, is given by $d\sigma/d\Omega = |\mathcal{M}|^2/(64\pi^2 s)$. Inserting (2.30) and using the orthogonality property of the Legendre polynomials, $\int_{-1}^1 dx P_l(x) P_{l'}(x) = \delta_{ll'}/\frac{2}{2l+1}$, we find for the total cross section

$$\sigma = \frac{16\pi}{s} \sum_{l=0}^{\infty} (2l+1) |a_l|^2. \quad (2.31)$$

The optical theorem relates the total cross section with the imaginary part of the scattering amplitude in the forward direction,

$$\sigma = \frac{1}{s} \Im[\mathcal{M}(\theta = 0)]. \quad (2.32)$$

This leads to the unitarity condition for the partial waves

$$|a_l|^2 = \Im[a_l] \longrightarrow |\Re[a_l]| \leq \frac{1}{2}. \quad (2.33)$$

This relation provides constraints on M_H . From (2.29), we find that the result for the $l = 0$ partial wave amplitude is

$$a_0 = -\frac{M_H^2}{16\pi v^2} \left[2 + \frac{M_H^2}{s - M_H^2} - \frac{M_H^2}{s} \log \left(1 + \frac{s}{M_H^2} \right) \right] \xrightarrow{s \gg M_H^2} -\frac{M_H^2}{8\pi v^2}. \quad (2.34)$$

From the requirement of the unitarity condition (2.33) and the numerical value for the vacuum expectation value, $v = 246$ GeV, we obtain the upper bound

$$M_H \lesssim 870 \text{ GeV} \quad (2.35)$$

This analysis can be done also for different scattering channels [8], and the upper bound can be lowered to

$$M_H \lesssim 710 \text{ GeV}. \quad (2.36)$$

We therefore find that if the Higgs boson mass is larger than $\mathcal{O}(1 \text{ TeV})$, the weak interactions should become strong. The tree-level analysis no longer adequately describes the high-energy scattering. Radiative corrections can be very large and indicate the breakdown of perturbation theory⁴. In order to use the unitarity argument as a bound on the Higgs mass, one has to assume that the SM remains perturbative and radiative corrections are not large. It is therefore a perturbative unitarity argument. By investigating the scattering of longitudinal vector bosons at a high-energy collider

⁴ A more sophisticated analysis including one- and two-loop corrections [9] and a comparison with non-perturbative calculations on the lattice [10] also shows that perturbation theory is lost for Higgs boson masses above $M_H \gtrsim 700$ GeV which is very close to the bound derived from the tree-level analysis.

which can probe the TeV-scale, we will either discover the Higgs boson or see strong interactions of electroweak bosons.

2.2.2 Triviality and vacuum stability

Another limit on M_H comes from the variation of the energy scale Q of the quartic Higgs boson self-coupling λ , which appears in the Higgs potential (2.5). This variation is governed by the Renormalisation Group Equation (RGE), and an explicit one-loop calculation, including fermion and gauge boson contributions, gives

$$\frac{d\lambda}{d \log Q^2} = \frac{1}{16\pi^2} \left[12\lambda^2 + 6\lambda\lambda_t - 3\lambda_t^4 - \frac{3}{2}\lambda(3g_W^2 + g_W'^2) + \frac{3}{16} \left(2g_W^4 + (g_W^2 + g_W'^2)^2 \right) \right], \quad (2.37)$$

where the top quark Yukawa coupling is given by $\lambda_t = \sqrt{2}m_t/v$. For large M_H , the first term in (2.37) dominates, since $M_H^2 = 2\lambda v^2$. The solution of the evolution equation for λ , choosing the electroweak symmetry breaking scale $Q_0 = v$ as a natural reference energy point, can be easily solved and reads

$$\lambda(Q^2) = \frac{\lambda(v^2)}{1 - \frac{3}{4\pi^2}\lambda(v^2) \log \frac{Q^2}{v^2}}. \quad (2.38)$$

The quartic coupling varies logarithmically with the squared energy Q^2 . For energies much greater than the weak scale, $Q^2 \gg v^2$, the coupling grows, and eventually reaches a singularity, the Landau pole. If one wants to avoid this singularity before some new physics scale $Q_0 = \Lambda$ (for example, the Planck scale or the grand unification scale), then the coupling at low energy ($\lambda(v)$) cannot be too large, which translates into an *upper* bound on the Higgs mass,

$$M_H^2 < \frac{8\pi v^2}{2 \log \frac{\Lambda^2}{v^2}}. \quad (2.39)$$

For small values of the quartic coupling, corresponding to a light Higgs boson, the top quark contribution can change the sign of (2.38) and its solution in this limit is

$$\lambda(Q^2) = \lambda(v^2) + \frac{1}{16\pi^2} \left[-3\lambda_t^4 + \frac{3}{16} \left(2g_W^4 + (g_W^2 + g_W'^2)^2 \right) \right]. \quad (2.40)$$

If the top Yukawa coupling λ_t is sufficiently large, the quartic Higgs coupling λ gets negative. If this happens, the potential in (2.5) is no longer bounded from below and has no minimum. The Higgs vacuum becomes unstable. This can be avoided by setting a *lower* limit on the Higgs mass, depending on the numerical value of the top quark mass m_t .

More accurate analyses include higher order corrections and details can be found in [11]. Fig. 2.3 shows the limits on M_H from the triviality and vacuum stability constraints as a function of the new physics scale Λ . The width of the bands corresponds to theoretical and experimental uncertainties. As can be read off, if the new physics

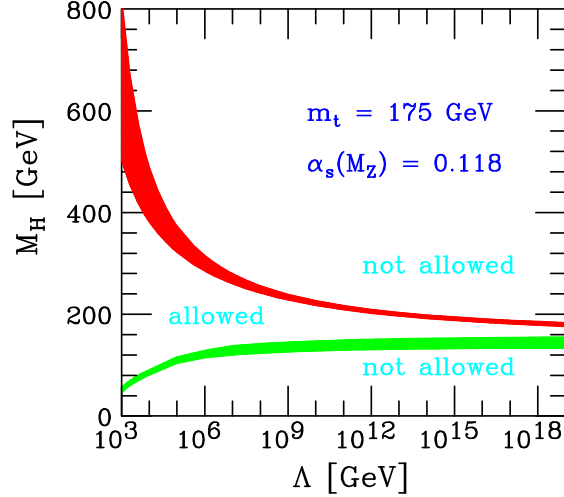


Figure 2.3: The triviality (upper) bound and the vacuum stability (lower) bound on the SM Higgs boson mass M_H as a function of the new physics scale Λ . The allowed region lies between the bands [11].

scale Λ is at the TeV scale, the Higgs boson mass is allowed to be in the range

$$50 \text{ GeV} \lesssim M_H \lesssim 800 \text{ GeV}. \quad (2.41)$$

Requiring the SM to be valid up to the Grand Unification scale, $\Lambda_{\text{GUT}} \approx 10^{16}$ GeV, the Higgs boson mass should lie in the range

$$130 \text{ GeV} \lesssim M_H \lesssim 180 \text{ GeV}. \quad (2.42)$$

2.2.3 Experimental constraints

The Higgs boson has been searched for at the e^+e^- collider LEP with a center-of-mass energy up to $\sqrt{s} = 209$ GeV. In this energy regime, the dominant production process is Higgs-strahlung, where the e^+e^- pair goes into an off-shell Z boson which splits into a real Z boson, which decays further, and a Higgs boson, see Fig. 2.4. Also other channels have been investigated by the LEP collaboration, and no significant excess above the expected SM background has been seen. The exclusion limit [12]

$$M_H > 114.4 \text{ GeV} \quad (2.43)$$

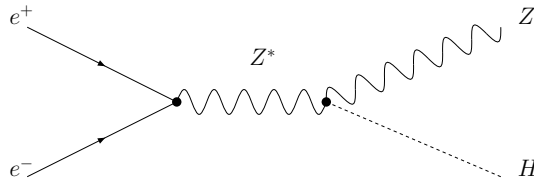


Figure 2.4: The production mechanism for SM Higgs bosons in e^+e^- collisions

has been established at the 95% confidence level [12]. This value is obtained by performing a likelihood ratio test of the hypothetical scenario, where one assumes that the data receives contributions from background processes and additional contributions from a SM Higgs boson of a given mass M_H .

The lower limit has been expected to be $M_H > 115.3$ GeV, where the data for the statistical test has been replaced by a large number of simulated event configurations. The reason for this discrepancy has been explained with an excess of 1.7 standard (σ)⁵ of events for a Higgs boson mass around $M_H = 116$ GeV. The production cross section at $M_H = 115$ GeV is of the order of 100 fb, which corresponds to ten produced events for a collected integrated luminosity of $\int \mathcal{L} \sim 0.1 \text{ fb}^{-1}$. At 117 GeV the production cross section drops to zero. This value is essentially the available collision energy minus the Z boson mass minus a few extra GeV to account for the finite width of the Z boson, which might be produced slightly off-shell with a non-zero rate. Therefore, a few signal events might have been observed, however this excess is not sufficient enough to claim the discovery of a Higgs boson. At least a 5σ signal is needed for this.

A second experimental constraint comes from indirect bounds from electroweak measurements. The Higgs particle contributes to the radiative corrections of high-precision electroweak observables, like the mass of the W boson, the electroweak mixing angle or various leptonic and hadronic asymmetries. Since the Higgs boson mass is the only free parameter of the Standard Model which is not yet determined experimentally, one can extract it indirectly from precision fits from all the measured electroweak observables, within the fit uncertainty. All available studies can be found on the LEP Electroweak Working Group webpage [13] and in their publications [14, 15]. The result is summarised in the famous “blue band plot”, Fig. 2.5. It shows the $\Delta\chi^2$ of the fit to all high-precision measurements as a function of the Higgs mass, with included theoretical uncertainties from missing higher order corrections, shown as a blue band. The preferred value for the SM Higgs boson mass, corresponding to the minimum of the curve, is

$$M_H = 76_{-24}^{+33} \text{ GeV} \quad (2.44)$$

⁵compare with a reported value of 2.9σ at the end of 2000

where the upper and lower limit is the experimental uncertainty at 68 % confidence level derived from $\Delta\chi^2 = 1$ for the solid line, thus not taking the theoretical uncertainty into account. This plot leads also to a 95% confidence level upper limit (corresponding to a $\Delta\chi^2 = 2.7$) of

$$M_H < 144 \text{ GeV.} \quad (2.45)$$

The top mass value for this fit is given by $m_t = 170.9 \pm 1.8 \text{ GeV}$. We note that already

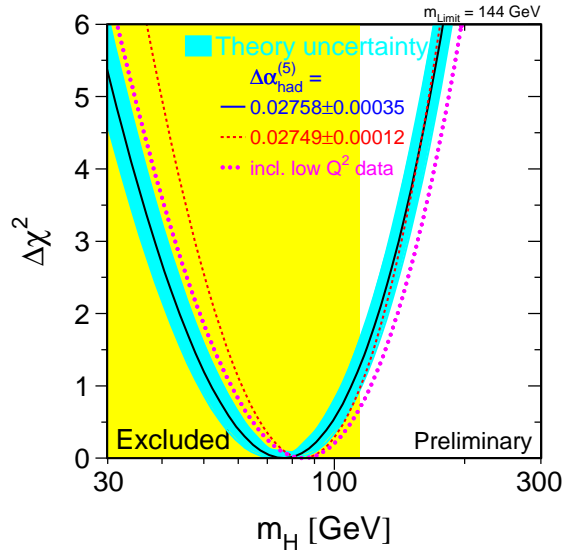


Figure 2.5: The $\Delta\chi^2 = \chi^2 - \chi_{\min}^2$ of the fit to the electroweak precision data as a function of M_H . The solid line results when all data are included, the blue band represents an estimate of the theoretical error due to missing higher order corrections. The effect of including low Q^2 data and the use of different values for $\Delta\alpha_{\text{had}}$ is also shown [13].

a large region of the $\Delta\chi^2$ band, in particular the region at the minimum is already excluded and values of M_H very close to the experimental lower bound seem to be favoured. However this fit is open to controversies, since it depends strongly on the fit input parameters. For instance, the minimum of $\Delta\chi^2$ shifts significantly, if a top quark mass of $178.5 \pm 3.9 \text{ GeV}$ is used, as was done in winter 2005 [16]. The best fit value for the Higgs mass was

$$M_H = 129_{-49}^{+74} \text{ GeV.} \quad (2.46)$$

It is therefore fair to say that no clear statement on the bounds of the Higgs mass, derived from electroweak precision fits, is possible.

2.3 Higgs Bosons at Hadron Colliders

The Tevatron at Fermilab near Chicago, USA, is a proton antiproton ($P\bar{P}$) collider where in Run II the operating energy was upgraded from 1.8 TeV to 1.96 TeV. The machine will stop operating at the end of this decade and a dataset, corresponding to $5 - 10 \text{ fb}^{-1}$ of integrated luminosity will be collected. The hope for finding a Higgs boson was high [17], but no clear evidence has been found so far.

The Large Hadron Collider (LHC), in the final construction phase at CERN in Geneva, Switzerland is a PP collider designed to run at an energy of 14 TeV in the pp center of mass. There are two general purpose experiments under construction, ATLAS and CMS. These detectors have been optimised to detect Higgs boson signatures and possible signatures of supersymmetry. For each experiment, it is hoped to collect at least 300 fb^{-1} of data. The larger dataset together with larger cross sections at the higher operating energy will allow the LHC to find the Higgs bosons and potentially new physics beyond the Standard Model.

2.3.1 Higgs boson production

Light quarks have a too small mass, and therefore Yukawa coupling to produce a Higgs boson with a usable rate. Quarks however may annihilate to the massive electroweak gauge bosons, which have a large coupling to the Higgs. Incoming quarks can also emit a pair of electroweak gauge bosons, which fuse to a Higgs boson. At high energy, the gluon content in hadrons is large, and gluons have a loop-induced coupling to Higgs bosons. Therefore, there are four relevant production mechanisms, all of them use the preference of the Higgs boson to couple to heavy particles:

- gluon fusion: $gg \rightarrow H$,
- vector boson fusion (VBF): $qq \rightarrow Hqq$ via W^+W^- , $ZZ \rightarrow H$,
- associated production with massive vector bosons: $q\bar{q} \rightarrow WH, ZH$,
- associated production with heavy top quarks: $gg, q\bar{q} \rightarrow t\bar{t}H$.

The Feynman diagrams for the four main production channels are displayed in Fig. 2.6. The lowest order cross sections for these processes are shown in Fig. 2.7 for the LHC collider as a function of the Higgs mass. The dominant mode is the gluon fusion process, followed by the vector boson fusion which amounts to about 20 % of the gluon fusion cross section in the low Higgs mass region. The propagator suppressed WH - and ZH production modes, as well as the $t\bar{t}H$ production mode are only relevant for the search of a light SM Higgs boson, with a mass close to the LEP exclusion limit.

For all the relevant production processes higher order QCD corrections have been calculated. Already more than ten years ago, the next-to-leading order (NLO) QCD corrections to gluon fusion have been calculated. They have been found to be large

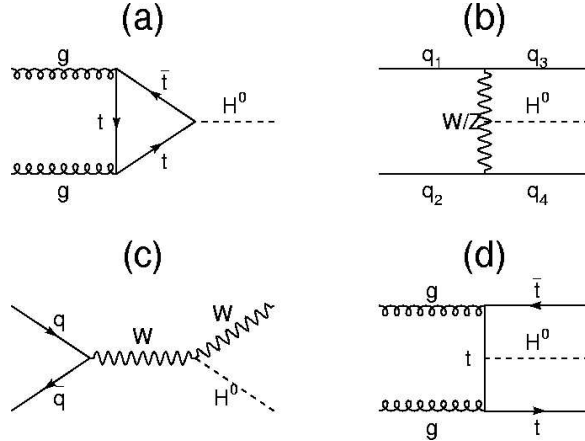


Figure 2.6: Feynman diagrams of the four dominant Higgs production channels

and increase the predicted LO cross section by about 50-100%. This motivated the calculation of next-to-next-to leading order (NNLO) corrections and has been completed in the heavy top-quark limit $m_t \rightarrow \infty$, which effectively reduces the one-loop amplitude in Fig. 2.6a to a tree-level amplitude. The correctness of this approximation can be tested at NLO by applying a rescaling factor which is obtained from the LO cross section with a finite top mass, divided by the cross section in the $m_t \rightarrow \infty$ limit. The agreement is within 5% with the full NLO calculation up to $m_H = 2m_t$. At high Higgs boson masses, $m_H = 1$ TeV, the deviation from the exact result is about 10%, which is surprisingly small. Therefore, it is reasonable to apply this approximation for the NNLO calculation, and the results are shown in Fig. 2.8. The increase for the total cross section between NLO and NNLO of 10-20% is modest, which indicates a good convergence of the perturbation series. Also the reduction of the uncertainty due to unknown higher order corrections is visible, which is based on the cross section dependence on the renormalisation scale μ_R and the factorisation scale μ_F . By varying the scales around a “natural scale” (which is expected to absorb large logarithmic corrections), one obtains an uncertainty band, and the narrower the band is, the smaller the higher order corrections are expected to be. Including higher orders should in principle reduce these uncertainty bands, and this is indeed observed for the gluon fusion process. The residual scale dependence at NNLO is 25% at the LHC.

Another example, where the inclusion of the NLO QCD correction significantly reduces the scale uncertainty is shown in Fig. 2.9. It shows the predicted LO and NLO production cross section for a Higgs boson in association with top quarks, as a function of the renormalisation and factorisation scale μ . For the choice $\mu = m_t + M_H/2$, for example, a modest increase of the order of 20% is found for the LHC.

However, one should be careful with the interpretation of the scale variation as an uncertainty estimate for unknown higher order corrections. The scale dependence is

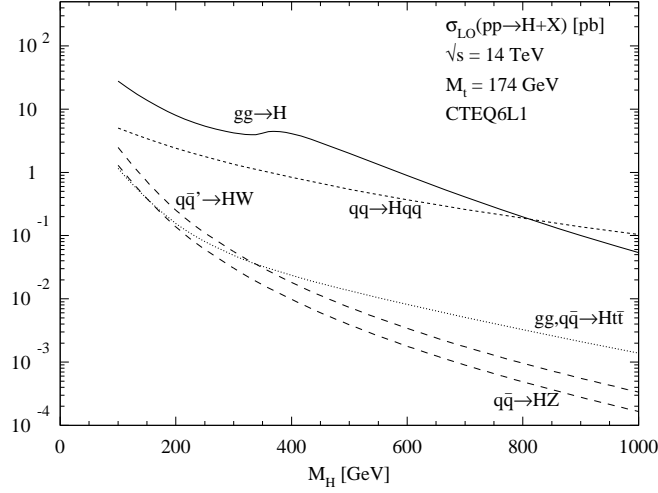


Figure 2.7: LO production cross sections for a SM Higgs boson as a function of the Higgs boson mass at the LHC [18].

unphysical, it is only a reflection of the truncation of the perturbation series. Cross sections to all orders do not depend on the scales. The scale variation is therefore no rigorous way to estimate the theoretical uncertainty. This can also be seen at the gluon fusion process, where the NLO and LO uncertainty bands do not overlap.

NLO calculations are also available for the two remaining production cross sections. For vector boson fusion, the NLO corrections are moderate, of the order of 10% [22, 23]. The NLO QCD corrections to Higgs production in association with a massive vector boson increase the LO cross sections by 30% [24].

The production cross sections for the four relevant channels including the NLO corrections are shown in Fig. 2.10.

2.3.2 Higgs boson decay

Once the SM Higgs boson mass is fixed, the decay profile is uniquely determined. The Higgs couplings to fermions (gauge bosons) are proportional to the mass (mass squared) of the particles, therefore the Higgs boson tends to decay into heaviest ones allowed by phase space. Since the masses of the gauge bosons, leptons and quarks are all known, all partial decay widths can be predicted.

The tree-level decay width for a Higgs boson decaying into fermion pairs is given by

$$\Gamma_{\text{Born}}(H \rightarrow f\bar{f}) = \frac{G_F N_c}{4\sqrt{2}\pi} M_H m_f^2 \beta_f^2, \quad (2.47)$$

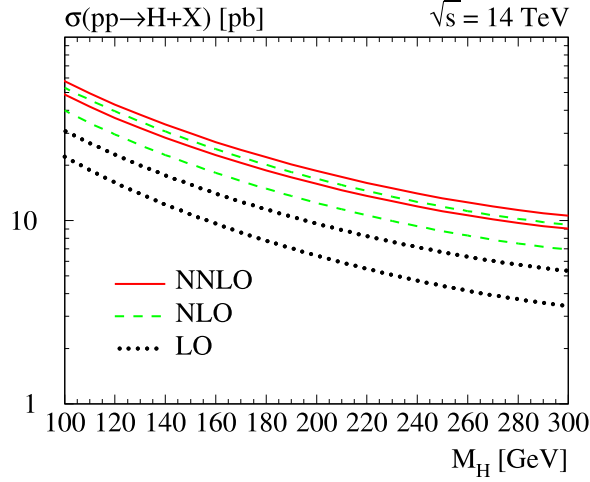


Figure 2.8: Gluon fusion production cross section for a SM Higgs boson at the LHC with higher order QCD corrections. The upper and lower curve is obtained by varying the renormalisation μ_R and factorisation scale μ_F ($\mu \equiv \mu_R = \mu_F$) within $m_H/2 < \mu < 2m_H$ [19].

where $\beta_f = \sqrt{1 - 4m_f^2/M_H^2}$ is the velocity of the fermions in the final state, $N_c = 3(1)$ is the colour factor for quarks (leptons), and G_F is the Fermi decay constant. Note that the decay width to fermions is linear in M_H , modulo the fermion velocity. The partial width for a Higgs boson decaying into two real massive gauge bosons, $H \rightarrow VV$, $V = W, Z$, is given by

$$\Gamma_{\text{Born}}(H \rightarrow VV) = \frac{G_F M_H^3}{16\sqrt{2}\pi} \delta_V \sqrt{1 - 4x} (1 - 4x + 12x^2), \quad x = \frac{M_V^2}{M_H^2}, \delta_W = 2, \delta_Z = 1. \quad (2.48)$$

The partial width is mainly cubic in the Higgs mass, and always dominates over the top quark decays. This cubic dependence originates from the scattering of longitudinally polarised vector bosons. Their wave functions in the high energy limit are linear in the energy which leads to an extra factor of M_H^2 in the decay widths.

Gluons and photons are massless particles, therefore they do not couple directly to the Higgs boson. Nevertheless, these couplings are generated at the one-loop level via a heavy fermion loop (for $H \rightarrow gg$) and an additional massive gauge boson loop (for $H \rightarrow \gamma\gamma, \gamma Z$). These loop decays are suppressed by additional electroweak or strong coupling constants and thus only important in the light Higgs mass regime below ~ 130 GeV, where the total Higgs width is still small. Fig. 2.11 shows all the decay branching ratios of the SM Higgs boson as functions of its mass M_H , including all important EW and QCD higher order corrections. The total width, the sum of all partial widths $\Gamma(H \rightarrow XX)$ is shown in Fig. 2.12. It is useful to consider three distinct mass ranges:

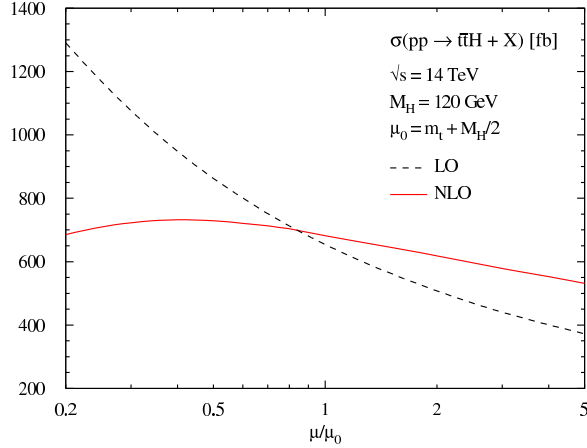


Figure 2.9: Variation of the $t\bar{t}H$ production cross section at the LHC with renormalisation and factorisation scale $\mu = \mu_R = \mu_F$ varied around the central scale $\mu_0 = m_t + m_H/2$ [20, 21].

1. the “low mass” range $110 \text{ GeV} \lesssim M_H \lesssim 130 \text{ GeV}$,
2. the “intermediate mass” range $130 \text{ GeV} \lesssim M_H \lesssim 180 \text{ GeV}$,
3. the “high mass” range $180 \text{ GeV} \lesssim M_H \lesssim 1 \text{ TeV}$.

In the “low mass” range, the Higgs boson decays mainly into a bottom quark pair ($b\bar{b}$), followed hierarchically by the decays into $\tau^+\tau^-$ and a charm quark pair ($c\bar{c}$). Significant is also the loop-induced decay $H \rightarrow gg$. Although the $\gamma\gamma$ decay is tiny, it is phenomenologically very important, since it provides a very clean signal, which can be seen over the very large hadronic backgrounds. The Higgs decays into VV^* , with one gauge boson being off-shell, is at the percent level for $M_H = 100 \text{ GeV}$ but increases dramatically with increasing M_H . The branching ratio for $H \rightarrow WW^*$ reaches $\sim 30\%$ at $M_H \sim 130 \text{ GeV}$, still 30 GeV below the W pair threshold. The decay into ZZ^* still occurs at the percent level for this mass value.

In the “intermediate mass” range, the decay into the heavy gauge bosons become dominant, with one virtual gauge boson below the $2M_V$ threshold. The only other relevant decay mode is the $b\bar{b}$ decay, which drops from $\sim 50\%$ at $M_H = 130 \text{ GeV}$ to the level of two percent at $M_H \sim 2M_W$. In the region $2M_W \lesssim M_H \lesssim 2M_Z$ both W bosons are real, while one Z boson is still virtual and therefore suppressed, leading to a WW branching ratio of almost 100%.

In the “high mass” range the Higgs boson decay almost exclusively into massive gauge bosons with a branching ratio of $\sim 2/3$ for WW and $\sim 1/3$ for ZZ final states. The $t\bar{t}$ channel opens at $M_H \gtrsim 350 \text{ GeV}$ and reaches a branching ratio of 20% slightly above the $2m_t$ threshold. It starts decreasing at $M_H \sim 500 \text{ GeV}$ and is below 10% at $M_H \sim 800 \text{ GeV}$.

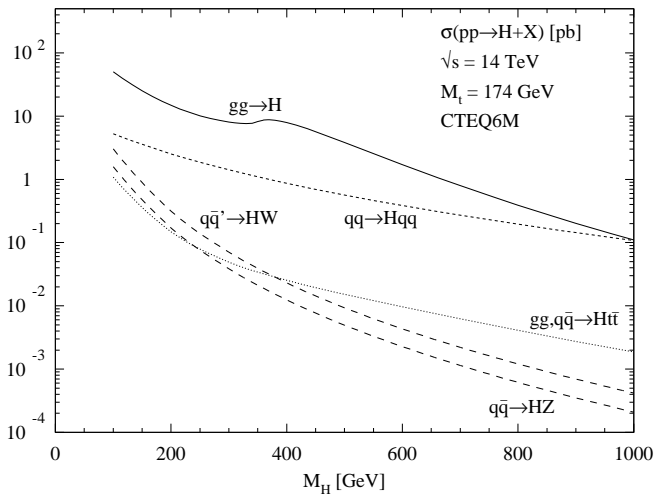


Figure 2.10: NLO production cross sections for a SM Higgs boson as a function of the Higgs boson mass at the LHC [18].

2.3.3 Search strategies and backgrounds

The SM Higgs boson will be searched for at the LHC in various decay channels. The discovery potential of a given channel depends on the signal rates and signal-to-background ratios. In the following, only the most important Higgs discovery channels are discussed, for a more detailed discussion, we refer to [18, 26] and the references therein.

The leading production mode for Higgs bosons is gluon fusion, $gg \rightarrow H$. Although the cross section for this process is very large, it has to compete against the enormous hadronic background, since the Higgs boson mainly decays into $b\bar{b}$ in the light and intermediate mass region. There is also no other non-hadronic particle involved, which could help to distinguish this mode from the overall hadronic activity, which makes this channel useless for the Higgs boson discovery. The main hope for discovering the Higgs boson lies in the investigation of decay channels with leptonic final states.

The rare decay mode $H \rightarrow \gamma\gamma$ can be used for the Higgs search if the Higgs boson mass is below 150 GeV, where both the production cross section and decay branching ratio are sufficiently large. A huge reducible QCD background originates from jets faking photons. The Higgs signal shows as a peak in the two-photon invariant mass distribution $d\sigma/dM_{\gamma\gamma}$. The background can be normalised very precisely from the sidebands of this distribution, where we know that there is no Higgs signal. Fig 2.13 shows the results of an ATLAS study.

Since the decay is rare, a large amount of data has to be collected. This mode is especially important for measuring the Higgs mass at low M_H . Since the decay into two photons is loop-induced, it is also very sensitive to new physics.

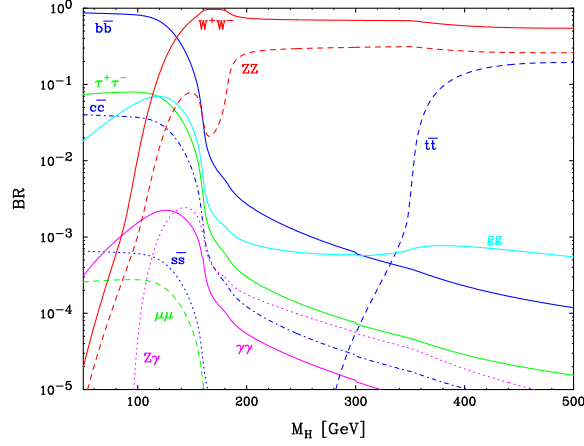


Figure 2.11: SM Higgs decay branching ratios as a function of M_H [25].

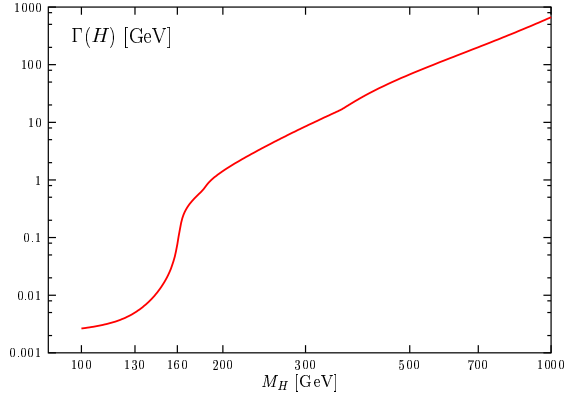


Figure 2.12: Decay widths of the SM Higgs boson [26].

The decay channel $H \rightarrow ZZ^{(*)} \rightarrow 4\ell$ is the “gold-plated” mode in the high mass region. It allows the detection of the Higgs boson up to $\mathcal{O}(1)$ TeV. The main background is the continuum production of Z pairs and is known theoretically rather precisely, but it can be also interpolated experimentally from the sidebands of the four-lepton invariant mass distribution. The discovery reach can be extended down to Higgs masses $M_H \approx 120$ GeV, when allowing one of the Z bosons to be virtual, except in the narrow mass range $M_H \approx 2M_W$ to $M_H \approx 2M_Z$ where the branching ratio is suppressed due to the opening of the WW decay mode. In this range, one can use the $H \rightarrow WW^{(*)} \rightarrow \ell\nu\ell\nu$ decay. The neutrinos cannot be detected, therefore it is not possible to reconstruct the Higgs boson mass peak. The Higgs signal is observed as an excess of events above the background, originating mainly from WW , $t\bar{t}$ and single top production processes. The signal significance depends strongly on their precise knowledge.

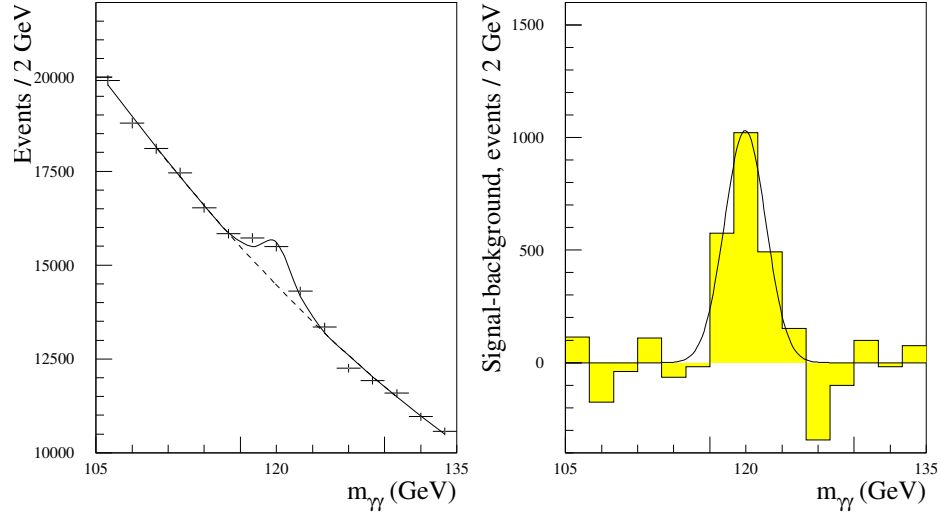


Figure 2.13: ATLAS simulation of $gg \rightarrow H \rightarrow \gamma\gamma$ at LHC for $M_H = 120$ GeV and 30 fb^{-1} of data [27]. The right plot shows the mass distribution after background subtraction, normalised from sidebands.

The discovery potential is significantly increased by studying the Higgs production in the VBF mode. Although the production cross section only amounts to about 20% of the total production cross section in the intermediate mass range, the additional event characteristics can be used to suppress the large backgrounds in all Higgs decay channels. The initial quarks that emit the vector bosons scatter with significant transverse momentum and will show up as forward and backward jets in the hadronic calorimeter. The Higgs boson, however, is produced centrally and so are its decay products, independently of the decay mode. A central jet activity of the initial quarks is suppressed due to the lack of colour exchange. This is in contrast to most background processes, where the colour flow appears in the t -channel. The differences are visualised in Fig. 2.14, where the pseudorapidity (η) distribution and the separation $\Delta\eta$ between the two tag jets is shown for signal events with $M_H = 160$ GeV and $t\bar{t}$ events. See chapter 3 for the definition of the kinematic variables occurring in the distributions. Therefore, the tagging of the forward and backward jet together with a veto of jet activity in the central region drastically reduce the large backgrounds and enhance the signal-to-background ratio. After applying suitable cuts, approximately 30% of the Higgs signal events in the Higgs mass range of 100 to 200 GeV are left over from the initial data sample, which is still large, at the order of a few picobarns. Since higher order QCD corrections and uncertainties from scale variations are rather small, VBF will play a key role when properties of the Higgs boson will be studied.

The discovery potential of the decay $q\bar{q}H \rightarrow q\bar{q}WW$ in VBF, for instance, is larger than in the inclusive $H \rightarrow WW^{(*)}$ channel, since the signal sensitivity is less affected by systematic uncertainties on the predictions of the (suppressed) background.

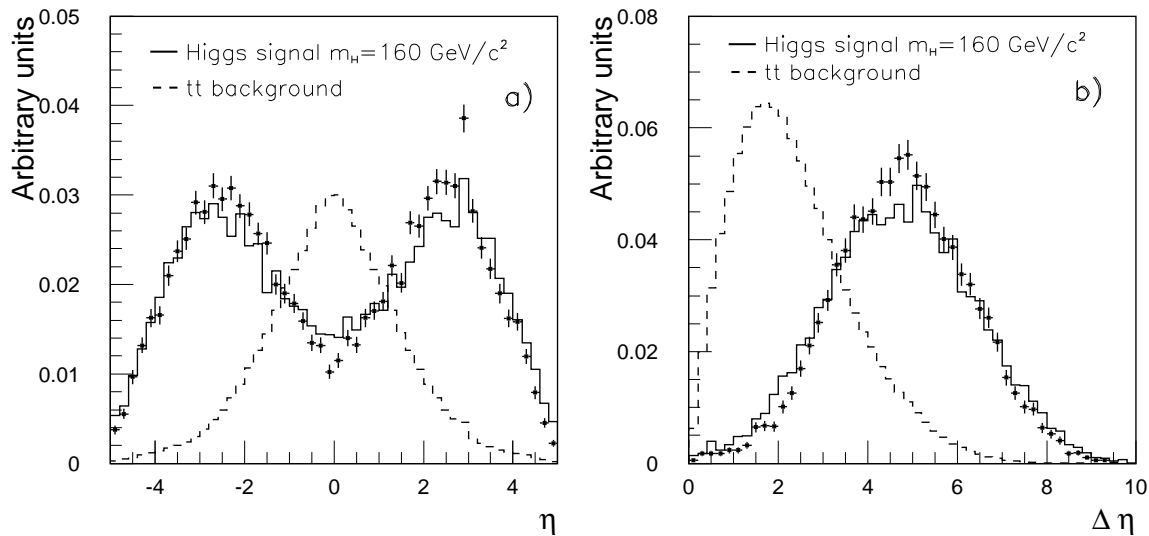


Figure 2.14: Tagging jet rapidity (left) and separation (right) for VBF Higgs production vs. $t\bar{t}$ background events [28].

Fig. 2.15 shows the large suppression of backgrounds for the transverse mass distribution in the VBF case in comparison to the gluon fusion mode.

Early studies of the Higgs production in association with top-quarks and a subsequent decay of the Higgs boson into a b-quark pair considered this channel very important for Higgs discovery in the low mass range [27]. These studies greatly underestimated the large QCD background from $t\bar{t} + 2\text{jet}$ production. The problem lies in the uncertainty on the exact shape of the QCD background, due to missing higher order corrections. The calculation of the QCD corrections to this $2 \rightarrow 4$ process is a very challenging task and considered very important, see Table 1.1 in chapter 1. More recent ATLAS studies show that the Higgs boson discovery with a significance of more than 5σ is no longer possible.

The combined signal significance over the full Higgs mass range, $100 \text{ GeV} < M_H < 1000 \text{ GeV}$, is shown in Fig. 2.16, assuming an integrated luminosity of 30 fb^{-1} . The signal significance is always larger than 5σ , and several discovery channels are available at the same time. Note that higher order QCD corrections have not been taken into account (no K-factors). However, this would allow for more precise predictions and stabilises the scale dependence. They can also change the kinematical properties of the processes under study. This is particularly true for the $gg \rightarrow H$ signal, where large QCD corrections occur. The chapters 3, 4 and 6 discuss the impact and need of higher order corrections in more detail.

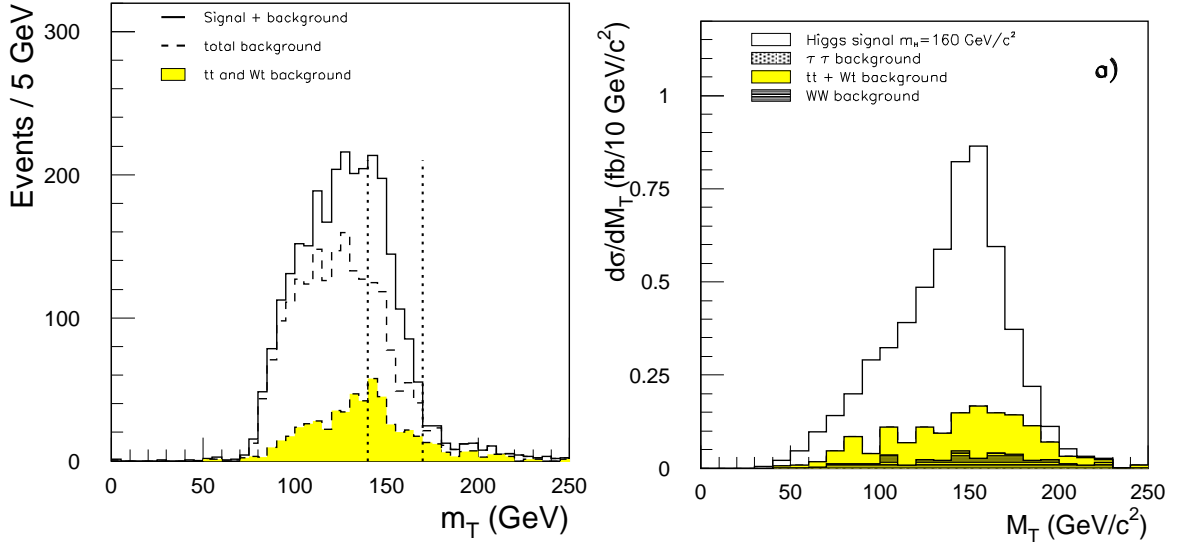


Figure 2.15: ATLAS simulations of $H \rightarrow WW$ events for $M_H = 170$ GeV (left, from [27]) and $q\bar{q}H \rightarrow q\bar{q}WW$ for $M_H = 160$ GeV (right, from [28]).

2.4 Summary

The Higgs boson is the key for one of the most important problems in particle physics: understanding the origin of particle masses. From direct searches at LEP we already found a lower bound for the SM Higgs boson, $M_H > 114.4$ GeV. The LHC will find it if its mass is less than $\mathcal{O}(1)$ TeV. If the Higgs boson doesn't exist, we can expect to discover new physics, which sheds light onto the mechanism of electroweak symmetry breaking.

Although the Higgs mechanism is an elegant solution of this problem, it is not without difficulties. There is a severe fine-tuning (“naturalness”) problem of the Higgs mass. Unlike the gauge bosons and fermions, the scalar SM Higgs boson is not protected by a symmetry of acquiring large contributions to the physical mass from radiative corrections, which would drive the Higgs mass up to some ‘new-physics’ or grand unification scale. One can of course write down a counterterm during the process of renormalisation, which exactly cancels these radiative corrections. The value of its coefficient however has to be severely fine-tuned if the new-physics scale is larger than $\mathcal{O}(1)$ TeV, which is regarded as unnatural.

One of the most popular extensions of the SM, which circumvent the naturalness problem is supersymmetry (SUSY). It extends the two fundamental groups of the SM, the Poincaré group and the $SU(3) \times SU(2)_L \times U(1)_Y$ gauge group of the strong and electroweak interactions, and induces an equal number of bosonic and fermionic states. The Higgs sector of the minimal supersymmetric standard model (MSSM), contains *two* complex Higgs doublets. The masses of the resulting five Higgs bosons

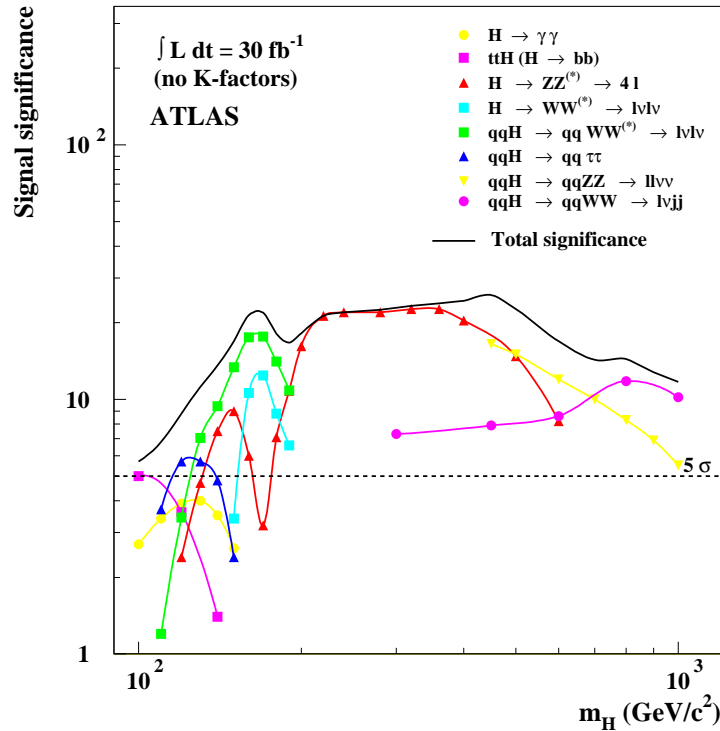


Figure 2.16: ATLAS sensitivity for the discovery of a SM Higgs boson for an integrated luminosity of 30fb^{-1} [28].

are expressible (at tree level) by just two parameters, the ratio of the two non-zero vevs, $\tan\beta = v_2/v_1$, and the mass of the CP-odd scalar boson, M_A . The key feature of the MSSM is the existence of an upper bound of the lightest SUSY Higgs boson at the order of 140 GeV. It has a similar behaviour as the SM Higgs boson and the calculations and search strategies described in this chapter again apply. There are many studies which show that the LHC will be sensitive to almost the entire $(M_A, \tan\beta)$ parameter space.

Hadron collider cross sections

3

The Standard Model contains quarks and gluons as fundamental particles. The leading interaction between these particles is the strong interaction, which is well described by Quantum Chromodynamics (QCD), a non-abelian gauge theory based on the group $SU(3)$. This theory has two important properties: asymptotic freedom and confinement¹. Asymptotic freedom tells us why the methods of perturbation theory are useful at high energy, or equivalently, at small distances. The strength of the strong interaction is governed by α_s , the strong coupling constant. Unlike QED, the coupling constant *decreases* with growing energy, which is a direct consequence of the non-abelian nature of QCD. The variation of the coupling constant with the energy scale Q is given by the Renormalisation Group and can be calculated with perturbative methods. The absolute value however has to be obtained from experiment, where Q is large enough to be in the perturbative domain. A one-loop calculation gives the relation between $\alpha_s(Q^2)$ and $\alpha_s(\mu^2)$ for two arbitrary scales in the perturbative regime,

$$\alpha_s(Q^2) = \frac{\alpha_s(\mu^2)}{1 + b\alpha_s(\mu^2) \log \frac{Q^2}{\mu^2}}, \quad b = \frac{33 - 2n_f}{12\pi}. \quad (3.1)$$

From measurements, one obtains $\alpha_s(M_Z^2) = 0.118$ as numerical value for the coupling constant. It is crucial that the sign of b is positive, since n_f , the number of active flavours is smaller than 17. Evidently as Q gets large, the running coupling $\alpha_s(Q^2)$ decreases to zero. This is the property of *asymptotic freedom*. From eq. (3.1) one can also deduce where the coupling becomes strong. Depending on the precise definition and including higher order corrections, a value of $Q = \Lambda_{\text{QCD}} \approx 200$ MeV is obtained. This point, where the denominator of (3.1) vanishes, is called the Landau pole. Thus, perturbation theory breaks down for scales comparable to the masses of light hadrons, i.e. $Q \approx 1$ GeV. The *confinement* of quarks and gluons inside the hadron, which cannot be observed as free particles, but only as constituents of hadrons, could therefore be a consequence of the decrease at high scales that leads to asymptotic freedom.

¹It turns out that among the renormalisable quantum field theories in four space-time dimensions, only the non-abelian gauge theories are asymptotically free [29].

At the LHC, the colliding particles are protons and it is necessary to relate the interactions at the parton level to the interactions of the hadron level to make theoretical predictions. The basis for doing this is the parton model, which is described in the next section.

3.1 Parton model

The parton model describes the interactions of hadrons in high-energy collisions. In this model, a scattering process of two hadrons results from pointlike constituents of the incoming hadrons, the so-called partons, which are identified as quarks and gluons. To derive a first approximation to the cross section for hadron-hadron scattering, we consider the reaction in the hadronic center-of-mass system where the hadrons move rapidly towards each other. We also assume that the center-of-mass energy is large enough to neglect the proton mass. Then the proton has an almost lightlike momentum P^μ along the collision axis. The constituents of the proton also have momenta p^μ which are almost collinear with the proton momentum. They can only acquire a large transverse momentum through the exchange of a hard gluon², which is suppressed by the smallness of α_s at large momentum scales, and can therefore be neglected at LO QCD perturbation theory. Thus, at LO, we can write

$$P^\mu = xp^\mu, \quad (3.2)$$

where x is a number between 0 and 1, called the longitudinal fraction of the parton. At LO, we also ignore gluon emission during the hard scattering process. The cross section for a hard scattering process initiated by two hadrons with momenta P_1^μ, P_2^μ is then given by the cross section $\hat{\sigma}$ for parton-parton scattering with given momentum fractions x_1, x_2 , multiplied by the probabilities $f_i(x)$ that the hadrons contain partons at these values of x_1, x_2 , integrated over x_1, x_2 :

$$\sigma(P_1, P_2) = \sum_{i,j} \int_0^1 dx_1 \int_0^1 dx_2 f_i(x_1) f_j(x_2) \hat{\sigma}_{ij}(p_1, p_2). \quad (3.3)$$

This is visualised in Fig. 3.1. After the hard scattering process, the struck partons interact softly with the remainder of the hadrons, so that the pieces materialise as jets of hadrons, approximately collinear to the direction of the original final state partons.

The functions $f_i(x)$ are called the parton distribution functions (pdf), and cannot be computed using QCD perturbation theory, since they depend on the soft processes

²The parton model can be also formulated in a field theoretical way, using the operator-product expansion together with the renormalisation group. This essentially confirms the more intuitive picture of the parton model. The more rigorous treatment leads to so-called ‘higher-twist’ contributions, which are power suppressed by the inverse of the hard scattering scale Q .

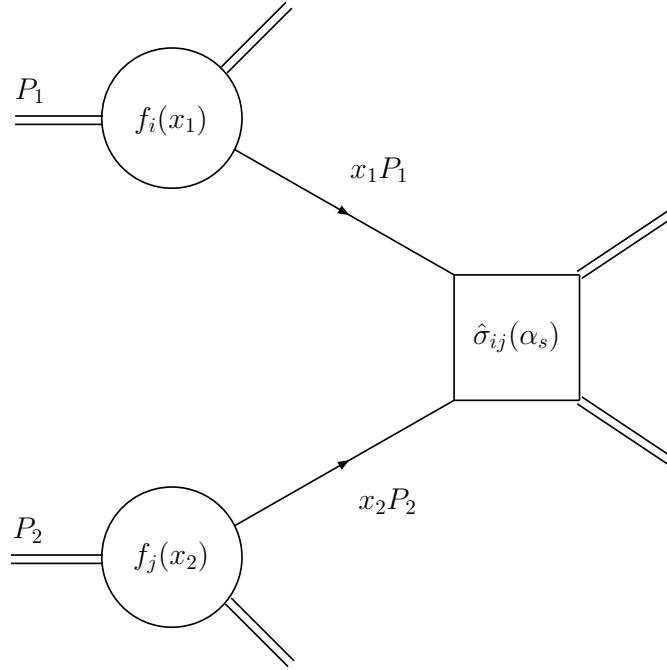


Figure 3.1: The parton model description of a hard scattering process

(where α_s is large) that determine the structure of the proton as a bound state of quarks and gluons. They have to be determined from experiment. The short-distance cross section for the scattering of partons of types i and j is denoted by $\hat{\sigma}_{ij}$. It is independent of interactions between partons of the same hadron, since the interaction time of the two incoming partons is very short in comparison to the soft interaction time in the hadron. Effectively, a static hadron is seen, and the short-distance cross section can be calculated as a perturbation series in the strong coupling constant α_s , since the coupling is small at high energy. Note that (3.3) is not the complete QCD prediction, but only the first term of an expansion in α_s . This approximation is called the *parton model* [30, 31] and is justified by the property of asymptotic freedom. This naive model predicts that the pdfs are independent of the momentum transfer Q of the interacting partons, which is known as Bjorken scaling. This is essentially the statement that the structure of the hadron looks the same to the incoming parton of the other hadron, no matter how hard the hadron is struck.

However, the strict Bjorken scaling is violated by logarithms of Q^2 , if higher order QCD corrections are taken into account. Even in an asymptotically free quantum field theory, the coupling constant is still nonzero for any finite momentum transfer. In fact, the decrease is very slow, logarithmic in momentum. Therefore, we will find small corrections to Bjorken scaling due to the exchange or emission of high transverse momentum gluons. The simplification of lightlike hadronic momenta is also only approximate, when corrections from gluon exchange and emission are considered. These

corrections contain mass singularities, i.e. singularities associated with collinear or soft emission in the limit of zero mass. They result not only from virtual particles in the loop integral. The real emissions of soft or collinear massless particles gives rise to similar singularities, when integrating over the phase space of the emitted particles. The Kinoshita-Lee-Nauenberg theorem [32, 33] states that all mass singularities from final states cancel in scattering amplitudes order by order in perturbation theory. In hadronic scattering processes, where quarks and gluons appear in the initial state of a partonic subprocess, collinear singularities remain. The pdfs are not directly measurable quantities, since the partons are not free particles, but confined in the hadron. On this level, we cannot expect a cancellation. The collinear singularity ($p_T \rightarrow 0$) corresponds to a long-range (“soft”) part of the strong interaction, which is not calculable in perturbation theory. It can be absorbed process-independently into the bare pdf at a factorisation scale μ_F , in analogy to the renormalisation procedure which deals with the ultraviolet divergences, see section 4.2. The ability to factorise the long- and short-distance contributions to the physical cross sections is a fundamental property of the theory and holds to all orders in perturbation theory [34]. The evolution of the pdfs as a function of the factorisation scale is obtained with perturbative methods and given by the Altarelli-Parisi equations [35].

Factorisation tells us how to deal with the collinear singularities, but there is an arbitrariness in how the finite contributions are treated. This has to be defined in a factorisation scheme. A widely used choice is the $\overline{\text{MS}}$ scheme where only the divergence (and a ubiquitous factor $\log(4\pi) - \gamma_E$) is absorbed into the pdfs. The factorisation scale μ_F is an arbitrary parameter, which can be thought of as the scale which separates the long- and short-distance physics. Simplifying, a parton with transverse momentum below μ_F is considered as a part of the hadron structure and is absorbed into the definition of the pdf. Partons emitted with a transverse momentum above μ_F are part of the hard scattering cross section $\hat{\sigma}$. The scale μ_F is usually chosen to be at the order of the hard scale Q , where parton-parton interaction takes place. Including more terms in the perturbative expansion will soften the dependence of the cross section on μ_F . The same is true for a variation of the renormalisation scale μ_R . The cross section to all orders is independent of the scales,

$$\frac{\partial \sigma}{\partial \mu_F} = \frac{\partial \sigma}{\partial \mu_R} = 0. \quad (3.4)$$

The simplifying assumption $\mu \equiv \mu_F = \mu_R$ is often made, with the standard choice $\mu = Q$.

In summary, a NLO QCD cross section with two initial-state hadrons with momenta

P_1 and P_2 and n partons in the final state is given by

$$\sigma(P_1, P_2) = \sum_{i,j} \int_0^1 dx_1 \int_0^1 dx_2 f_i(x_1, \mu_F^2) f_j(x_2, \mu_F^2) [\hat{\sigma}_{ij}^{\text{LO}}(p_1, p_2) + \hat{\sigma}_{ij}^{\text{NLO}}(p_1, p_2, \mu_F^2, \mu_R^2)], \quad (3.5)$$

with

$$\hat{\sigma}_{ij}^{\text{LO}}(p_1, p_2) = \int_n d\hat{\sigma}_{ij}^{\text{B}}(p_1, p_2), \quad (3.6)$$

$$\hat{\sigma}_{ij}^{\text{NLO}}(p_1, p_2, \mu_F^2, \mu_R^2) = \int_{n+1} d\hat{\sigma}_{ij}^{\text{R}}(p_1, p_2, \mu_R^2) + \int_n d\hat{\sigma}_{ij}^{\text{V}}(p_1, p_2, \mu_R^2) + \int_n d\hat{\sigma}_{ij}^{\text{C}}(p_1, p_2, \mu_F^2), \quad (3.7)$$

where the collinear counterterm $d\hat{\sigma}_{ij}^{\text{C}}$ for the pdfs can be found in [36], for instance. $d\hat{\sigma}_{ij}^{\text{B}}$, $d\hat{\sigma}_{ij}^{\text{R}}$ and $d\hat{\sigma}_{ij}^{\text{V}}$ denote the fully exclusive cross sections in the Born approximation and to one-loop order (R: real emission; V: virtual correction), respectively. They are integrated over the corresponding parton phase space, denoted by \int_{n+1} , \int_n . Only the sum of the three terms in (3.7) is free of singularities and can be integrated numerically.

Fig. 3.2 shows the quark and gluon distributions in the proton, resulting from a global NLO QCD fit to deep-inelastic scattering data [37]. The proton consists of three *valence* quarks (uud) which carry its electric charge and baryon quantum numbers, and an infinite *sea* of $q\bar{q}$ pairs and gluons. The total amount of the momentum of the proton is the sum of the parton momenta, which implies

$$\int_0^1 dx x \left[\sum_{i=u,d,s,c,b} f_i(x) + f_{\bar{i}}(x) + f_g(x) \right] = 1. \quad (3.8)$$

Note that a significant fraction of the energy-momentum is carried by the gluons.

3.2 Phase space integration

The differential cross section for the scattering of two partons with momenta p_1 and p_2 and masses m_1 and m_2 into n partons with momenta p_3, \dots, p_{n+2} is given by the squared invariant matrix element \mathcal{M} , multiplied with the flux of the incoming partons and the phase space density $d\Phi_n$ of the outgoing partons,

$$d\hat{\sigma} = \frac{1}{4\sqrt{(p_1 \cdot p_2)^2 - m_1^2 m_2^2}} \overline{\sum} \left| \mathcal{M}(p_1, p_2 \rightarrow \{p_f\}) \right|^2 \times d\Phi_n, \quad (3.9)$$

where $\overline{\sum}$ denotes the average and sum over the initial and final state spins and colours respectively. The total cross section is obtained by integrating over the phase space

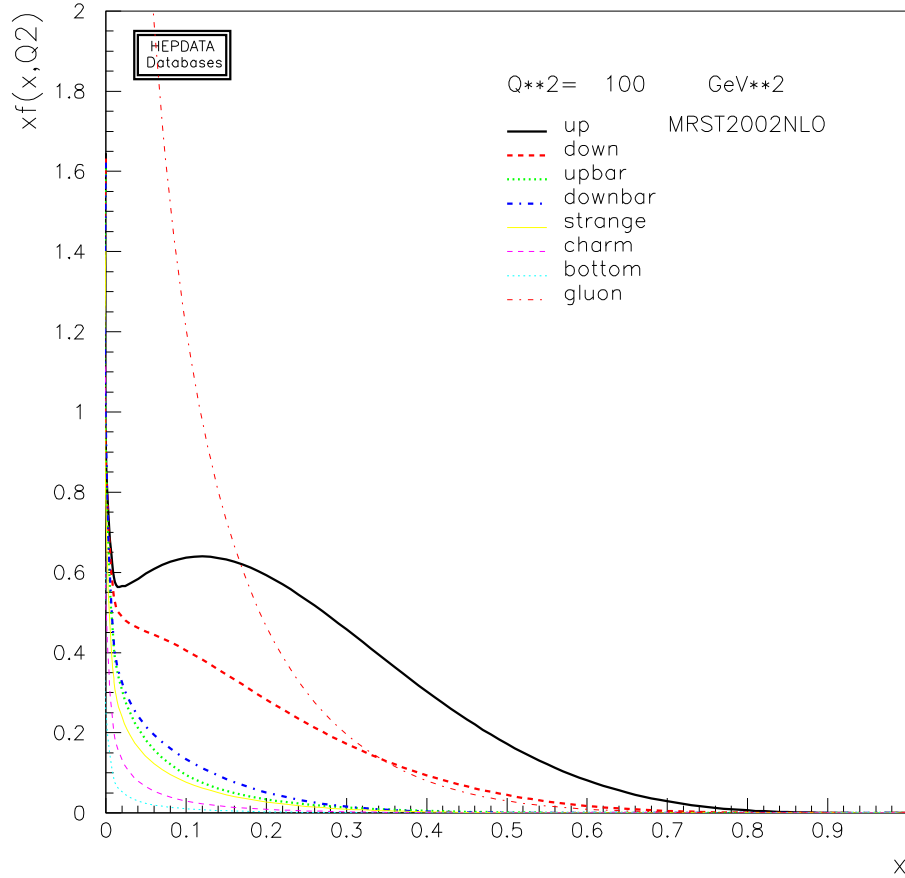


Figure 3.2: Quark and gluon distribution functions $x f_i(x, Q^2)$ of the proton, at $Q^2 = 100 \text{ GeV}^2$ [38].

of the final state. For any set of n identical particles in the final state, a symmetry factor $1/n!$ has to be included in this inclusive quantity.

The parametrisation of the phase space for $2 \rightarrow 2$ and $2 \rightarrow 3$ processes, as it was used for the calculations in this thesis, is shown now. The two incoming (massless) particles define the beam axis and carry a center-of-mass energy of $\sqrt{\hat{s}}/2$. For each final state particle an integral over its three-momentum \vec{p} occurs in the calculation of integrated cross sections. The energy p^0 of the particle is fixed by the on-shell condition $p^0 = \sqrt{|\vec{p}|^2 + m^2}$, where m denotes the mass of the particle. Four of the momentum integrals can be eliminated by energy-momentum conservation. The Lorentz-invariant phase space element for an n -particle final state is given by

$$d\Phi_n = (2\pi)^4 \delta^{(4)} \left(p_1 + p_2 - \sum_{f=3}^{n+2} p_f \right) \prod_{f=3}^{n+2} \frac{d^3 p_f}{(2\pi)^3} \frac{1}{2E_f}. \quad (3.10)$$

3.2.1 Two-particle phase space

For a two-particle final state with the momenta p_3, p_4 respectively, the integral can be written in terms of the azimuth angle ϕ and the polar angle θ with respect to the beam axis. Due to the rotational invariance around the beam axis, the integration over ϕ can be trivially performed and contributes a factor 2π . The phase space element is given by

$$d\Phi_2 = \frac{1}{(2\pi)^2} \delta^{(4)}(p_1 + p_2 - p_3 - p_4) \frac{d^3p_3}{(2\pi)^3} \frac{1}{2E_3} \frac{d^3p_4}{(2\pi)^3} \frac{1}{2E_4} \quad (3.11)$$

$$= \frac{1}{(4\pi)^2} \frac{|\vec{p}_3^{cm}|}{\sqrt{\hat{s}}} d\Omega_3 = \frac{1}{(4\pi)^2} \frac{|\vec{p}_3^{cm}|}{\sqrt{\hat{s}}} d\cos\theta_3 d\phi_3. \quad (3.12)$$

In the center-of-mass frame, we have

$$|\vec{p}_3^{cm}| = |\vec{p}_4^{cm}| = \frac{\lambda^{1/2}(\hat{s}, m_3^2, m_4^2)}{2\sqrt{\hat{s}}}, \quad E_3^{cm} = \frac{\hat{s} + m_3^2 - m_4^2}{2\sqrt{\hat{s}}}, \quad E_4^{cm} = \frac{\hat{s} + m_4^2 - m_3^2}{2\sqrt{\hat{s}}}, \quad (3.13)$$

where the Källén function $\lambda(x, y, z)$, is defined as

$$\lambda(x, y, z) = (x - y - z)^2 - 4yz = x^2 + y^2 + z^2 - 2xy - 2xz - 2yz. \quad (3.14)$$

For the double Higgs production cross section, the initial particles are gluons with $p_{1,2}^2 = 0$ and the final state consists of two identical Higgs particles with $p_{3,4}^2 = m_H^2$. The following parametrisation with $|\vec{p}_3^{cm}| = \sqrt{\hat{s}/4 - m_H^2}$ of the four vectors was used:

$$\begin{aligned} p_{1,2}^\mu &= (\sqrt{\hat{s}}/2, 0, 0, \pm\sqrt{\hat{s}}/2), \\ p_{3,4}^\mu &= (\sqrt{\hat{s}}/2, \pm|\vec{p}_3^{cm}| \sin\theta \cos\phi, \pm|\vec{p}_3^{cm}| \sin\theta \sin\phi, \pm|\vec{p}_3^{cm}| \cos\theta). \end{aligned} \quad (3.15)$$

3.2.2 Three-particle phase space

For the three-particle phase space, where the outgoing particles are labeled by the indices 3, 4 and 5, five independent integration variables remain after applying the delta-constraints from the energy-momentum conservation. The choice of integration variables is not unique. In this work, two different parametrisations were used.

Decay chain

In the case of the production and decay of an intermediate massive particle with mass M it is often advantageous to generate the phase space recursively by observing that

$$d\Phi_n(p; p_1, \dots, p_n) = d\Phi_{n-j-1}(p; q, p_{j+1}, \dots, p_n) \frac{dq^2}{2\pi} d\Phi_j(q; p_1, \dots, p_j) \quad (3.16)$$

with the invariant mass

$$q^2 = \left(\sum_{i=1}^j E_i \right)^2 - \left| \sum_{i=1}^j \vec{p}_i \right|^2 \quad (3.17)$$

of decay products. For the three-particle phase space, we therefore need two different two-particle phase spaces. After boosting into the center-of-mass frame of the decaying particle, and (3.12) can be used. Finally, the 4-momenta are boosted back to the lab frame.

The propagator contribution of an unstable particle of mass M and total width Γ is written as

$$R(q^2) = \frac{1}{(q^2 - M^2)^2 + (M\Gamma)^2}, \quad (3.18)$$

which is the Breit-Wigner resonance. For narrow resonances, i.e. when $\Gamma \ll M$, this peak will significantly delay or even jeopardise the convergence of the numerical integration. In order to avoid this, one employs a transformation for every Breit-Wigner-type resonance in the cross section:

$$\begin{aligned} q^2 &= M^2 + M\Gamma \tan z, \\ dq^2 &= dz \frac{(q^2 - M^2)^2 + (M\Gamma)^2}{M\Gamma}. \end{aligned} \quad (3.19)$$

Therefore, the Jacobian of this transformation cancels the resonant propagator and the convergence of the numerical integration is ensured.

Parametrisation with hadron collider variables

The scattering of two hadrons provides two beams of incoming partons and the spectrum of the longitudinal momenta of these beams is determined by the parton distribution functions. The center of mass system of the parton system is usually boosted with respect to the two incoming hadrons. It is therefore useful to classify the final state in terms of variables which transform simply under longitudinal boosts. For this purpose we introduce the transverse momentum $p_T = \sqrt{p_x^2 + p_y^2}$ and the rapidity y , and a parametrisation of the three-particle phase space in terms of these variables will be shown. The rapidity is defined as

$$y = \operatorname{artanh} \frac{p_z}{p_0} \equiv \frac{1}{2} \ln \frac{p_0 + p_z}{p_0 - p_z}, \quad (3.20)$$

where $p_z = |\vec{p}| \cos \theta$ denotes the fraction of the particle's three-momentum that goes in the direction of the beam axis. Using the rapidity instead of directly taking the angle θ has the advantage that the shape of the rapidity distribution $d\sigma/dy$ stays invariant under a boost in the beam direction. Under this boost, the rapidity is additive and transforms as $y \rightarrow y - \operatorname{artanh} \beta$. The sum of two rapidities when the momenta

point into the same direction is given by the rapidity of the sum of the momenta, via the formula for the addition of relativistic velocities³: $y(p_1) + y(p_2) = y\left(\frac{p_1+p_2}{1+p_1 p_2}\right)$. In experimental analyses often a slightly different measure, the pseudo-rapidity η is used. It is derived from the standard rapidity by taking the limit of a vanishing mass of the particle and is defined as

$$\eta = \frac{1}{2} \ln \frac{1 + \cos \theta}{1 - \cos \theta}. \quad (3.21)$$

It is more convenient experimentally, since the angle θ from the beam direction is measured directly at the detector. The transverse mass $M_T = \sqrt{m^2 + p_T^2}$ rather than p_T is also used, since it is the former quantity which is measured in a hadron calorimeter. Rapidity and pseudorapidity are related via the simple transformation

$$y = \operatorname{artanh} \left(\sqrt{1 - \frac{m^2}{\vec{p}^2 + m^2}} \tanh \eta \right). \quad (3.22)$$

For hadronic cross sections, the partonic cross section has to be convoluted with the parton distribution functions, therefore two additional integrations over the Bjorken variables x_1 and x_2 of the incoming partons occur. For convenience, we include this integration into the phase space integral and therefore compute $dx_1 dx_2 d\Phi_3$.

We use the following parametrisation for the five momenta:

$$\begin{aligned} p_1 &= x_1 E/2 (1, 0, 0, 1), \\ p_2 &= x_2 E/2 (1, 0, 0, -1), \\ p_3 &= (M_{T3} \cosh(y_3), p_{T3} \cos(\phi_3), p_{T3} \sin(\phi_3), M_{T3} \sinh(y_3)), \\ p_4 &= (M_{T4} \cosh(y_4), p_{T4} \cos(\phi_4), p_{T4} \sin(\phi_4), M_{T4} \sinh(y_4)), \\ p_5 &= (M_{T5} \cosh(y_5), p_{T5} \cos(\phi_5), p_{T5} \sin(\phi_5), M_{T5} \sinh(y_5)), \end{aligned}$$

with the azimuthal angles ϕ_i and the center of mass energy E of the hadrons. Another important variable is the distance ΔR , which is used in the cone-algorithm of a jet definition. In this algorithm, a jet is a concentration of transverse mass M_T in a cone of radius R , where

$$\Delta R = \sqrt{(\Delta\eta)^2 + (\Delta\phi)^2}. \quad (3.23)$$

This definition of a jet measure is invariant under longitudinal boosts.

The phase space measure $dp^3/2E$ in terms of the hadron collider variables y, p_T reads

$$\frac{dp^3}{2E} = \frac{1}{2} p_T dp_T d\phi dy = \frac{1}{2} d^2\vec{p}_T dy,$$

³This can be easily seen with the help of the identity $\tanh(y_1 + y_2) = \frac{\tanh y_1 + \tanh y_2}{1 + \tanh y_1 \tanh y_2}$.

and the four constraints from the energy-momentum conservation are given by

$$\begin{aligned} & \delta((x_1 + x_2)E/2 - \sum_{j=3}^5 M_{Tj} \cosh y_j), \\ & \delta^{(2)}(\vec{p}_{T3} + \vec{p}_{T4} + \vec{p}_{T5}), \\ & \delta((x_1 - x_2)E/2 - \sum_{j=3}^5 M_{Tj} \sinh y_j). \end{aligned} \quad (3.24)$$

By adding the arguments of the first and last constraint and using $\delta(ax) = \frac{1}{|a|}\delta(x)$, they can be rewritten as

$$\delta((x_1 + x_2)E/2 - \hat{E}) \delta((x_1 - x_2)E/2 - \hat{p}) = \frac{2}{E^2} \delta(x_1 - \frac{\hat{E}}{E} - \frac{\hat{p}}{E}) \delta(x_2 - \frac{\hat{E}}{E} + \frac{\hat{p}}{E}). \quad (3.25)$$

The integration over \vec{p}_{T5} , x_1 and x_2 is therefore trivial, and we obtain with a factor 2π for the ϕ_3 integration the following compact three-particle phase space parametrisation in terms of six integration variables:

$$dx_1 dx_2 d\Phi_3 = \frac{1}{(2\pi)^4} \frac{1}{4E^2} p_{T3} p_{T4} d\phi_4 dp_{T3} dp_{T4} dy_3 dy_4 dy_5. \quad (3.26)$$

Calculation of multi-leg one-loop amplitudes

4

Efficient techniques for computing tree level amplitudes have been available for several years, for a recent review, see for example [39]. One-loop calculations are considerably more involved, and they form the “bottleneck” to obtaining new results at next-to-leading order (NLO). In principal, it is straightforward to compute tree and loop amplitudes by drawing all Feynman diagrams and evaluating the corresponding analytical expressions. Standard reduction techniques could be applied to the encountered loop integrals. In practice, this will become extremely tedious and inefficient as the number of external legs grows. The complexity of a calculation based on Feynman diagrams grows factorially with the number of external particles. As an example, Table 4.1 shows the number of Feynman diagrams contributing to the process $gg \rightarrow ng$ at tree level, and many of them are related by gauge invariance. Additionally, complicated self-interactions of nonabelian gauge bosons blow up the expressions even further. Going to higher n also leads to a higher number of kinematic invariants, which allows the construction of arbitrarily complicated expressions. At the loop level, the algebra gets considerably more complicated, since there are more diagrams, more off-shell lines and nonabelian vertices. Furthermore, reducing the loop integrals often requires the inversion of matrices which produces spurious kinematic singularities, and leads to very large intermediate expressions, but should cancel in the final result.

4.1 Quantum number management

Due to the long intermediate expressions, computer algebra like MAPLE, MATHEMATICA or FORM [40] has become an essential tool. However, a brute force

n	2	3	4	5	6	7	8
diagrams	4	25	220	2485	34300	559405	10525900

Table 4.1: Number of tree-level Feynman diagrams contributing to $gg \rightarrow ng$.

application alone will still produce lengthy expressions, which are slow and potentially unstable, when evaluated numerically. Therefore, techniques are needed which keep the size of the intermediate expressions under control. It is useful to decompose the quantity to be calculated into simpler pieces and calculate these separately. The organisational framework is called “quantum number management”. First, it is not necessary to square the transition amplitude and sum over the spins and helicities analytically, in order to obtain unpolarised cross sections. It is sufficient to do this numerically at the very end of the calculation. This avoids obtaining $\mathcal{O}(N^2)$ terms from an expression with $\mathcal{O}(N)$ terms. Individual amplitudes have to be calculated in a helicity or spin basis, which is discussed in section 4.1.1. Furthermore, individual helicity amplitudes can be divided into smaller gauge-invariant pieces, called partial amplitudes, which is discussed in section 4.1.2.

4.1.1 Spinor Helicity formalism

The spinor helicity formalism [41, 42, 43] has proven to be a very useful tool for calculations within the framework of massless QCD, since it is largely responsible for extremely compact expressions for tree and loop amplitudes. We begin with fermions, their equations of motion are given by the Dirac equation

$$(\not{p} - m) u(p) = (\not{p} + m) v(p) = 0 \quad \text{and} \quad (4.1)$$

$$\bar{u}(p) (\not{p} - m) = \bar{v}(p) (\not{p} + m). \quad (4.2)$$

In the massless limit, positive and negative energy solutions are identical. Therefore, the solutions of definite helicity

$$u_{\pm}(p) = \Pi_{\pm} u(p) \quad \text{and} \quad (4.3)$$

$$v_{\mp}(p) = \Pi_{\pm} v(p) \quad (4.4)$$

can be identified, where the helicity projection operator is given by

$$\Pi_{\pm} = \frac{1}{2}(\mathbf{1} \pm \gamma_5). \quad (4.5)$$

We use the common bra-ket notation [42]

$$|p_{\pm}\rangle \equiv u_{\pm}(p) = v_{\mp}(p), \quad \langle p_{\pm}| \equiv \bar{u}_{\pm}(p) = \bar{v}_{\mp}(p) \quad (4.6)$$

and define spinor products by

$$\langle pq \rangle \equiv \langle p_- | q_+ \rangle, \quad [pq] \equiv \langle p_+ | q_- \rangle \quad (4.7)$$

which take value in the complex numbers. The orthogonality of the projectors Π_{\pm} leads to the vanishing of products like $\langle p_+ | q_+ \rangle$. The completeness relation reads

$$|p_+\rangle \langle p_+| + |p_-\rangle \langle p_-| = \not{p}, \quad (4.8)$$

and therefore

$$|p_{\pm}\rangle \langle p_{\pm}| = \Pi_{\pm} \not{p}. \quad (4.9)$$

By computing

$$\langle pq \rangle [pq] = \bar{u}(p) \Pi_+ \Pi_+ \not{q} \Pi_- u(p) = \text{tr}(\not{p} \Pi_+ \Pi_+ \not{q} \Pi_-) = 2 p \cdot q \quad (4.10)$$

we observe that the spinor products are, up to a phase, square roots of Lorentz products. A numerical evaluation is possible after choosing a specific representation of Dirac matrices. In the Dirac representation, the spinor products are given by [44]

$$\begin{aligned} \langle pq \rangle &= \sqrt{|s_{pq}|} e^{i\phi_{pq}}, \\ [pq] &= \sqrt{|s_{pq}|} e^{-i(\phi_{pq} + \pi)}, \end{aligned} \quad (4.11)$$

where $s_{pq} = (p + q)^2 = 2 p \cdot q$ and

$$\cos \phi_{pq} = \frac{p_1 q_+ - q_1 p_+}{\sqrt{|s_{pq}|} |p_+ q_+|}, \quad \frac{p_2 q_+ - q_2 p_+}{\sqrt{|s_{pq}|} |p_+ q_+|}, \quad p_+ = p_0 + p_3. \quad (4.12)$$

We can also express polarisation vectors for massless gauge bosons with definite helicity ± 1 by

$$\epsilon_+^{\mu}(k, q) = \frac{\langle q_- | \gamma^{\mu} | k_- \rangle}{\sqrt{2} \langle qk \rangle}, \quad (4.13)$$

$$\epsilon_-^{\mu}(k, q) = \frac{\langle q_+ | \gamma^{\mu} | k_+ \rangle}{\sqrt{2} [kq]}, \quad (4.14)$$

where k is the momentum of the vector boson and q is an arbitrary light-like reference momentum. The dependence on the reference momentum q will drop out in gauge invariant quantities. The completeness relation for these polarisation vectors is that of an light-like axial gauge:

$$\sum_{\lambda=\pm} \epsilon_{\lambda}^{\mu}(k, q) (\epsilon_{\lambda}^{\nu}(k, q))^* = -g^{\mu\nu} + \frac{k^{\mu} q^{\nu} + k^{\nu} q^{\mu}}{k \cdot q}. \quad (4.15)$$

In order to prove that (4.13) is a valid definition of a polarisation vector, some auxiliary properties are needed. The Gordon identity

$$\langle p_{\pm} | \gamma^{\mu} | p_{\pm} \rangle = 2 p^{\mu} \quad (4.16)$$

is used to express light-like vectors by spinor strings. The application of the Fierz rearrangement theorem yields the identity

$$\langle p_{+} | \gamma^{\mu} | q_{+} \rangle \langle r_{+} | \gamma_{\mu} | s_{+} \rangle = 2 [pr] \langle sq \rangle. \quad (4.17)$$

This identity is derived from the expansion of the (4-dim) matrix $|q_{+}\rangle \langle p_{+}|$ into a linear combination of $\mathbf{1}$, γ_{μ} , γ_5 , $\gamma_{\mu}\gamma_5$ and $\gamma_{\mu}\gamma_{\nu}$. It reads

$$2 |q_{+}\rangle \langle p_{+}| = \langle p_{+} | \gamma^{\mu} | q_{+} \rangle \gamma_{\mu} \Pi_{-}. \quad (4.18)$$

Multiplying (4.18) with $\langle r_{+}|$ from the left and $|s_{+}\rangle$ from the right leaves us with (4.17). The charge conjugation relation for vector currents reads

$$\langle q_{\mp} | \gamma^{\mu} | k_{\mp} \rangle = \langle k_{\pm} | \gamma^{\mu} | q_{\pm} \rangle. \quad (4.19)$$

By using (4.16) and (4.17), we can prove the orthogonality condition of the polarisation vectors

$$\epsilon_{\pm}(k, q) \cdot k \propto \langle q_{\mp} | \gamma^{\mu} | k_{\mp} \rangle \langle k_{\mp} | \gamma_{\mu} | k_{\mp} \rangle = -2 [qk] \langle kk \rangle = 0. \quad (4.20)$$

Similarly, one shows

$$\epsilon^{+} \cdot \epsilon^{-} = 0, \quad \epsilon^{\pm} \cdot \epsilon^{\pm} = -1. \quad (4.21)$$

Now we can also prove (4.15). Complex conjugation reverses the helicity of the polarisation vector, $(\epsilon_{\pm}^{\mu})^{*} = \epsilon_{\mp}^{\mu}$, therefore the first term in the sum of (4.15) can be rewritten as traces, yielding

$$\epsilon_{+}^{\mu}(k, q) \epsilon_{-}^{\nu}(k, q) = \frac{1}{2} \left(-g^{\mu\nu} + \frac{k^{\mu} q^{\nu} + k^{\nu} q^{\mu}}{k \cdot q} \right) - \frac{i}{2} \varepsilon^{\rho\mu\sigma\nu} k_{\rho} q_{\sigma}. \quad (4.22)$$

Adding the second term with μ and ν exchanged leads to (4.15). Finally, changing the reference momentum q gives a term proportional to the momentum of the gauge boson,

$$\epsilon_{+}^{\mu}(k, q_1) - \epsilon_{+}^{\mu}(k, q_2) = \sqrt{2} \frac{\langle q_1 q_2 \rangle}{\langle q_1 k \rangle \langle k q_2 \rangle} \times k^{\mu} \quad (4.23)$$

which amounts to an on-shell gauge transformation.

Extension to the massive case

Although the treatment of massive fermions is not part of this thesis, I briefly mention how to extend the formalism. For massive fermions, the spinors $u(p)$ and $v(p)$ have to

be distinguished. The key idea is that any massive vector p can always be decomposed into a sum of two light-like vectors \hat{p} and q :

$$p = \hat{p} + \frac{p^2}{2p \cdot q} q. \quad (4.24)$$

Note that $2kq = 2\hat{k}q$. Using eq. (4.24) we may associate to any four-vector p a massless four-vector \hat{p} . q again denotes an arbitrary light-like reference momentum and is related to the quantisation axis of the spin for the massive fermion. In contrast to the massless gauge bosons, amplitudes with the label $+$ or $-$ will depend on the choice of the reference momentum. The following choice for the spinors of massive fermions satisfies the Dirac equation [39]:

$$\begin{aligned} u_{\pm} &= \frac{1}{\langle \hat{p}_{\mp} | q_{\pm} \rangle} (\not{p} + m) |q_{\pm}\rangle, & \bar{u}_{\pm} &= \frac{1}{\langle q_{\mp} | \hat{p}_{\pm} \rangle} \langle q_{\mp} | (\not{p} + m), \\ v_{\mp} &= \frac{1}{\langle \hat{p}_{\mp} | q_{\pm} \rangle} (\not{p} - m) |q_{\pm}\rangle, & \bar{v}_{\mp} &= \frac{1}{\langle q_{\mp} | \hat{p}_{\pm} \rangle} \langle q_{\mp} | (\not{p} - m). \end{aligned} \quad (4.25)$$

One can also verify the orthogonality condition

$$\bar{u}(\bar{\lambda})u(-\lambda) = 2m\delta_{\bar{\lambda}\lambda}, \quad (4.26)$$

and the completeness relation

$$\sum_{\lambda=+/-} u(-\lambda)\bar{u}(\lambda) = \not{p} + m. \quad (4.27)$$

The extension of the spinor helicity formalism to massive gauge bosons is analogous to the previous case. Again, the momentum of the massive gauge boson is split into two light-like momenta, $k^{\mu} = k_1^{\mu} + k_2^{\mu}$ with $k^2 = m^2, k_1^2 = k_2^2 = 0$. The polarisation vectors $\epsilon_{\pm}^{\mu}(k_1, k_2)$ of the massive gauge boson are given by (4.13), and the longitudinal polarisation vector is given by

$$\epsilon_0^{\mu}(k_1, k_2) = \frac{1}{2m} (\langle k_{1+} | \gamma^{\mu} | k_{1+} \rangle - \langle k_{2+} | \gamma^{\mu} | k_{2+} \rangle). \quad (4.28)$$

By direct computation, one shows that the above definitions satisfy the requirements of a polarisation vector:

$$\epsilon_{\pm,0} \cdot k = 0, \quad \epsilon_{\pm} \cdot \epsilon_{\mp} = \epsilon_0 \cdot \epsilon_0 = -1, \quad \epsilon_0 \cdot \epsilon_{\pm} = 0. \quad (4.29)$$

Similarly, one shows the completeness relation for massive vector bosons:

$$\sum_{\lambda=-,0,+} \epsilon_{\lambda}^{\mu} (\epsilon_{\lambda}^{\nu})^* = -g^{\mu\nu} + \frac{k^{\mu}k^{\nu}}{m^2}. \quad (4.30)$$

4.1.2 Colour decomposition

QCD amplitudes contain group theoretical factors, like the generator T_{ij}^a of the gauge group $SU(N_c)$ from gluon-quark-antiquark vertices or structure constants f^{abc} (defined by $[T^a, T^b] = if^{abc}T^c$) from three-gluon or four-gluon vertices. Gluon- and quark propagators contract many of these indices together with δ_{ab} , δ_{ij} factors. These colour amplitudes can be organised by projecting on a colour basis which separates the amplitude in gauge-invariant sub-amplitudes or partial amplitudes [44, 45, 46]. In the pure gluonic case, the colour decomposition of tree level amplitudes with n external gluons reads

$$\mathcal{A}_n(1, 2, \dots, n) = g^{n-2} \sum_{\sigma \in S_n/Z_n} \text{tr}(T^{a_{\sigma(1)}} \dots T^{a_{\sigma(n)}}) A_n(\sigma(1), \dots, \sigma(n)), \quad (4.31)$$

where the sum is over all non-cyclic permutations of the external gluon legs. The quantities $A_n(\sigma(1), \dots, \sigma(n))$ contain the kinematic information and are colour-ordered, that is, only diagrams with a particular cyclic ordering contribute and are therefore simpler than the complete amplitude. Usually, the number of independent partial amplitudes is reduced by applying symmetries like charge conjugation, which allows one to exchange a quark with an antiquark, or parity, which simultaneously reverses all helicities in an amplitude.

This decomposition is obtained by replacing the structure constants f^{abc} by

$$if^{abc} = 2 [\text{tr}(T^a T^b T^c) - \text{tr}(T^b T^a T^c)], \quad (4.32)$$

using the normalisation $\text{tr}(T^a T^b) = 1/2 \delta^{ab}$. Strings and traces of colour matrices can be simplified with the help of the Fierz identity,

$$T_{ij}^a T_{kl}^a = \frac{1}{2} \left(\delta_{il} \delta_{jk} - \frac{1}{N_c} \delta_{ij} \delta_{kl} \right), \quad (4.33)$$

if external quarks are present. The colour factors for QCD amplitudes containing also quarks in the external states are combinations of open

$$(T^{a_1} \dots T^{a_n})_{i_q j_{\bar{q}}} \quad (4.34)$$

and closed strings

$$\text{tr}(T^{b_1} \dots T^{b_k}) \quad (4.35)$$

of colour matrices. These strings are the building blocks for a basis in colour space and the choice of the basis is not unique.

A second basis is the colour-flow basis [47]. This decomposition is based on treating the gluon field as an $N \times N$ matrix $(A_\mu)^i_j$, ($i, j = 1, \dots, n$) rather than a one-index field A_μ^a , ($a = 1, \dots, N^2 - 1$). The colour basis in this case consists of products of Kronecker deltas δ_{ij} . This choice is especially useful for QCD amplitudes involving many external quarks.

4.2 Dimensional regularisation and Renormalisation

Higher-order corrections to Green functions and S -matrix elements result from Feynman graphs containing loops. This is a conceptual and technical complication because *divergences* occur in the evaluation of loop diagrams. A simple example is the scalar 2-point diagram (Fig. 4.1), which involves the integral

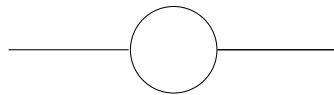


Figure 4.1: Scalar self-energy

$$B_0(p, m_1, m_2) = \frac{1}{i\pi^2} \int d^4k \frac{1}{[(k-p)^2 - m_1^2]} \frac{1}{k^2 - m_2^2}. \quad (4.36)$$

The integral over the loop momentum k extends to infinity and therefore develops an ultraviolet (UV) divergence. Simple power counting shows that the integral is logarithmically divergent in four dimensions. The singularities occurring in loop integrals therefore have to be systematically removed by a renormalisation procedure. A consistent Lorentz- and gauge-invariant prescription for regularising divergent loop integrals is known as conventional dimensional regularisation, which simultaneously regularises ultraviolet [48, 49] and soft and collinear divergences [50]. In this scheme, calculations are performed in $n = 4 - 2\epsilon$ instead of four dimensions. The analytic structure of these integrals allows for an analytic continuation to arbitrary complex n . The UV divergences manifest themselves as poles in ϵ . Changing the dimension of the integral changes also the dimension of $B_0(p, m_1, m_2)$. We compensate this by multiplying with $\mu^{2\epsilon}$, where μ has the dimension of a mass. So, we replace

$$\int \frac{d^4k}{(2\pi)^4} \longrightarrow \mu^{(2\epsilon)} \int \frac{d^n k}{(2\pi)^n} \quad (4.37)$$

in the loop integrals. Additionally, all particle momenta are also set to n dimensions. An explicit calculation of (4.36) in n dimensions for massless internal lines leads to

$$B_0(p, 0, 0) = \left(\frac{4\pi\mu^2}{-p^2} \right)^\epsilon \Gamma(\epsilon) \frac{\Gamma^2(1-\epsilon)}{\Gamma^2(2-2\epsilon)} = \frac{1}{\epsilon} - \gamma_E + \log(4\pi) - \log\left(\frac{-p^2}{\mu^2}\right) + 2. \quad (4.38)$$

The dependence of the unphysical scale μ can now be removed via renormalisation: The Lagrangian of a model contains free parameters, which are not determined by the theory, but have to be taken from experiment. At leading order, these parameters can be identified with physical observables like masses or coupling constants. Higher order corrections from Feynman graphs containing loops change the relations among the parameters of the Lagrangian. As a result, the bare parameters are no longer directly related to physical quantities, they can even become divergent.

These divergent quantities have to be regularised, e.g. by dimensional regularisation. This amounts to a modification of the theory so that the possibly divergent expressions become well-defined, and that in a suitable limit the original (divergent) theory is recovered. Consequently, a redefinition of the original (*bare*) parameters, a *renormalisation* of the theory is needed. In this process, also the fields have to be renormalised.

The requirement that divergences are compensated does not determine the finite parts of the renormalisation constants. As a consequence, calculations in finite orders of perturbation theory performed in different renormalisation schemes may differ by higher-order contributions. In an all-order calculation all different schemes would lead to equivalent relations among physical quantities. The dependence of the choice of the renormalisation scheme and consequences are studied with the help of renormalisation group equations.

The most popular renormalisation approach is multiplicative renormalisation with counterterms. The divergences are absorbed by a simple rescaling of the original (bare) parameters g and fields Ψ , denoted by the subscript 0. They are defined as

$$\Psi_0 = \sqrt{Z_\Psi} \Psi = \left(1 + \frac{1}{2} \delta Z_\Psi^{(1)} - \frac{1}{8} \delta Z_\Psi^{(1)2} + \frac{1}{2} \delta Z_\Psi^{(2)} + \dots \right) \Psi \quad (4.39a)$$

$$g_0 = Z_g g = (1 + \delta Z_g^{(1)} + \delta Z_g^{(2)} + \dots) g. \quad (4.39b)$$

The right-hand side of (4.39) is written as an expansion in orders of perturbation theory. At NLO, only $\delta Z_g^{(1)}$ and $\delta Z_\Psi^{(1)}$ need to be considered. This multiplicative renormalisation does not change the functional dependence of the Lagrangian $\mathcal{L}(\Psi, g)$ on Ψ and g . It leads to the same Feynman rules for the renormalised and parameters as the Lagrangian with the bare quantities. Inserting (4.39), we have

$$\mathcal{L}(g_0, \Psi_0) = \mathcal{L}(g, \Psi) + \mathcal{L}_{\text{ct}}(g, \Psi, Z_g, Z_\Psi), \quad (4.40)$$

where the counterterm Lagrangian \mathcal{L}_{ct} summarises all terms containing the renormalisation constants and generates counterterm Feynman rules. The renormalisation constants will absorb the divergences, up to finite parts. In the mass-independent modified minimal-subtraction scheme $\overline{\text{MS}}$ only the divergences of the form $\Delta = 1/\epsilon - \gamma_E + \log 4\pi$ get subtracted, which is especially convenient for higher-order calculations and best suited for dimensional regularisation.

There are different regularisation prescriptions within dimensional regularisation. All of them have the analytic continuation of the loop momenta into $n \neq 4$ dimensions in common. There is however some freedom for choosing the dimensionality of the momenta of the external particles as well as the number of polarisations of both external and internal particles. Conventional regularisation (CDR) [51] considers $n - 2$ helicity states for massless vector bosons and 2 helicity states for fermions and no distinction is made between virtual and real particles, therefore also the external momenta are defined in n dimensions. This scheme however does not preserve supersymmetry, since the number of bosonic degrees of freedom no longer equals the number of fermionic degrees of freedom, which is a crucial requirement of supersymmetry. In the dimensional reduction scheme (DR) [52], the polarisation of internal and external fields is kept four-dimensional, such that the number of helicity states for both quarks and gluons is 2. This avoids explicit supersymmetry breaking. The number of internal and external dimensions is still n . In a practical one-loop calculation, this prescription works almost like CDR, except that one has to distinguish between four-dimensional metric tensors coming from the Lorentz algebra and n -dimensional metric tensors originating from momentum integrals with more than one loop momentum in the numerator. A modification of DR is the four-dimensional helicity scheme (FDH) [53], also called modern dimensional reduction [54], where the number of external dimensions is no longer n , but 4. A fourth variant is the original choice of 't Hooft and Veltman [48] (HV-scheme), which continues particle momenta and helicities of vector particles inside loops into $n \neq 4$ dimensions, while keeping the momenta and helicities of external particles, as well as fermion helicities inside loops, in four dimensions. The regularisation of infrared divergences, resulting from external particles which are soft or collinear to other external particles is also possible within dimensional regularisation. Like virtual particles, these are not observed, therefore these two classes are grouped as *unobserved* particles. Unitarity requires a uniform treatment of unobserved particles, independent of whether they are internal or external. Table 4.2 summarises the definitions of the various regularisation prescriptions within dimensional regularisation.

The conventional scheme (CDR) is conceptually simpler, as all quantities are continued uniformly to $n = 4 - 2\epsilon$ dimensions. The HV- and the FDH scheme however have practical advantages when using the spinor helicity formalism, which is naturally defined in four dimensions. These schemes do not require the unnecessary work of computing additional ϵ -helicity amplitudes.

The treatment of the Dirac matrix γ_5 , which appears in parity-violating processes,

4 Calculation of multi-leg one-loop amplitudes

	CDR	DR	FDH	HV
# of internal dimensions	d	d	d	d
# of external dimensions	d	d	4	4
# of unobserved vector bosons	$d - 2$	2	2	$d - 2$
# of observed vector bosons	$d - 2$	2	2	2
# of unobserved fermions	2	2	2	2
# of observed fermions	2	2	2	2

Table 4.2: Definitions of regularisation prescriptions in dimensional regularisation

is not well defined within dimensional regularisation. It is well known [51] that the gamma-algebra in n dimensions,

$$\{\gamma^\mu, \gamma^\nu\} = 2g^{\mu\nu} \cdot \mathbf{1}, \quad g_\mu^\mu = n, \quad \{\gamma^\mu, \gamma_5^{(n)}\} = 0 \quad (4.41)$$

is inconsistent with

$$\text{tr}(\gamma^\mu \gamma^\nu \gamma^\rho \gamma^\sigma \gamma_5^{(4)}) \neq 0. \quad (4.42)$$

This condition is necessary, since we need

$$\text{tr}(\gamma^\mu \gamma^\nu \gamma^\rho \gamma^\sigma \gamma_5^{(4)}) = 4i\epsilon^{\mu\nu\rho\sigma}. \quad (4.43)$$

Therefore, the matrix γ_5 cannot be analytically continued to n dimensions and simultaneously requiring the anticommutation with γ^μ .

A scheme which allows for a consistent treatment of γ_5 is for example the HV-scheme. Here, the four-dimensional γ_5 is also used in n dimensions, by splitting the n -dimensional space into an ordinary four-dimensional physical space (denoted by a hat) and an orthogonal $(n - 4)$ -dimensional space (denoted by a tilde) [55],

$$g^{\mu\nu} = \hat{g}^{\mu\nu} + \tilde{g}^{\mu\nu}, \quad k = \hat{k} + \tilde{k}, \quad \gamma^\mu = \hat{\gamma}^\mu + \tilde{\gamma}^\mu. \quad (4.44)$$

The 't Hooft-Veltman algebra is given by

$$\{\gamma^\mu, \gamma_5\} = \begin{cases} 0, & \mu \in \{0, 1, 2, 3\} \\ 2\tilde{\gamma}^\mu \gamma_5, & \text{otherwise,} \end{cases} \quad (4.45)$$

with $\gamma_5 = \frac{i}{4}\epsilon_{\mu\nu\rho\sigma}\hat{\gamma}^\mu\hat{\gamma}^\nu\hat{\gamma}^\rho\hat{\gamma}^\sigma$. Eq.(4.45) can also be read as

$$[\gamma_5, \tilde{\gamma}^\mu] = 0, \quad (4.46)$$

making the trivial behaviour of γ_5 in the non-physical space manifest. These rules are sufficient to perform the n -dimensional Dirac traces involving γ_5 in the numerators of loop-integrals. Note that external momenta p are defined in four dimensions only,

and therefore $p^\mu \gamma_\mu = p^\mu \hat{\gamma}_\mu$ holds.

Care has to be taken in the presence of gauge anomalies [56], where the treatment of γ_5 in the HV-scheme violates certain Ward identities. In fact, the non-existence of a chirally invariant regularisation scheme is the formal origin of these anomalies¹.

4.3 Reduction method for scalar integrals

In this section we will derive a reduction formula for one-loop, scalar N -point functions. If $N \geq 4$ and all legs are off-shell, the integral is finite and can be treated in four dimensions [58]. If at least one external leg is massless, it is infrared divergent and needs a regulator. In the framework of dimensional regularisation four-dimensional methods are not applicable anymore. We work in $n = 4 - 2\epsilon$ dimensions in the following with the external momenta kept in four dimensions.

With the momentum flow as indicated in Fig. 4.2, we define the propagator momenta as $q_l = k - r_l$ with $r_l = p_l + r_{l-1}$ for l from 1 to N and $r_0 = r_N$. Momentum conservation allows to choose $r_N = 0$.

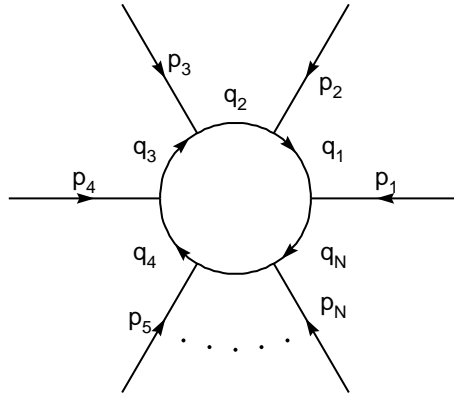


Figure 4.2: N -point graph

¹If a classical symmetry is broken by quantum fluctuations, this is called an anomaly. If they appear in the Noether currents of local gauge theories, they destroy the validity of classical Ward identities which are crucial for the proof of renormalisability. Unitarity and gauge invariance is no longer guaranteed. Theories invariant under charge conjugation or space reflection, like pure Yang-Mills theories, QED and QCD, are free of anomalies related to gauge invariance [57]. The SM is anomaly free due to remarkable fact that the sum of the fermion electric charges in one family (e.g. ν_e, e, u, d) adds up to zero ($0 - 1 + N_c(2/3 - 1/3) = 0$).

The corresponding analytic expression in momentum and Feynman parameter space reads

$$I_N^n(R) = \int \frac{d^n k}{i\pi^{n/2}} \frac{1}{\prod_{l=1}^N (q_l^2 - m_l^2 + i\delta)} = (-1)^N \Gamma(N - \frac{n}{2}) \int_0^\infty d^N z \frac{\delta(1 - \sum_{l=1}^N z_l)}{(-\frac{1}{2} z \cdot S \cdot z - i\delta)^{N-n/2}} \quad (4.47)$$

where R is the *ordered* set containing the propagator labels ($R = (1, \dots, N)$ in Fig. 4.2). This formula is obtained by introducing integrals over Feynman parameters z_l

$$\frac{1}{A_1 A_2 \cdots A_N} = \int_0^1 d^N z \delta(1 - \sum_{l=1}^N z_l) \frac{\Gamma(N)}{[z_1 A_1 + \cdots + z_N A_N]^N} \quad (4.48)$$

and performing the integration over the loop momentum k with the help of

$$\int \frac{d^n k}{i\pi^{n/2}} \frac{1}{(k^2 - \Delta + i\delta)^N} = \frac{\Gamma(N - n/2)}{\Gamma(N)} \frac{(-1)^N}{(\Delta - i\delta)^{N-n/2}}. \quad (4.49)$$

The kinematic information (IR divergences, thresholds) is contained in the matrix S which is related to the Gram matrix G by

$$\begin{aligned} S_{ij} &= (r_i - r_j)^2 - m_i^2 - m_j^2 = G_{ij} - v_i - v_j \\ G_{ij} &= 2r_i \cdot r_j, \quad v_i = r_i \cdot r_i - m_i^2. \end{aligned} \quad (4.50)$$

In general, a one-loop N -point amplitude will contain N -point integrals as well as $(N-1)$, $(N-2)$, \dots , $(N-M)$ -point integrals with tree graphs attached to some of the external legs of the loop integral. The latter are characterised by the omission of some propagators (say j_1, \dots, j_m) of the “maximal” one loop N -point graph. They consist of N external particles and $M < N$ internal lines, where M denotes the number of elements in the set $R \setminus \{j_1, \dots, j_m\}$. We give two examples for pinched graphs, which appear in the reduction of pentagon integrals in Fig. 4.3. The corresponding kinematic matrix is denoted by

$$S^{\{j_1 \cdots j_m\}} \equiv S(R \setminus \{j_1, \dots, j_m\}). \quad (4.51)$$

It is obtained from S by replacing the entries of the rows and columns j_1, \dots, j_m by zero. In this way one can keep track of the pinching of propagators in the iterative application of reduction formulae without changing the labels of the rows and columns of reduced matrices $S^{\{j_1 \cdots j_m\}}$ with respect to the maximal set R .

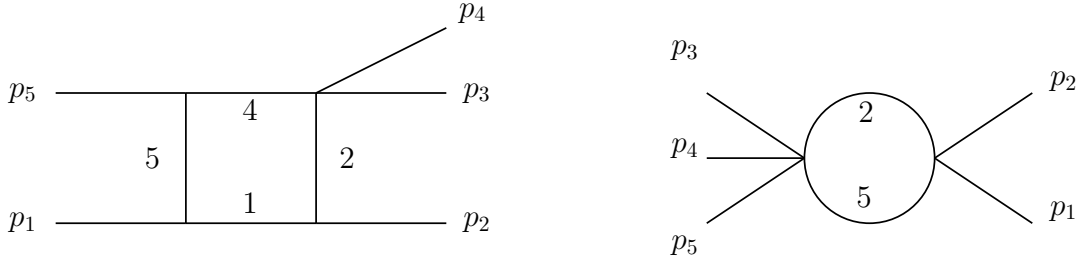


Figure 4.3: Graphical representation of pinch integrals. Each topology defines an ordered set R . The two diagrams correspond to $N = 5$, $M = 4$, $R = \{1, 2, 4, 5\}$ (left), and $N = 5$, $M = 2$, $R = \{2, 5\}$ (right).

For example, for $R = \{1, 2, 3, 4\}$ one has, with $s_j = p_j^2$ and $s_{ij} = (p_i + p_j)^2$:

$$S = \begin{pmatrix} -2m_1^2 & s_2 - m_1^2 - m_2^2 & s_{23} - m_1^2 - m_3^2 & s_1 - m_1^2 - m_4^2 \\ s_2 - m_1^2 - m_2^2 & -2m_2^2 & s_3 - m_2^2 - m_3^2 & s_{12} - m_2^2 - m_4^2 \\ s_{23} - m_1^2 - m_3^2 & s_3 - m_2^2 - m_3^2 & -2m_3^2 & s_4 - m_3^2 - m_4^2 \\ s_1 - m_1^2 - m_4^2 & s_{12} - m_2^2 - m_4^2 & s_4 - m_3^2 - m_4^2 & -2m_4^2 \end{pmatrix} \quad (4.52)$$

The symmetric (4×4) matrix $S^{\{3,4\}}$, which corresponds to the pinching of propagators 3 and 4, is now defined by

$$S^{\{3,4\}} = \begin{pmatrix} -2m_1^2 & s_2 - m_1^2 - m_2^2 & 0 & 0 \\ s_2 - m_1^2 - 2m_2^2 & -2m_2^2 & 0 & 0 \\ 0 & 0 & 0 & 0 \\ 0 & 0 & 0 & 0 \end{pmatrix}. \quad (4.53)$$

Inverse matrices are labelled analogously. To construct the inverse one simply has to invert the sub-matrix of $S^{\{j_1 \dots j_m\}}$ with the zero rows and columns omitted and promote the result back to an $N \times N$ matrix by inserting zeros for the rows and columns $\{j_1, \dots, j_m\}$. In our example one finds, with $\lambda(x, y, z) = x^2 + y^2 + z^2 - 2xy - 2yz - 2xz$:

$$S^{\{3,4\}-1} = \frac{1}{\lambda(s_2, m_1^2, m_2^2)} \begin{pmatrix} 2m_2^2 & s_2 - m_1^2 - m_2^2 & 0 & 0 \\ s_2 - m_1^2 - m_2^2 & 2m_1^2 & 0 & 0 \\ 0 & 0 & 0 & 0 \\ 0 & 0 & 0 & 0 \end{pmatrix}. \quad (4.54)$$

In the following, $S^{-1}(R \setminus \{j_1, \dots, j_m\}) = S^{\{j_1, \dots, j_m\}-1}$ has to be understood in this sense.

The aim of the reduction is to split the integral into an infrared safe part and a remainder that contains all possible sources for infrared singularities. As an ansatz

we write (4.47) as a sum of (one-propagator) reduced diagrams and a remainder,

$$I_N^n = I_{div} + I_{fin} = \int \frac{d^n k}{i\pi^{n/2}} \frac{\sum_{l=1}^N b_l D_l}{\prod_{l=1}^N D_l} + \int \frac{d^n k}{i\pi^{n/2}} \frac{[1 - \sum_{l=1}^N b_l D_l]}{\prod_{l=1}^N D_l} \quad (4.55)$$

where $D_l = q_l^2 - m_l^2 + i\delta$ is the l 'th propagator. The first term in (4.55) is a sum of pinched integrals, where one of the propagators in the loop integral is omitted.

$$I_{div}(R) = \sum_{l \in R} b_l(R) I_{N-1}^n(R \setminus \{l\}) \quad (4.56)$$

In the second term of (4.55), we again introduce Feynman parameters by applying (4.48) and shifting the origin of the integration momentum by $k \rightarrow k - Q$; $Q = \sum_{l \in R} z_l r_l$. The denominator can be written, as usual, in the quadratic form $k^2 - \frac{1}{2} z \cdot S \cdot z$, while the numerator becomes

$$\mathcal{N} = 1 - \sum_l b_l (k^2 - 2k \cdot r_l + r_l \cdot r_l + 2k \cdot Q + Q^2 - 2Q \cdot r_l - m_l^2). \quad (4.57)$$

Terms linear in the integration momentum vanish under symmetric integration, and after a bit of algebra, we obtain

$$\mathcal{N} = - \left(\sum_l b_l \right) \left(k^2 + \frac{1}{2} z \cdot S \cdot z \right) + \sum_l x_l (1 + (S \cdot b)_l). \quad (4.58)$$

Now we can choose the $b_l(R)$, which are still undetermined, such that the second term in (4.58) vanishes. The b_l , $l \in \{1, \dots, N\}$ therefore satisfy the condition

$$(S \cdot b)_l = -1, \quad l = 1, \dots, N. \quad (4.59)$$

By defining the shorthand notation $B(R) = \sum_{l \in R} b_l(R)$ we have

$$I_{fin}(R) = -B(R) \Gamma(N) \int d^N z \delta(1 - \sum_{l=1}^N z_l) \int \frac{d^n k}{i\pi^{n/2}} \frac{(k^2 - \frac{1}{2} z \cdot S \cdot z)}{[k^2 + \frac{1}{2} z \cdot S \cdot z + i\delta]^N}. \quad (4.60)$$

Carrying out the momentum integration by using (4.49) and (4.49) with $N \rightarrow N + 1$ leaves us with the final expression

$$I_{fin}(R) = -B(R)(N - n - 1) I_N^{n+2}(R). \quad (4.61)$$

The $(6 - 2\epsilon)$ -dimensional is infrared finite, as can be seen by a power-counting argument in the corresponding momentum integral.

It remains to solve (4.59). In the case of $2 \rightarrow N$ scattering with $N \leq 6$ and a non-singular matrix S , the solution is simply given by

$$b_i(R) = - \sum_{k \in R} (S^{-1})_{ki}. \quad (4.62)$$

If the b_i belong to a reduced kinematic matrix $S^{\{j\}}$ where the j^{th} row and column is zero, associated with the set $R \setminus \{j\}$, one has $b_i(R \setminus \{j\}) = \sum_{k \in R \setminus \{j\}} (S^{\{j\}})^{-1}_{ki}$. For simplicity of notation, we introduce the shorthand $b_i(R \setminus \{j\}) = b_i^{\{j\}}$, and correspondingly $B^{\{j\}}$ is defined as

$$B^{\{j\}} = \sum_{i \in R \setminus \{j\}} b_i^{\{j\}}. \quad (4.63)$$

Note that in the case of $N = 5$, I_{fin} contains a factor $(N - 1 - n)$ which is $\mathcal{O}(\epsilon)$. As is well known, pentagon integrals are just a sum of box integrals up to a remainder which drops out in phenomenological applications, since $I_5^{n+2}(R)$ is both infrared and ultraviolet finite. In the case $N > 6$, (4.59) does not have a unique solution. The most general solution in this case can be constructed by means of pseudo-inverse matrices. These also called "Moore-Penrose" inverse matrices [59] define the inversion of a general $m \times n$ matrix.

A pseudo inverse H to G is defined by the conditions $HGH = H$ and $GHG = G$. Solutions to the linear equation $G \cdot x = y$ can be found in the form of $x = H \cdot y$, even if G is not an invertible matrix. Since this formalism is not needed for the scattering processes considered in this thesis, I refer to the literature for details [60].

For $N \leq 6$ and $\det S \neq 0$ the following relation [60, 61] holds

$$\sum_{l=1}^N b_l = - \frac{\det G}{\det S}, \quad (4.64)$$

which shows that the vanishing of the finite remainder terms in (4.61) is related to the vanishing of the Gram determinant.

To conclude this section, let us briefly review what we have gained. The reduction algorithm for scalar N -point integrals splits the integrals into a infrared finite, higher dimensional part and a sum of simpler, $N - 1$ -point integrals carrying the infrared divergences:

$$I_N^n(R) = \sum_{l \in R} b_l(R) I_{N-1}^n(R \setminus \{l\}) - B(R)(N - n - 1) I_N^{n+2}(R). \quad (4.65)$$

By iteration of (4.65) arbitrary N -point integrals can be reduced to n -dimensional triangle functions and $(n + 2)$ dimensional box functions. The determinant relation (4.64) shows that the application of (4.65) introduces inverse Gram determinants

through the $1/B$ terms.

4.4 Reduction method for tensor integrals

4.4.1 Form factor representation for tensor integrals

Before discussing the reduction of tensor integrals I introduce the form factor representation A rank r , N -point tensor integral is defined by

$$I_N^{\mu_1 \dots \mu_r}(R) = \int \frac{d^n k}{i\pi^{n/2}} \frac{k^{\mu_1} \dots k^{\mu_r}}{\prod_{j=1}^N D_j} \quad (4.66)$$

The Lorentz structure of the integrals will be carried by the metric tensor $g^{\mu\nu}$ and the r_i^μ -vectors, which are sums of the external momenta p_i^μ . Tensor integrals are expressible by linear combinations of such Lorentz tensors and form factors denoted by $T_{00}^{N,r}$, $T_{j_1}^{N,r}$, $T_{00j_1j_2}^{N,r}$, etc. $T_{00}^{N,r}$ is the coefficient of the Lorentz structure containing only the metric tensor, an index j in the other form factors indicates the appearance an r -vector. We illustrate the notation for pentagon tensor integrals, $N = 5$.

$$\begin{aligned} I_5^{\mu_1} &= \sum T_{j_1}^{5,1} r_{j_1}^{\mu_1} \\ I_5^{\mu_1 \mu_2} &= T_{00}^{5,2} g^{\mu_1 \mu_2} \sum T_{j_1 j_2}^{5,2} r_{j_1}^{\mu_1} r_{j_2}^{\mu_2} \\ I_5^{\mu_1 \mu_2 \mu_3} &= \sum T_{00 j_3}^{5,3} (g^{\mu_1 \mu_2} r_{j_3}^{\mu_3} + 2 \text{ perm.}) \\ &+ \sum T_{j_1 j_2 j_3}^{5,3} r_{j_1}^{\mu_1} r_{j_2}^{\mu_2} r_{j_3}^{\mu_3} \\ I_5^{\mu_1 \mu_2 \mu_3 \mu_4} &= T_{0000}^{5,4} (g^{\mu_1 \mu_2} g^{\mu_3 \mu_4} + 2 \text{ perm.}) \\ &+ \sum T_{00 j_3 j_4}^{5,4} (g^{\mu_1 \mu_2} r_{j_3}^{\mu_3} r_{j_4}^{\mu_4} + 2 \text{ perm.}) \\ &+ \sum T_{j_1 j_2 j_3 j_4}^{5,4} (r_{j_1}^{\mu_1} r_{j_2}^{\mu_2} r_{j_3}^{\mu_3} r_{j_4}^{\mu_4}) \end{aligned} \quad (4.67)$$

4.4.2 Tensor reduction through recursion relations

In this section, we show that any rank r , N -point integral can be expressed in terms of scalar box, triangle and two-point integrals by using scalar reduction and recursion relations. A generalisation of (4.49) reads

$$\int \frac{d^n k}{i\pi^{n/2}} \frac{k^{\mu_1} \dots k^{\mu_{2m}}}{(k^2 - \Delta)^N} = (-1)^N \left[g_{(m)} \right]^{\{\mu_1 \dots \mu_{2m}\}} \left(-\frac{1}{2} \right)^m \frac{\Gamma(N - (n + 2m)/2)}{\Gamma(N)} (\Delta)^{-N + \frac{(n+2m)}{2}}, \quad (4.68)$$

which can be obtained by replacing and even number of the loop momenta in the numerator by replacement rules of the form

$$\begin{aligned} k^{\mu_1} k^{\mu_2} &\rightarrow \frac{1}{n} k^2 g^{\mu_1 \mu_2} \\ k^{\mu_1} k^{\mu_2} k^{\mu_3} k^{\mu_4} &\rightarrow \frac{1}{n(n+2)} (k^2)^2 (g^{\mu_1 \mu_2} g^{\mu_3 \mu_4} + g^{\mu_1 \mu_3} g^{\mu_2 \mu_4} + g^{\mu_1 \mu_4} g^{\mu_2 \mu_3}). \end{aligned} \quad (4.69)$$

Odd powers of the loop momentum can be dropped due to symmetric integration. After introducing Feynman parameters, shifting the loop momentum as before and performing the loop momentum integration, the formula for tensor integrals reads

$$I_N^{\mu_1 \dots \mu_r} = \sum_{m=0}^{[r/2]} \left(-\frac{1}{2}\right)^m \sum_{j_1, \dots, j_{r-2m}=1}^{N-1} [g_{(m)}^{\ddot{\cdot}} r_{j_1}^{\dot{\cdot}} \dots r_{j_{r-2m}}^{\dot{\cdot}}]^{\{\mu_1 \dots \mu_r\}} I_N^{n+2m}(j_1, \dots, j_{r-2m}). \quad (4.70)$$

$[r/2]$ is the nearest integer less or equal to $r/2$ and $[g_{(m)}^{\ddot{\cdot}} r_{j_1}^{\dot{\cdot}} \dots r_{j_{r-2m}}^{\dot{\cdot}}]^{\{\mu_1 \dots \mu_r\}}$ stands for the sum over all different combinations of r Lorentz indices distributed to m metric tensors and $(r-2m)$ r -vectors. These are $\binom{r}{2m} \prod_{k=1}^m (2k-1)$ terms. A dot appearing as an index at objects inside a square bracket stands for one index out of the set specified in curly brackets at the outside of the square bracket. $X^{(m)}$ or $X_{(m)}$ denotes the product of m terms of X with adequate indices². For example, a tensor object like $[X_{(2)}^{\ddot{\cdot}} Y^{\dot{\cdot}}]^{\{\mu_1 \mu_2 \mu_3 \mu_4 \mu_5\}}$ with X a symmetric tensor of rank 2 and Y a vector means

$$[X_{(2)}^{\ddot{\cdot}} Y^{\dot{\cdot}}]^{\{\mu_1 \mu_2 \mu_3 \mu_4 \mu_5\}} = (X^{\mu_1 \mu_2} X^{\mu_3 \mu_4} + X^{\mu_1 \mu_3} X^{\mu_2 \mu_4} + X^{\mu_1 \mu_4} X^{\mu_2 \mu_3}) Y^{\mu_5} + 5 \text{ permutations.}$$

Two examples for pentagon integrals will illustrate the procedure. But first, we have to deal with $I_N^n(j_1, \dots, j_r)$, which are scalar integrals with Feynman parameters in the numerator, defined by

$$I_N^n(j_1, \dots, j_r) = (-1)^N \Gamma(N - n/2) \int_0^\infty d^N z \delta(1 - \sum_{l=1}^N z_l) \frac{z_{j_1} \dots z_{j_r}}{(z \cdot S \cdot z)^{N-n/2}} \quad (4.71)$$

Recursion relations for these kind of integrals are derived in [60] and only the result is presented:

$$I_N^n(j_1, \dots, j_r; R) = \sum_{k=2}^r S_{j_1 j_k}^{-1} I_N^{n+2}(j_2, \dots, j_{k-1}, j_{k+1}, \dots, j_r; R)$$

²The ‘‘power’’ (m) may appear as a lower index for convenience of notation if it would interfere with the dots standing for upper indices. Hence we write $X_{(m)}^{\ddot{\cdot}}$ instead of $(X^{\ddot{\cdot}})^{(m)}$.

$$-b_{j_1}(N-n-r)I_N^{n+2}(j_2, \dots, j_r; R) - \sum_{j=1}^N S_{j_1 j}^{-1} I_{N-1}^n(j_2, \dots, j_r; R \setminus \{j\}). \quad (4.72)$$

This equation shows that all Feynman parameter integrals with nontrivial numerators can be reduced to ordinary scalar integrals by iteration. In each reduction step the highest dimension that appears in an integral is increased by 2. These integrals then can be brought back to the standard basis by reverse application of (4.65). Notice that the reduction involving the inverse of (4.65) is the only source for $1/B$ terms, i.e. for inverse Gram determinants.

Two examples

We illustrate the presented reduction method of one-loop integrals by two examples. In the scattering processes considered in this thesis, pentagon integrals with one or two loop momenta appear, therefore the tensor coefficients $T_{j_1}^{5,1}$, $T_{00}^{5,2}$ and $T_{j_1 j_2}^{5,2}$ have to be known for $N=5$. For the rank 1 pentagon integral, we apply (4.70) and (4.72) and obtain

$$I_5^\mu(R) = \sum_{j \in R} I_5^n(j; R) r_j^\mu = \sum_{k \in R} S_{jk}^{-1} I_4^n(R \setminus \{k\}). \quad (4.73)$$

Now we can express the n -dimensional box integral via (4.65) by a $n+2$ -dimensional box integral and a sum of four triangle integrals. The tensor coefficient therefore reads

$$T_j^{5,1}(R) = I_5^n(j; R) = - \sum_{k \in R} S_{jk}^{-1} B^{\{k\}} I_4^{n+2}(R \setminus \{k\}) - \sum_{k \in R} \sum_{l \in R \setminus \{k\}} S_{jk}^{-1} b_l^{\{k\}} I_3^n(R \setminus \{k, l\}). \quad (4.74)$$

For the rank 2 tensor coefficients we apply the same algorithm and additionally use the fact that for general N -point kinematics with $N \geq 5$, the metric tensor $g^{\mu\nu}$ in 4 dimensions is expressible by a tensor product of (4-dimensional) external momenta, which span a basis of the Minkowski space. With (4.70) and (4.72), the integral decomposes into

$$I_5^{\mu\nu}(R) = -\frac{1}{2}g^{\mu\nu} I_5^{n+2}(R) + \sum_{j_1, j_2} I_5^n(j_1, j_2; R) r_{j_1}^\mu r_{j_2}^\nu. \quad (4.75)$$

The integral $I_5^n(j_1, j_2; R)$ with two Feynman parameters is now reduced to integrals with trivial numerators via twice application of (4.72), the appearing $(n+4)$ -dimensional scalar integral I_5^{n+4} is reduced to a sum of lower-dimensional integrals by (4.65),

$$(2-n)I_5^{n+4}(R) = -\frac{1}{B}I_5^{n+2}(R) - \sum_l b_l I_4^{n+2}(R \setminus \{l\}). \quad (4.76)$$

Collecting only the pentagon integrals I_5^{n+2} , we get

$$I_5^{\mu\nu} = I_5^{n+2} \left\{ -\frac{1}{2}g^{\mu\nu} + \sum_{j_1 j_2} \left(S_{j_1 j_2}^{-1} + \frac{b_{j_1} b_{j_2}}{B} \right) r_{j_1}^\mu r_{j_2}^\nu \right\} + I_{N<5}\text{-integrals}. \quad (4.77)$$

The proof of the vanishing of the curly brackets in (4.77) with a four-dimensional metric tensor $g_{[4]}^{\mu\nu}$ is straightforward: One has to contract the tensor with $4r_{\mu,k}r_{\nu,l}$, use the relation $G_{ij} = S_{ij} - S_{Nj} - S_{Ni} + S_{NN}$ and (4.59). In n dimensions, a tensor structure of $\mathcal{O}(\epsilon)$ occurs, which is defined as the difference of two tensors in n and 4 dimensions. Contracting such differences with kinematical objects like external momenta, polarisation vectors or fermion currents will always lead finally to scalar quantities of $\mathcal{O}(\epsilon)$, which can be neglected in phenomenological applications at one loop.

The tensor coefficient $T_{00}^{5,2}$ is therefore given by the pinched box integrals in (4.76),

$$T_{00}^{5,2} = -\frac{1}{2} \sum_{j \in R} b_j I_4^{n+2}(R \setminus \{j\}) + \mathcal{O}(\epsilon). \quad (4.78)$$

Computing the rank 2 tensor coefficients containing the r -vectors is now straightforward. They are obtained by repeated application of (4.72) on $I_5^n(j_1, j_2)$. The result is given by a combination of 5 box integrals and 20 triangle integrals and reads

$$\begin{aligned} T_{j_1 j_2}^{5,2}(R) = & - \sum_{l \in R} \left(S_{l j_1}^{-1} b_{j_2} + S_{l j_2}^{-1} b_{j_1} - 2 S_{j_1 j_2}^{-1} b_l + b_l S_{j_1 j_2}^{\{l\}-1} \right) I_4^{n+2}(R \setminus \{l\}) \\ & + \frac{1}{2} \sum_{l \in R} \sum_{k \in S \setminus \{l\}} \left(S_{l j_2}^{-1} S_{k j_1}^{\{l\}-1} + S_{l j_1}^{-1} S_{k j_2}^{\{l\}-1} \right) I_3^n(R \setminus \{l, k\}), \end{aligned} \quad (4.79)$$

where the additional relation C.101 in [62] was used. Although not needed in this work, it is interesting to mention that for N -point integrals with $N \geq 5$, higher than $n = 4 - 2\epsilon$ dimensional integrals can be avoided under the condition that the external kinematics is defined in 4 dimensions. This allows to write the metric tensor as a linear combination of four linearly independent external vectors, which is the case for $N \geq 5$. As is shown in [62], tensor integrals with $N \geq 6$ can be iteratively reduced to 5-point integrals, and therefore form factors with $N \geq 5$ are not needed. The case $N = 5$ is, in a sense, the most complicated one. Therefore, *arbitrary* N -point tensor integrals can be reduced to scalar integrals, and the endpoints of the reduction can be chosen as $I = \{I_2^n(R), I_3^n(R), I_4^{n+2}(R)\}$, which are known algebraically.

As it is clear from the above reduction formulae, tensor integrals are written as a linear combination of many tensor coefficients, which are themselves a complicated combination of the basis integrals. This leads to very large expressions in the intermediate steps of the amplitude reduction. Even after applying simplification algorithms,

the final result can still be too complicated for a numerically fast evaluation of the algebraic expressions. Also the vanishing of inverse Gram determinants in certain regions of phase space can lead to numerical instabilities when integrating over the phase space. Cancellations of Gram determinants among gauge invariant subsets of Feynman diagrams potentially soften the numerical instabilities. Nevertheless, this doesn't guarantee numerical stability. A possible solution is to stop the tensor reduction at the point where inverse Gram determinants, the $1/B$ -terms, are introduced. This leads to basis functions which now also include the above integrals with up to three Feynman parameters in the numerators, which have to be evaluated numerically. The prize to pay for the increased numerical stability is a significant slow-down of the evaluation of the amplitude. Details on this method, which is not used for the processes considered in this thesis, can be found in [62].

Gluon induced multi-Higgs production

5

5.1 Introduction

In order to establish the Higgs mechanism and confirm the Higgs sector of the SM, the discovery of a Higgs-like boson is not sufficient. In addition, the predicted couplings of fermions and gauge bosons to the Higgs boson, as well as the trilinear and quartic Higgs self-couplings need to be confirmed experimentally. While Higgs-fermion and Higgs-gauge boson couplings are measurable with accuracies of 10–40% at the LHC [63] and in many channels considerably better at the International Linear Collider (ILC) [64], the measurement of the trilinear and quartic Higgs self-couplings, which are probed in double and triple Higgs boson production, respectively, are more challenging. For low Higgs masses not too much above the LEP limit ($m_H \lesssim 140$ GeV), the largest rates are obtained with the decay channel $H \rightarrow b\bar{b}$ dominating in this mass regime. Unfortunately, at the LHC this search channel is not viable, because of an overwhelming QCD background. The ILC, however, would allow the measurement of the trilinear Higgs self-coupling to a precision of 20-30% in the low Higgs mass regime [64, 65, 66, 67]. We note that in this regime a photon collider promises an even better determination of the trilinear Higgs coupling [68, 69, 70]. For higher Higgs masses, the ILC production cross section decreases due to the reduced phase space. However, in this mass region, the vector boson pair decay channels open up and allow for leptonic signatures that can be separated from the backgrounds at the LHC [64, 71, 72, 73, 74, 75].

The dominant production mechanism for Higgs boson pairs at the LHC is gluon fusion. We note that Higgs production in hadronic collisions can also proceed through bottom quark fusion, $b\bar{b} \rightarrow nH$, but in the SM the corresponding LO as well as NLO [76] cross sections are negligible. In the MSSM, however, enhanced Yukawa couplings can lead to comparable cross sections for gluon and bottom quark fusion [77].

The gluon fusion loop amplitude was first presented in [78]. For neutral Higgs boson pairs in the Minimal Supersymmetric Standard Model (MSSM) the top/bottom-loop contribution was evaluated in [79, 80]. Charged Higgs boson pairs including squark effects were studied in [81]. Although the SM cross section for triple Higgs boson

production at the LHC can be expected to be small [65, 66], this expectation has to be verified through explicit calculation. Only recently, a full calculation of the process $gg \rightarrow HHH$ appeared in the literature [82] and confirmed that SM cross sections are indeed too small to be observable at the LHC. However, it has to be stressed that multi-Higgs boson production rates are very sensitive to physics beyond the Standard Model (BSM) and should be scrutinised carefully in high energy experiments, as they might point to new physics at high energy scales that are not directly accessible at the given collider [83, 84]. A non-standard heavy quark that receives its mass via the Higgs mechanism does not decouple [85], and therefore leads to a nonvanishing contribution in heavy quark loop-induced processes. Furthermore, contributions of higher dimensional operators might alter the SM cross section considerably [86]. Also, in certain Little Higgs Models the Higgs pair production cross section is significantly different from the SM cross section [87].

In this chapter, we present our calculation of double and triple Higgs boson production via gluon fusion. This provides an independent check of the recent calculation in [82], which employed different computational methods and tools. To go beyond the findings of [82], we study higher dimensional operator effects on production rates relative to the SM. The corresponding couplings are in principle only restricted by unitarity constraints [88]. We also analyse amplification effects in supersymmetric (SUSY) two-Higgs-doublet models (2HDMs).

5.2 Higgs boson properties

The SM Higgs mechanism provides fundamental mass terms for massive vector bosons and fermions. The coupling strength of the Higgs boson is proportional to the mass (squared) of the interacting fermion (gauge boson). The SM Higgs boson self interactions, induced by the scalar potential

$$V = \frac{m_H^2}{2v^2} \left(\Phi^\dagger \Phi - \frac{v^2}{2} \right)^2, \quad (5.1)$$

are also proportional to the Higgs mass squared. In unitary gauge one has

$$V = \frac{m_H^2}{2} H^2 + \frac{\lambda_3}{3!} H^3 + \frac{\lambda_4}{4!} H^4 \quad (5.2)$$

with

$$\lambda_4 = \lambda_3/v = \frac{3m_H^2}{v^2}. \quad (5.3)$$

Relation (5.3) between the trilinear and quartic Higgs self couplings is a genuine SM prediction. To establish the SM Higgs mechanism, it has to be verified experimentally.

As already pointed out, the discovery of the Higgs boson and the measurement of its couplings to fermions and gauge bosons by itself are not sufficient.

In general, the Higgs self-couplings change in extensions of the SM. By allowing for higher dimensional operators of the type

$$\sum_{k=1}^{\infty} \frac{g_k}{\Lambda^{2k}} \left(\Phi^\dagger \Phi - \frac{v^2}{2} \right)^{2+k}, \quad (5.4)$$

the constraint (5.3) is relaxed. Magnitude and sign of λ_3 and λ_4 can be arbitrary up to constraints imposed by unitarity. In order to guarantee the stability of the vacuum, only the sign of the highest power of the Higgs field has to be positive. We note that the addition of singlet Higgs fields preserves relation (5.3), but may lead to invisible Higgs boson decays and diluted Higgs signals [89].

The ability to measure the Higgs self-couplings depends on the size of multi-Higgs boson cross sections. As will be discussed below, SM rates are very small at the LHC (see also [82]). It is thus interesting to consider extensions of the SM that allow for amplified event rates. For Higgs pair production in gluon fusion this has been studied in [79] in the context of the MSSM. Two amplification sources have been identified. Firstly, the top and bottom Yukawa couplings are altered due to the mixing of the Higgs fields. In the MSSM one has, at tree level,

$$\begin{aligned} \lambda_{ht\bar{t}} &= \frac{m_t \cos \alpha}{v \sin \beta}, \\ \lambda_{hb\bar{b}} &= -\frac{m_b \sin \alpha}{v \cos \beta}, \end{aligned} \quad (5.5)$$

where

$$\tan \beta = \frac{v_2}{v_1} \quad \text{and} \quad \alpha = \frac{1}{2} \arctan \left(\frac{M_A^2 + M_Z^2}{M_A^2 - M_Z^2} \tan 2\beta \right), \quad -\frac{\pi}{2} \leq \alpha \leq 0. \quad (5.6)$$

Here, v_1 (v_2) is the vacuum expectation value of the Higgs doublet with weak hypercharge $-\frac{1}{2}$ ($+\frac{1}{2}$). For sufficiently large $\tan \beta$, the bottom-loop contribution to the cross section becomes sizable in comparison to the top-loop contribution, leading to a larger production rate. Secondly, internal Higgs propagators can become resonant thereby enhancing the production rate. Both effects generally play a role in 2HDMs, as will be discussed and quantified for triple Higgs boson production below.

We will now briefly review the features of 2HDMs that are important for our purposes. The general potential of the 2HDM is given by [90, 91]

$$\begin{aligned} V(\Phi_1, \Phi_2) &= m_{11}^2 \Phi_1^\dagger \Phi_1 + m_{22}^2 \Phi_2^\dagger \Phi_2 - (m_{12}^2 \Phi_1^\dagger \Phi_2 + \text{h.c.}) \\ &+ \frac{\lambda_1}{2} (\Phi_1^\dagger \Phi_1)^2 + \frac{\lambda_2}{2} (\Phi_2^\dagger \Phi_2)^2 + \lambda_3 (\Phi_1^\dagger \Phi_1) (\Phi_2^\dagger \Phi_2) + \lambda_4 (\Phi_1^\dagger \Phi_2) (\Phi_2^\dagger \Phi_1) \end{aligned}$$

$$+ \left\{ \frac{\lambda_5}{2} (\Phi_1^\dagger \Phi_2)^2 + [\lambda_6 (\Phi_1^\dagger \Phi_1) + \lambda_7 (\Phi_2^\dagger \Phi_2)] (\Phi_1^\dagger \Phi_2) + \text{h.c.} \right\}, \quad (5.7)$$

with the complex Higgs-doublet fields acquiring the vacuum expectation values v_1 and v_2 . After diagonalising the mass matrix one obtains the physical Higgs fields h, H, A, H^\pm and the Goldstone bosons G^\pm, G . We are interested in the Higgs self-couplings, which can be written in terms of the dimensionless parameters λ_i , $i = 1, \dots, 7$, appearing in (5.7). For the quartic couplings, one has

$$\begin{aligned} \lambda_{hhhh} &= 3 \cos^4 \alpha \lambda_2 + 3 \sin^4 \alpha \lambda_1 + 6 \cos^2 \alpha \sin^2 \alpha (\lambda_3 + \lambda_4 + \lambda_5) \\ &\quad - 12 \cos^3 \alpha \sin \alpha \lambda_7 - 12 \sin^3 \alpha \cos \alpha \lambda_6, \\ \lambda_{Hhhh} &= -3 \cos \alpha \sin^3 \alpha \lambda_1 + 3 \cos^3 \alpha \sin \alpha \lambda_2 - \frac{3}{2} \cos 2\alpha \sin 2\alpha (\lambda_3 + \lambda_4 + \lambda_5) \\ &\quad + 3(3 \cos^2 \alpha \sin^2 \alpha - \sin^4 \alpha) \lambda_6 + 3(\cos^4 \alpha - 3 \cos^2 \alpha \sin^2 \alpha) \lambda_7, \end{aligned}$$

to be multiplied by M_Z^2/v^2 . In the MSSM, the Higgs sector is constrained such that only two of the seven input parameters are free. Choosing $\tan \beta$ and $M_A = \lambda_6 v^2$ as basic input, one recovers the MSSM values

$$\begin{aligned} \lambda_{hhhh} &= 3 \cos^2 2\alpha, \\ \lambda_{Hhhh} &= 3 \cos 2\alpha \sin 2\alpha. \end{aligned} \quad (5.8)$$

As is well known, radiative corrections in the Higgs sector are large. The largest ubiquitous correction is given by $3 G_F m_t^4 / (\sqrt{2} \pi^2 \sin^2 \beta) \cdot \ln(m_t^2/m_t^2)$. In our numerical analysis for the MSSM all one-loop and leading two-loop corrections to Higgs masses and couplings are included [25, 92]. For a discussion about reconstructing the Higgs potential in the SUSY case, see [93].

5.3 Calculation

From a computational point of view loop amplitudes with five or more external legs are challenging due to their combinatorial complexity. We employ the reduction techniques introduced in chapter 4 which leads to a numerically stable algebraic representation of the amplitude.

5.3.1 Structure of the amplitude

The production processes $pp \rightarrow hh$ and $pp \rightarrow hhh$ proceed at the parton level via gluon fusion in combination with a quark loop. Here h stands for the Higgs boson of the SM or the light CP-even Higgs boson of the MSSM. Squarks in the loop have been neglected. Their contributions vanish for large squark masses, due to their decoupling

property. In the SM, only the top quark loop leads to a non-negligible cross section at the LHC. For triple Higgs boson production,

$$g(p_1, \lambda_1) + g(p_2, \lambda_2) \rightarrow h(p_3) + h(p_4) + h(p_5) , \quad (5.9)$$

with p_i defining the 4-momenta and $\lambda_{1,2}$ specifying the gluon helicities, the Feynman diagrams are classified in Fig. 5.1. On the diagrammatic level 3-, 4- and 5-point topologies can be distinguished. Each topology involves a different combination of

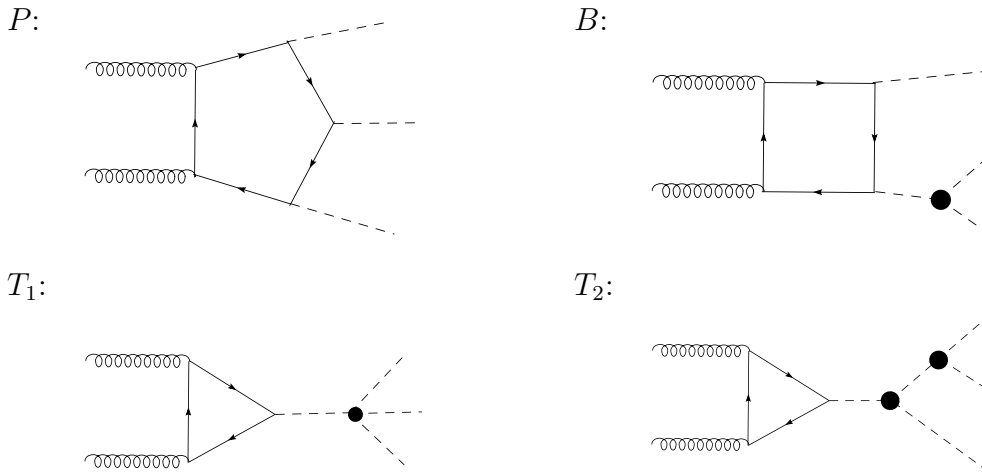


Figure 5.1: Illustration of different topologies to the process $gg \rightarrow HHH$.

coupling constants. Here, we only discuss the structure of the SM amplitude. In 2HDMs one has additional tree structures from the heavy Higgs boson H attached to the quark loop. The pentagon topology P contains no Higgs self-coupling. The box topologies B are proportional to λ_3 , whereas the triangle topologies T_1 and T_2 are proportional to λ_4 and λ_3^2 , respectively. Subsequently, the amplitude can be expressed as

$$\Gamma(gg \rightarrow hhh) = \delta_{ab} T_R \frac{\alpha_s}{4\pi} \varepsilon_{1,\mu} \varepsilon_{2,\nu} \mathcal{M}^{\mu\nu} , \quad (5.10)$$

$$\mathcal{M}^{\mu\nu} = \lambda_{tth}^3 \mathcal{M}_P^{\mu\nu} + \lambda_3 \lambda_{tth}^2 \mathcal{M}_B^{\mu\nu} + \lambda_4 \lambda_{tth} \mathcal{M}_{T,1}^{\mu\nu} + \lambda_3^2 \lambda_{tth} \mathcal{M}_{T,2}^{\mu\nu} . \quad (5.11)$$

The scattering tensor $\mathcal{M}^{\mu\nu}$ can be decomposed in terms of metric tensors and

external momenta and, using momentum conservation, be expressed as

$$\mathcal{M}^{\mu\nu} = \hat{A} g^{\mu\nu} + \sum_{j,l=1,4} \hat{B}_{jl} p_j^\mu p_l^\nu . \quad (5.12)$$

By solving the Ward identities $\mathcal{M}^{\varepsilon_1 p_2} = 0$, $\mathcal{M}^{p_1 \varepsilon_2} = 0$, leading to five linear relations among the tensor coefficients, or equivalently using axial gauge conditions (e.g. $\varepsilon_1 \cdot p_2$, $\varepsilon_2 \cdot p_1$), one can achieve a manifestly gauge invariant representation of the amplitude. Introducing the abelian part of the gluon field strength tensor $\mathcal{F}_j^{\mu\nu} = \varepsilon_j^\mu p_j^\nu - p_j^\mu \varepsilon_j^\nu$ it reads

$$\mathcal{M}^{\varepsilon_1 \varepsilon_2} = A \text{tr}(\mathcal{F}_1 \mathcal{F}_2) + \sum_{j,l=3,4} B_{jl} p_2 \cdot \mathcal{F}_1 \cdot p_j p_1 \cdot \mathcal{F}_2 \cdot p_l . \quad (5.13)$$

The amplitude coefficients A , B_{jl} are equal to \hat{A} , \hat{B}_{jl} , up to trivial factors. Bose symmetry of the gluons and Higgs bosons leads to additional relations among them, e.g.

$$\begin{aligned} B_{43}(1, 2) &= B_{34}(2, 1) \\ B_{44}(3, 4) &= B_{33}(4, 3) . \end{aligned} \quad (5.14)$$

After determining all amplitude coefficients, verifying the Ward identities and Bose symmetry served as a powerful check of our calculation.

It is useful to decompose the amplitude further into helicity components. Due to parity invariance only two helicity amplitudes have to be known:

$$\begin{aligned} \mathcal{M}^{--} &= \mathcal{M}^{++} , \\ \mathcal{M}^{-+} &= \mathcal{M}^{+-} . \end{aligned} \quad (5.15)$$

Applying spinor helicity methods [42, 94], the polarisation vectors for \pm helicities are given by

$$\begin{aligned} \varepsilon_1^{+\mu} \varepsilon_2^{+\nu} &= -\frac{[21]}{\langle 12 \rangle} \frac{\text{tr}^-(1\nu 2\mu)}{2s_{12}} , \\ \varepsilon_1^{+\mu} \varepsilon_2^{-\nu} &= \frac{\langle 2^- | \mu | 1^- \rangle \langle 2^- | \nu | 1^- \rangle}{\sqrt{2} \langle 21 \rangle \sqrt{2} [12]} , \end{aligned} \quad (5.16)$$

with $\text{tr}^-(1\nu \dots) \equiv [\text{tr}(\not{p}_1 \not{\nu} \dots) - \text{tr}(\gamma_5 \not{p}_1 \not{\nu} \dots)]/2$ and the spinor inner products $\langle ij \rangle \equiv \langle p_i^- | p_j^+ \rangle$, $[ij] \equiv \langle p_i^+ | p_j^- \rangle$, where $|p_i^\pm\rangle$ is the Weyl spinor for a massless particle with momentum p_i .

This implies

$$\mathcal{M}^{++} = \frac{[21]}{\langle 12 \rangle} \left(A - \frac{\text{tr}^-(1323)}{2s_{12}} B_{33} - \frac{\text{tr}^-(1423)}{2s_{12}} B_{34} - \frac{\text{tr}^-(1324)}{2s_{12}} B_{43} - \frac{\text{tr}^-(1424)}{2s_{12}} B_{44} \right) \quad (5.17)$$

and

$$\mathcal{M}^{+-} = \frac{\langle 2^- | 3 | 1^- \rangle}{\langle 1^- | 3 | 2^- \rangle} \left(\frac{\text{tr}^-(1323)}{2s_{12}} B_{33} + \frac{\text{tr}^-(1324)}{2s_{12}} B_{34} \right) + \frac{\langle 2^- | 4 | 1^- \rangle}{\langle 1^- | 4 | 2^- \rangle} \left(\frac{\text{tr}^-(1423)}{2s_{12}} B_{43} + \frac{\text{tr}^-(1424)}{2s_{12}} B_{44} \right). \quad (5.18)$$

Contrary to the ++ case, it is not possible to factor out a global spinorial phase in the +- case without introducing denominators that in general aggravate numerical problems.

5.3.2 Evaluation of the amplitude coefficients

Our goal was the analytical reduction of all diagrams, to allow for algebraic cancellations of numerically dangerous denominators in the amplitude. These denominators are so-called Gram determinants which are induced by reduction algorithms of Lorentz tensor integrals. After generating all diagrams, using the QGRAF [95] program, we used FORM 3.1 [40] to perform the gamma matrix algebra and to project the diagrams on the helicity components and amplitude coefficients. Further, by applying the reduction algorithms for scalar and tensor integrals described in [62, 96], we expressed all amplitude coefficients as a linear combination of scalar integrals. As scalar integral basis we chose 2-, 3- and 4-point functions ($s_{ij} = (p_i + p_j)^2$):

$$\begin{aligned} I_2^{d=n}(s_{ij}, m_q^2, m_q^2), \\ I_3^{d=4}(s_{ij}, s_{kl}, s_{pr}, m_q^2, m_q^2, m_q^2), \\ I_4^{d=6}(s_{ij}, s_{kl}, s_{pr}, m_q^2, m_q^2, m_q^2, m_q^2), \end{aligned}$$

which were evaluated using LoopTools-2.2 [97]. The spurious UV pole of the 2-point integral cancels when adding all diagrams. The full amplitude is composed out of 12, 24 and 31 different 2-, 3-, and 4-point functions. The complexity of the expressions is induced by the number of independent scales, which is seven here. One may chose s_{12} , s_{23} , s_{34} , s_{45} , s_{15} , m_q^2 , m_h^2 . The coefficient of each function was exported to MAPLE to apply simplification algorithms. Schematically,

$$\mathcal{M}^{\lambda_1 \lambda_2} = \sum_k \text{simplify}[C_k^{\lambda_1 \lambda_2}] I_k \quad , \quad I_k \in \{I_2^n, I_3^4, I_4^6\}. \quad (5.19)$$

In this way, we could achieve expressions with a simple denominator structure allowing for a stable numerical evaluation. In the equal helicity case, $\lambda_1 = \lambda_2$, all Gram determinants cancel. In the opposite helicity case, $\lambda_1 = -\lambda_2$, one Gram determinant survives. The simplified expressions were then exported to Fortran code. Each of these steps was completely automatised.

5.3.3 Numerical implementation

In order to compute numerical results for hadron colliders, the differential partonic cross section has to be convoluted with parton distribution functions (PDFs) and integrated over the $2 \rightarrow 3$ -particle phase space. We employed the gluon density of the MRST2002nlo PDF set [37], as implemented in LHAPDF [98], which also provides the strong coupling constant as function of the renormalisation scale. In the MSSM case, where the heavy CP-even Higgs boson H can be resonant, we used multichannel Monte Carlo (MC) integration techniques [99, 100] with phase space mappings based on [101, 102] and the adaptive MC integration package BASES [103].

The relevant quartic Higgs couplings were implemented in the program HDECAY [25], which incorporates the routine FeynHiggsFast [104], in order to evaluate the radiatively corrected Yukawa- and Higgs couplings and also the Higgs widths, as discussed above.

5.4 Results

In this section we present and discuss the LHC cross sections for 2- and 3-Higgs boson production. We use the following parameters throughout:

$$\begin{aligned}\alpha_s(M_Z) &= 0.120 \\ \alpha(0) &= 1/137.036 \\ m_t &= 178 \text{ GeV} \\ m_b &= 4.7 \text{ GeV} \\ m_W &= 80.41 \text{ GeV} \\ m_Z &= 91.1875 \text{ GeV}\end{aligned}\tag{5.20}$$

For 2-Higgs (3-Higgs) boson production, the factorisation scale μ_F and renormalisation scale μ_R were set to $\mu_F = \mu_R = 2m_H$ ($3m_H$). The strong coupling constant α_s was taken at μ_R , but for the fine structure constant we used $\alpha(0)$. All results have been calculated with a MC error of 0.5% or less.

In the following subsections we present SM cross sections for 2- and 3-Higgs boson production and describe how BSM scenarios allow for observable enhancements of the SM rates.

5.4.1 Multi-Higgs boson production in the SM

We begin with the gluon-fusion production cross section for 2 and 3 Higgs bosons. Note that in both cases large next-to-leading order corrections are expected, leading to K -factors as large as 2 like in the case of single Higgs boson production [105, 106], since the infrared structure of these processes is identical (with a large contribution from soft gluon effects).

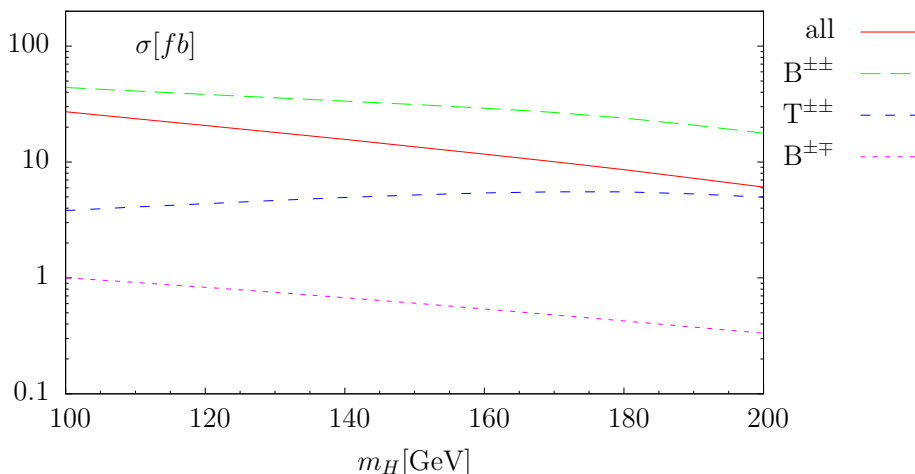


Figure 5.2: Total Higgs pair production cross section vs. m_H at the LHC, as well as the individual cross sections for box (B) and triangle (T) topologies with equal ($++ / --$) and opposite ($+ - / - +$) helicity components.

In Fig. 5.2, we display the Higgs pair production cross section vs. m_H at $\sqrt{s} = 14$ TeV. Our results show good agreement with [79] when PDF, scale and parameter uncertainties are taken into account. The total cross section falls from about 30 to 6 fb in the Higgs mass range from 100 to 200 GeV. In addition to the total cross section, the equal $++ / --$ and opposite $+ - / - +$ helicity components of the cross section are also shown. The triangle topologies only allow for a $L = S = 0$ interaction, i.e. the $+ - / - +$ helicity component is zero. Overall, the opposite helicity component is more than an order of magnitude suppressed. Furthermore, a destructive interference effect is visible between the box and triangle topologies.

In Fig. 5.3, the total cross section for triple Higgs boson production at the LHC is plotted vs. m_H . Our results agree with the recent calculation of [82] within MC errors. Again one finds that the opposite helicity components of the cross section are more than an order of magnitude suppressed. In the figure, the pentagon, box, and triangle contributions are also shown separately. The latter, being proportional to λ_3^2 and λ_4 , are suppressed relative to the box and pentagon topologies. Due to interference effects the contribution of the quartic Higgs self-coupling to the total cross section

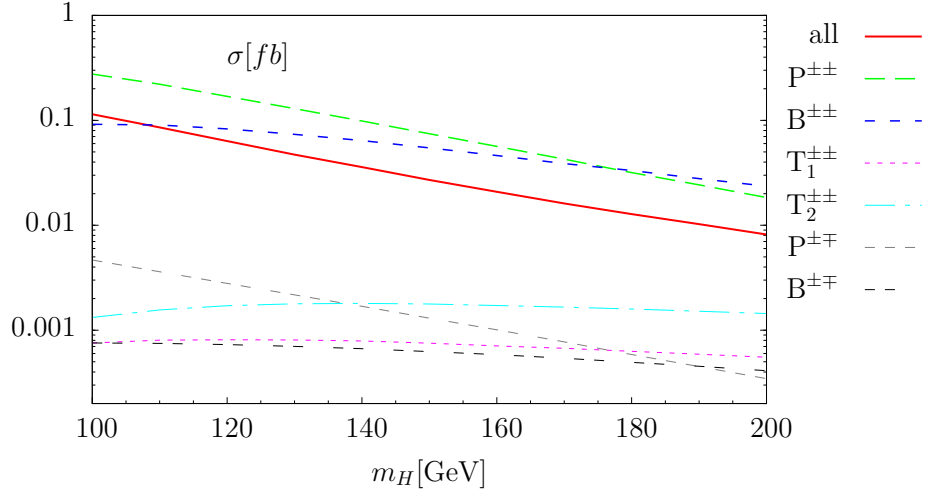


Figure 5.3: The total 3-Higgs boson production cross section vs. m_H at the LHC. Equal and opposite helicity components of contributions from various topologies are shown.

		m_H [GeV]	120	150	180
LHC	σ [fb]		0.0623	0.0267	0.0126
VLHC	σ [fb]		9.55	4.89	2.98

Table 5.1: Typical cross sections for triple Higgs boson production at the LHC and a 200 TeV VLHC.

is not negligible: it varies between +1% ($m_H = 100$ GeV) and -57.5% ($m_H = 200$ GeV). The destructive interference pattern between triangle, box and respectively box and pentagon contributions is well-known. It can be understood from the fact that the effective two-gluon n -Higgs boson operators contain a factor $(-1)^n$ [78]. As the self-couplings increase with increasing Higgs mass, the box and triangle topologies become more and more important relative to the pentagon contribution.

In Table 5.1 we give predictions for different values of the Higgs mass for the LHC and a 200 TeV Very Large Hadron Collider (VLHC). We also note that a change in the top mass best fit value from $m_t = 178$ GeV to 172.5 GeV leads to a 15% decrease of the cross section.

In Table 5.2, we compare the relative importance of the different topologies and helicities at the VLHC.

Furthermore, the gluon fusion cross section is proportional to α_s^2 and thus very sensitive to renormalisation scale variations, as exemplified in Fig. 5.4 for $\mu = \mu_R = \mu_F$. Here, the scale μ is varied around the central choice $\mu_0 = 2 m_H$ and $\mu_0 = 3 m_H$ for 2- and 3-Higgs boson production, respectively, by a factor $\mu/\mu_0 \in [1/3, 3]$. From this

σ [fb]	all	$P^{\pm\pm}$	$B^{\pm\pm}$	$T_1^{\pm\pm}$	$T_2^{\pm\pm}$	$P^{\pm\mp}$	$B^{\pm\mp}$
$m_H = 120$ GeV	9.55	21.82	10.04	0.111	0.189	0.589	0.169
$m_H = 200$ GeV	1.93	3.97	4.76	0.129	0.262	0.125	0.163

Table 5.2: Contributions of different topologies to triple Higgs boson production at a 200 TeV VLHC.

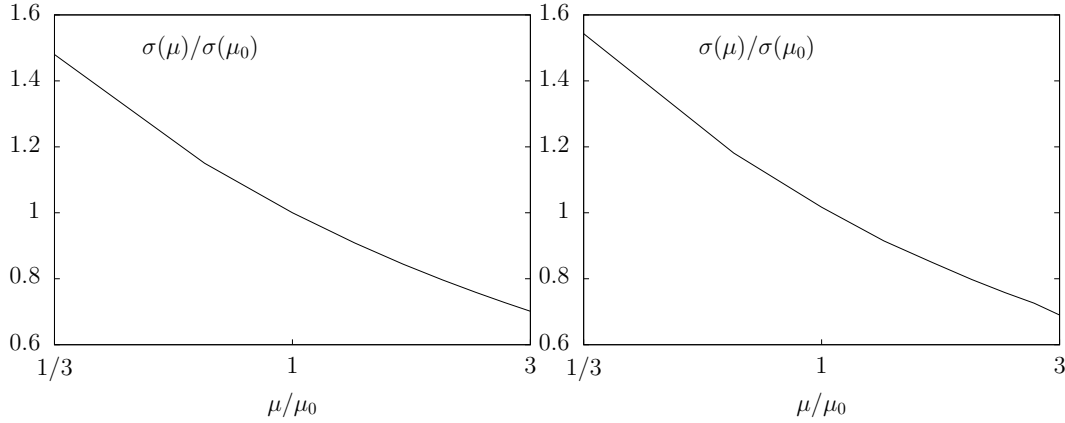


Figure 5.4: Renormalisation and factorisation scale dependence ($\mu = \mu_R = \mu_F$) of the 2-Higgs (left, $\mu_0 = 2m_H$) and 3-Higgs (right, $\mu_0 = 3m_H$) cross sections at the LHC.

we estimate a scale uncertainty of about 50%. Thus, large K -factors due to higher order effects can be expected. In Table 5.3 we study the scale dependence of the cross section for 3-Higgs boson production by varying the renormalisation and factorisation scales independently for $m_H = 120$ GeV. Note that the gluon luminosity decreases with increasing scale μ_F , because in 3-Higgs boson production the momentum of the gluons has to be relatively high. Hence, the cross section shrinks with increasing μ_F and μ_R . The table demonstrates that varying μ_R and μ_F in the same direction yields a conservative estimate of the scale uncertainty.

$\sigma[10^{-2}\text{fb}]$	$\mu_F = m_H$	$3m_H$	$9m_H$
$\mu_R = m_H$	9.71	8.61	7.66
$3m_H$	7.21	6.38	5.68
$9m_H$	5.57	4.93	4.39

Table 5.3: Renormalisation and factorisation scale dependence of the $gg \rightarrow HHH$ cross section for $m_H = 120$ GeV at the LHC.

5.4.2 Quality of the heavy-top approximation

Many years ago multi-Higgs boson production via gluon fusion was studied in [108] in the heavy top limit. In the limit $m_t \gg m_H$, the fermion loop effectively becomes a point interaction, and $gg \rightarrow nH$ couplings can be derived from the effective Lagrangian

$$\mathcal{L}_{\text{eff}} = \frac{\alpha_s}{12\pi} F^{a,\mu\nu} F_{\mu\nu}^a \log \left(1 + \frac{H}{v} \right), \quad (5.21)$$

where $F^{a,\mu\nu}$ is the field strength tensor of the gluon. Expanding the logarithm leads to the Feynman rules for the Higgs self-couplings

$$ggH : i \frac{\alpha_s}{3\pi} \delta^{ab} (k_1 \cdot k_2 g^{\mu\nu} - k_1^\mu k_2^\nu) \cdot \frac{1}{v}, \quad (5.22a)$$

$$ggHH : i \frac{\alpha_s}{3\pi} \delta^{ab} (k_1 \cdot k_2 g^{\mu\nu} - k_1^\mu k_2^\nu) \cdot \frac{-1}{v^2}, \quad (5.22b)$$

$$ggHHH : i \frac{\alpha_s}{3\pi} \delta^{ab} (k_1 \cdot k_2 g^{\mu\nu} - k_1^\mu k_2^\nu) \cdot \frac{2}{v^3}, \quad (5.22c)$$

where k_1 and k_2 are the gluon momenta. The calculation of matrix elements is therefore reduced to a much simpler tree-level calculation.

For single Higgs boson production via gluon fusion this limit is well known to be a good approximation [107]. In the context of multi-Higgs boson production, the heavy top limit has been applied at the leading [108] and next-to-leading level [109]. In [72], the quality of the heavy top approximation has been studied for Higgs pair production, and agreement at the $\mathcal{O}(10\%)$ -level for the total cross section, but large discrepancies for kinematic distributions have been observed when comparing results for $m_t \rightarrow \infty$ and physical m_t . In Fig. 5.5 we compare our physical- m_t results with results in the heavy top limit. While there is reasonable agreement in the 2-Higgs case for small Higgs masses, the heavy top limit fails completely in the 3-Higgs case. To better understand this observation, we study the variation of the cross sections with the internal quark mass m_q for a fixed value of $m_H = 120$ GeV in Fig. 5.6. We see that in the 2-Higgs case the heavy top limit accidentally agrees with the result for $m_q = m_t$ (indicated by the vertical line). However, asymptotically the result for finite m_q approaches the $m_q \rightarrow \infty$ limit only for masses around 3 TeV. The same holds for the 3-Higgs case, but here the result for $m_q = m_t$ is an order of magnitude smaller than the heavy top limit. In both cases the dominant contribution to the cross section comes from the kinematic regime close to the top pair threshold $s_{ij} \sim 4m_t^2$. We conclude that the heavy top limit is not applicable when calculating multi-Higgs boson production cross sections and should not be used in experimental studies.

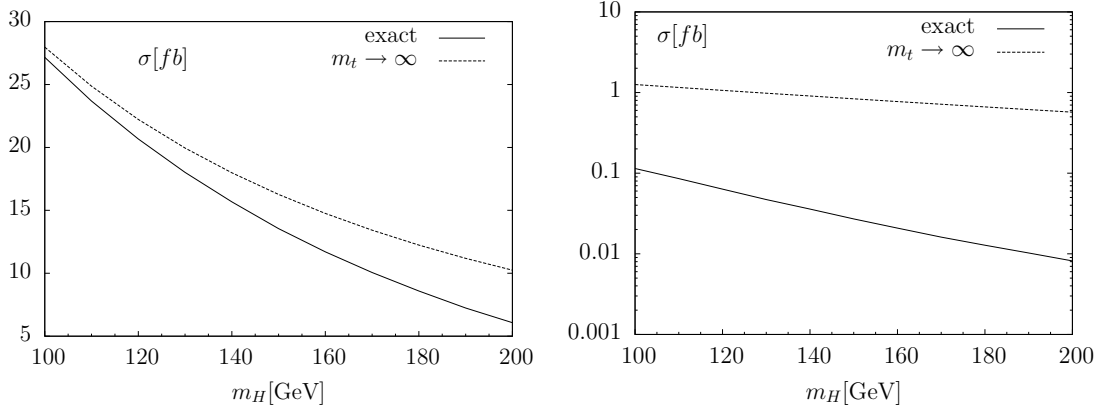


Figure 5.5: Comparison of the total cross section for 2-Higgs (left) and 3-Higgs (right) boson production vs. m_H at the LHC, calculated for the physical value of m_t and in the $m_t \rightarrow \infty$ limit.

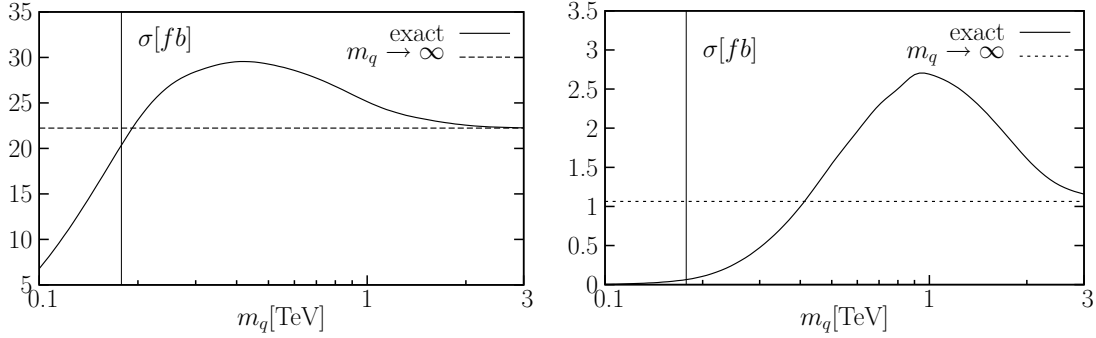


Figure 5.6: The total cross section for 2-Higgs (left) and 3-Higgs (right) production vs. m_q . The $m_q \rightarrow \infty$ limit is shown as horizontal line. The vertical line indicates the actual value of the top quark mass.

5.4.3 Multi-Higgs boson production beyond the SM

If one allows for higher dimensional operators in the Higgs sector the trilinear and quartic Higgs self-couplings are no longer directly related to the Higgs mass. This has motivated us to study the variation of the cross section with respect to λ_3 , λ_4 and m_H . In Fig. 5.7 we illustrate the variation of the cross section for 3-Higgs boson production with λ_3 and λ_4 (m_H is fixed), and in Fig. 5.8 the variation with λ_3 and m_H (λ_4 is fixed). Fig. 5.9 shows the variation with λ_3 and m_H for the 2-Higgs boson production.

The variation of the cross section with λ_3 , λ_4 and m_H is mainly due to phase space and interference effects. When m_H increases, the phase space is reduced and the PDF and α_s are to be taken at a higher value of x and a larger scale. All effects conspire and lead to a smaller cross section. The dependence on λ_3 is mainly due to the interference pattern. In Fig. 5.10 a slice of the contour plot Fig. 5.8 is shown for $m_H = 160$ GeV.

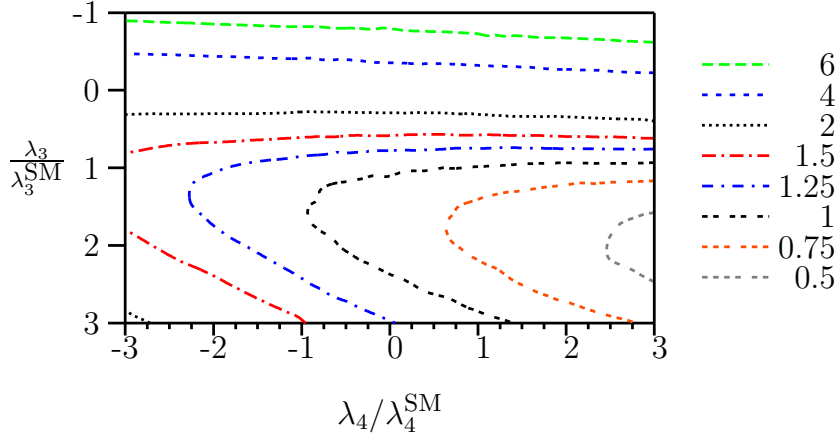


Figure 5.7: Contour plot showing the variation of the cross section for 3-Higgs boson production with λ_3 and λ_4 for $m_H = 120 \text{ GeV}$ at the LHC. The numbers denote the cross section normalised to $\sigma_{\text{SM}}(m_H = 120 \text{ GeV}) = 0.0623 \text{ fb}$.

When the trilinear coupling λ_3 becomes negative, the destructive interference between box and pentagon topologies turns into a constructive one, which explains the rise of the cross section in this regime. Increasing the coupling to positive values beyond the SM value first enhances the destructive interference effect, but finally the box topologies win and the full cross section grows again. The minimum moves to lower values of λ_3 when the Higgs mass gets larger, due to the growth of the Higgs self-couplings. We note that the same effect happens in the 2-Higgs case. It implies that even a precise measurement of the cross section by itself would not lead to a unique determination of the trilinear coupling.

This reasoning allows now to understand the variation of the cross section with λ_4 in Fig. 5.7. For negative values of λ_3 the box and pentagon topologies interfere constructively and the relative importance of the triangle contribution proportional to λ_4, λ_3^2 is further reduced, resulting in an almost flat dependence on λ_4 . For positive λ_3 the contribution of the triangle topologies is pronounced by destructive interferences between the various topologies leading to a slight variation with λ_4 . As can be seen from Fig. 5.7, for $\lambda_3/\lambda_3^{\text{SM}}$ in the range 0.5 to 1.5 and $\lambda_4/\lambda_4^{\text{SM}}$ in the range -3 to 3 the cross section varies from 0.03 to 0.1 fb.

In principle the couplings are restricted only by unitarity bounds. To illustrate the effects of large couplings that approach the nonperturbative regime, we list in Table 5.4 cross sections for values $|\lambda_3/v|, |\lambda_4| \sim 4\pi$. We see that nonperturbative effects in the Higgs sector may well lead to sizable triple Higgs cross sections of up to 30 fb at the LHC.

As already pointed out in section 5.2, in 2HDMs one finds two amplification effects for multi-Higgs boson production. These are illustrated in Fig. 5.11 (3-Higgs production) and in Fig. 5.12 (2-Higgs production) for the MSSM. The amplification

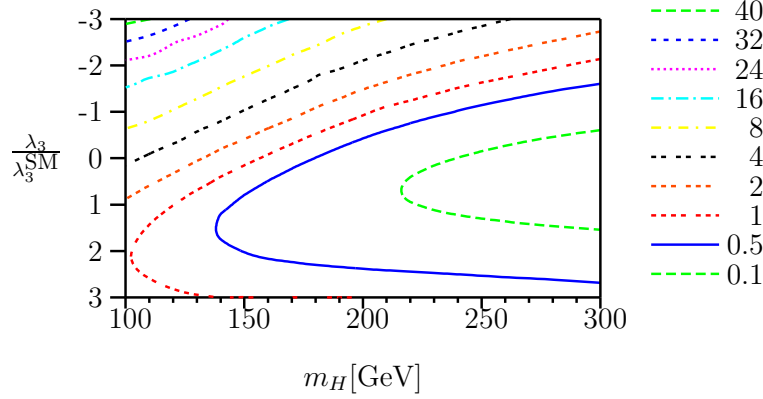


Figure 5.8: Contour plot showing the variation of the cross section for 3-Higgs boson production with λ_3 and m_H for $\lambda_4 = \lambda_4^{SM}$ at the LHC, normalised to $\sigma_{SM}(m_H = 120 \text{ GeV}) = 0.0623 \text{ fb}$.

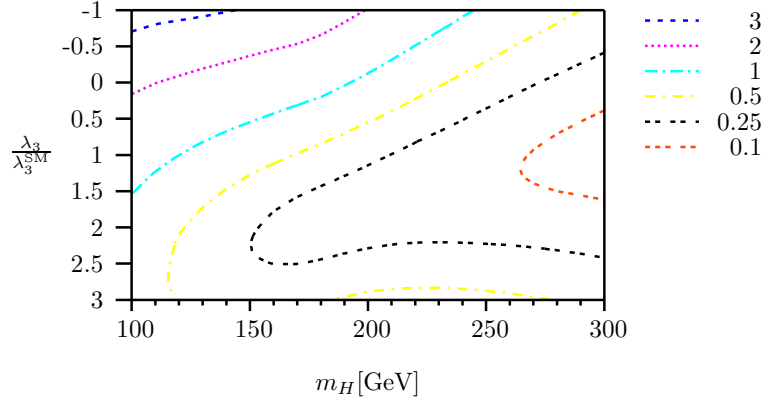


Figure 5.9: Contour plot showing the variation of the cross section for 2-Higgs boson production with λ_3 and m_H at the LHC, normalised to $\sigma_{SM}(m_H = 120 \text{ GeV}) = 20.7 \text{ fb}$.

effects for 2-Higgs production have already been observed in [71]. Fig. 5.12 shows a comparison with the calculation in this thesis. They are in good agreement up to unknown input parameters like m_t , α_s and pdf choices. The authors of [71] also included a K-factor of 1.9. Since the qualitative behaviour for the 2-Higgs production is the same as for 3-Higgs production, this case is not separately discussed. For small $\tan\beta = 3$ the heavy CP even Higgs boson may become resonant in some of the topologies sketched in Fig. 5.1. This is illustrated in Figs. 5.11a, 5.12a. With the given choice of parameters one sees for the 3-Higgs production that for $m_h > 109 \text{ GeV}$ the $H \rightarrow hh$ channel opens up inducing a resonant amplification of the box and triangle topologies, B and T_2 . For $m_h > 111 \text{ GeV}$ also the $H \rightarrow hhh$ channel opens up leading to an enhancement of the triangle topology T_1 proportional to the quartic coupling λ_{Hhh} . Since this triangle contribution is suppressed relative to the other

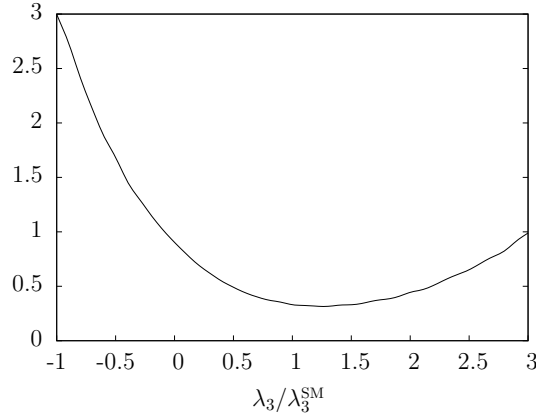


Figure 5.10: Variation of the cross section for 3-Higgs boson production with λ_3 for $m_H = 160$ GeV and fixed $\lambda_4 = \lambda_4^{\text{SM}}$ at the LHC, normalised to $\sigma_{\text{SM}}(m_H = 120 \text{ GeV}) = 0.0623 \text{ fb}$.

$\sigma[\text{fb}]$	$\lambda_4 = -4\pi$	0	4π
$\lambda_3/v = -4\pi$	28.0	30.7	33.4
0	0.169	0.0271	0.0428
4π	12.2	14.0	15.8

Table 5.4: 3-Higgs boson production cross sections for extreme choices of the Higgs couplings for $m_H = 150$ GeV at the LHC.

topologies the effect is hardly visible in the plot (tiny peak next to the right vertical line). We see that in BSM scenarios resonant amplification may lead to triple Higgs production reaching a few fb (not taking into account the expected K -factor of 2), which would be observable at the SuperLHC or even at the LHC.

For large $\tan\beta = 50$ the top contribution is largely suppressed and the bottom loops become dominant due to the enhanced Yukawa couplings. Resonance effects on the other hand are now negligible, because the Higgs width Γ_H is a factor 50 larger than at small $\tan\beta = 3$. Based on the double Higgs production results in [77], we expect therefore that the LO triple Higgs production cross section in bottom quark fusion is smaller than in gluon fusion. As the pentagon contribution to the cross section is proportional to $\lambda_{hb\bar{b}}^6$, all other topologies are much less relevant. For $m_A \rightarrow \infty$, m_h approaches its maximal value. In this limit one obtains the SM value for the cross section as shown in Fig. 5.11b. The minimum around $m_h \sim 115$ GeV arises due to the interplay of the Yukawa- and Higgs self-coupling, see Figs. 5.13c,d. Although the cross section rises for decreasing m_h , it is always well below 1 fb in the range considered. Note that in the 2-Higgs boson production case the bottom loops are more pronounced than in the 3-Higgs case, because the scalar loop integrals are probed in different kinematical regions.

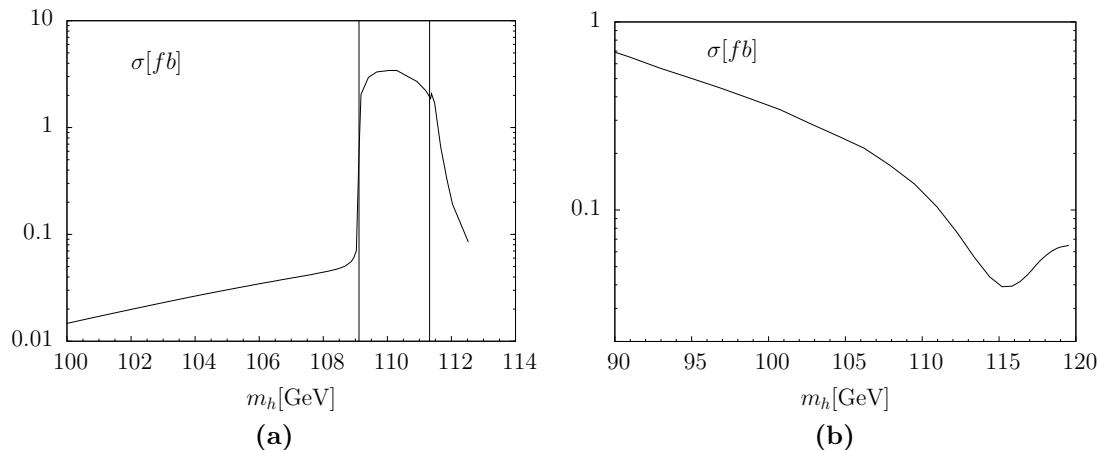


Figure 5.11: Cross section for 3-Higgs boson production vs. m_h at the LHC in the MSSM for $\tan\beta = 3$ (left) and $\tan\beta = 50$ (right) including mixing effects ($A_t = 1\text{TeV}$, $\mu/\text{TeV} = -1 (+1)$ for $\tan\beta = 3 (50)$). The vertical lines in the left plot indicate the 2- and 3-Higgs boson thresholds ($H \rightarrow hh$ and $H \rightarrow hhh$).

In principle, also squark loops have to be considered to obtain a complete prediction for hhh -production in the MSSM. In the heavy squark limit this contribution decouples and approaches zero in contrast to the quark contribution. For the present illustration of amplification effects we have neglected squark effects.

5.5 Summary

We presented our calculation of the loop-induced processes $gg \rightarrow HH$ and $gg \rightarrow HHH$, and discussed the resulting cross sections and their experimental accessibility at the LHC in the SM and beyond. The contributions from pentagon, box and triangle topologies exhibit strong interference patterns and large differences in the equal and opposite gluon helicity components. Generally, the opposite helicity component, which corresponds to a gluon pair with helicity 2, is suppressed by more than an order of magnitude. Furthermore, the triangle topologies are suppressed relative to the box and pentagon topologies. This results in a complex dependence of the cross sections on the trilinear and quartic Higgs self-couplings. The cross section for 3-Higgs boson production varies strongly with the quartic Higgs self-coupling. For $m_H = 100$ GeV and 200 GeV it affects the cross section by +1% and -57.5%, respectively. This effect is due to the fact that the Higgs self-coupling contributions are enhanced for higher Higgs masses and that there is a strong destructive interference between box and pentagon contributions. The estimated renormalisation and factorisation scale uncertainty of about 50% (variation by a factor 3) is typical for leading-order QCD cross sections. We also investigated the applicability of the heavy top quark approximation for 2- and 3-Higgs boson production and demonstrated that the heavy top

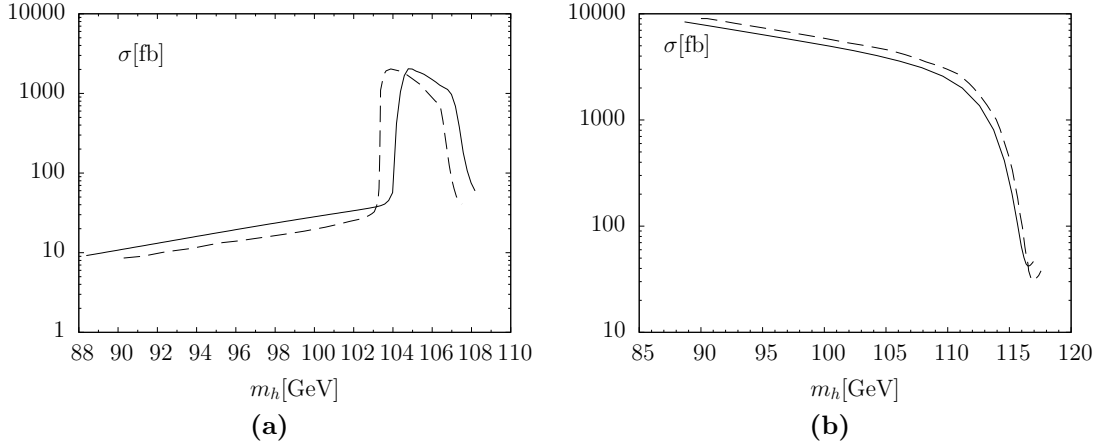


Figure 5.12: Cross section for 2-Higgs boson production vs. m_h at the LHC in the MSSM for $\tan\beta = 3$ (left) and $\tan\beta = 50$ (right) including mixing effects ($A_t = 1\text{TeV}$, $\mu/\text{TeV} = -1$ (+1) for $\tan\beta = 3$ (50)) and a K-factor of 1.9. A top-quark mass of $m_t = 175$ GeV and $\mu_F = \mu_R = M_H$ have been used. A comparison is shown with the results of [71] (dashed curve).

limit is not applicable when calculating multi-Higgs boson production cross sections. In summary, we find that the SM cross sections for 3-Higgs boson production are too small for observation at the LHC. The measurement of the SM trilinear Higgs self-coupling in 2-Higgs boson production, on the other hand, may be feasible at a luminosity-upgraded LHC, termed SuperLHC, collecting 6000 fb^{-1} of data, as long as QCD backgrounds are not prohibitively large [64, 110].

The experimental prospects improve if favourable extensions of the SM are realised in nature. We have demonstrated that cross sections for triple Higgs boson production can be as large as $\mathcal{O}(10)$ fb if one allows for higher dimensional operators or considers 2-Higgs-doublet models, e.g. the MSSM. Here, two amplification effects have been analysed. First, we studied Yukawa coupling enhancements through mixing that lead to important bottom-loop contributions. For the 3-Higgs case the cross section remains below 1 fb for the parameters considered and $\tan\beta = 50$. Secondly, we demonstrated that resonance effects due to an internal heavy Higgs boson decaying into 2 or 3 light Higgs bosons can enhance the 3-Higgs cross section into the potentially observable $\mathcal{O}(\text{fb})$ region. Higher dimensional operators lead to essentially unconstrained trilinear and quartic couplings. Strong coupling of the order $|\lambda_3/v|, |\lambda_4| \sim 4\pi$ leads to cross sections of up to 30 fb. This implies that already the LHC should be able to restrict the λ_3 - λ_4 plane. Although these bounds will not be very restrictive, they may still exclude parameter regions that exhibit nonperturbative effects, which would be an important qualitative finding. A more stringent bound on λ_3 alone will be obtained from Higgs pair production. We conclude that multi-Higgs boson production at the luminosity-upgraded LHC is an interesting probe of Higgs sectors beyond the

SM and warrants further study. A 200 TeV VLHC would of course further improve the sensitivity.

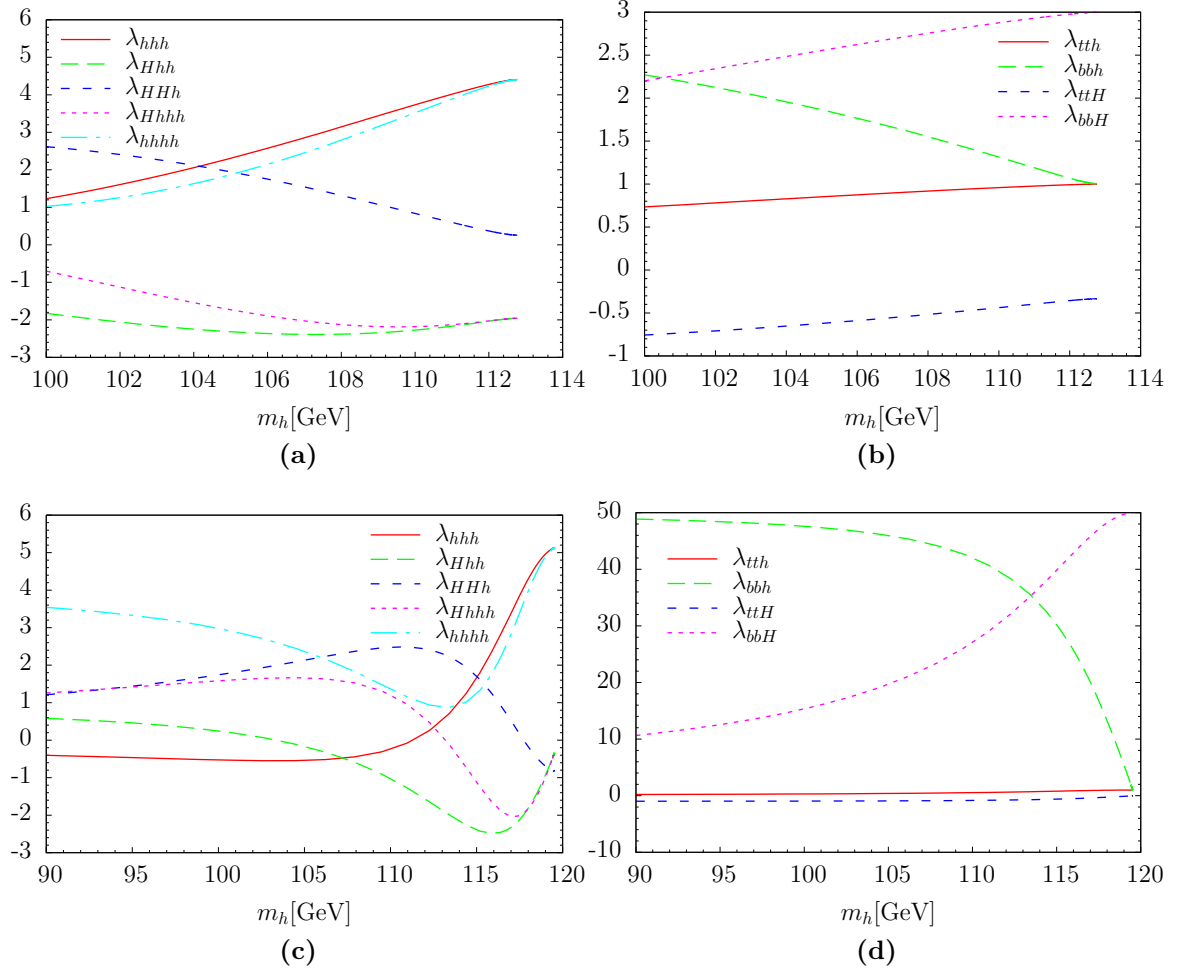


Figure 5.13: Normalised Higgs- and Yukawa-couplings of the CP-even MSSM neutral Higgs bosons as a function of m_h for $\tan\beta = 3$ (top) and $\tan\beta = 50$ (bottom) including the same mixing effects as in Fig. 5.11.

NLO QCD Cross section for $PP \rightarrow VV + \text{jet}$

6

6.1 Introduction

The search and interpretation of new physics at the LHC requires a precise understanding of the Standard Model. The quality of phenomenological analyses strongly depends on accurate QCD predictions and reliable error estimates. At the LHC, most analyses require perturbative calculations to at least NLO. Theoretical predictions for QCD processes at LO are usually affected by a large renormalisation and factorisation scale dependence. This uncertainty is significantly reduced, if NLO corrections are taken into account and getting comparable to the experimental systematic uncertainty. The scale uncertainty of background processes can be very sensitive on experimental cuts, which are employed in order to increase the signal-to-background ratio, and therefore higher order calculations are mandatory for reliable phenomenological analyses. Furthermore, additional partonic channels can contribute for a given scattering process at NLO, which are absent at LO. This can have a significant impact on differential distributions, which are used in phenomenological analyses. The need for higher order calculations at the LHC is summarised in an experimental “NLO wish-list” of processes for which QCD corrections are desired, see Table 1.1 in chapter 1, which has been recently updated at the Les Houches workshop in summer 2007.

A NLO calculation contains two primary components: virtual corrections, where internal lines are added to the LO Feynman diagrams, and real corrections, where an additional parton is radiated. Each contribution is separately divergent. Only the combination of the two components leads to a finite result. Singularities originating from collinear initial states do not cancel in the amplitude, they have to be absorbed into the definitions of the parton distribution functions. Well-developed techniques exist for the computation of the real emission matrix elements (recurrence relations, Feynman diagrammatic approaches) and the extraction of the singularities which occur when integrating over the phase space of the additional unresolved parton (e.g. dipole subtraction formalism, phase space slicing). Standard reduction algorithms such as the Passarino-Veltman method can be applied to one-loop virtual amplitudes

which involve maximally four particles. Therefore, many NLO predictions are available for $2 \rightarrow 2$ scattering processes.

At the LHC, however, many interesting signatures lead to multi-particle ($2 \rightarrow 3, 4$) final states and the computation of the virtual corrections is the bottleneck for obtaining NLO predictions for the processes in Table 1.1, which are considered most important for LHC phenomenology. The difficulties one has to face in the evaluation of multi-particle process at NLO has already been explained in chapter 4.

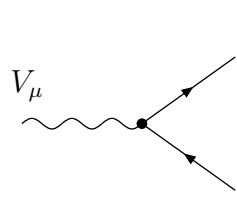
In this chapter, we investigate the first process in Table 1.1, the production of a pair of electroweak vector bosons in association with a hard jet and show first results for the computation of the virtual corrections.

The decay of the Higgs boson to EW vector bosons is one of the promising channels for Higgs production in the low mass range. Therefore, background processes involving a pair of EW vector bosons have to be known with high precision. The case where the Higgs boson is produced in association with a jet is also relevant, since a significant fraction of produced Higgs bosons are associated with at least one high transverse momentum hadronic jet. The additional jet activity leads to a more distinctive kinematics which could significantly improve the Higgs boson search strategies, as has been pointed out in a recent study, using LO matrix elements [111].

The calculation of $PP \rightarrow VV + \text{jet}$ at NLO will be especially important in understanding the background to this signal process. Its contribution typically reaches 10 to 30% [112] of the VV production cross section and therefore is an important source of gauge bosons pairs at the LHC. The existence of a high p_T jet in the final state allows us to choose suitable cuts which can suppress the large QCD background. The calculation of the virtual QCD corrections to $q\bar{q} \rightarrow VVg$ is also an important component for a complete NNLO QCD calculation for the production of a pair of EW vector bosons, which consists of three components: the real emissions with up to two unresolved partons at tree-level, the one-loop diagrams with one unresolved parton leading to both virtual and real contributions, and the computation of the two-loop virtual contribution. The latter is currently also in progress [113].

6.2 Amplitude organisation

The computation of the hadronic $VV + \text{jet}$ production cross section receives contributions from the partonic processes $q\bar{q} \rightarrow VVg$, $qg \rightarrow VVq$, and $\bar{q}g \rightarrow VV\bar{q}$. These three channels are related by crossing relations to the amplitude $q\bar{q}VVg \rightarrow 0$, thus only one matrix element has to be computed. The Feynman rule for the interaction of a vector boson V_μ with a antifermion-fermion pair $\bar{F}_1 F_2$ is given by



$$= ie\gamma_\mu \left(C_R \frac{1+\gamma_5}{2} + C_L \frac{1-\gamma_5}{2} \right) \quad (6.1)$$

with the values of V , \bar{F}_1 , F_2 , C_R and C_L

$V \bar{F}_1 F_2$	$Z \bar{f}_i f_j$	$W^+ \bar{u}_i d_j$	$W^- \bar{d}_j u_i$
C_L	$g_f^- \delta_{ij}$	$\frac{1}{\sqrt{2} \sin \theta_w} V_{ij}$	$\frac{1}{\sqrt{2} \sin \theta_w} V_{ji}^\dagger$
C_R	$g_f^- \delta_{ij}$	0	0

where

$$g_f^+ = -\frac{\sin \theta_W}{\cos \theta_W} Q_f, \quad g_f^- = \frac{\tau_f^3 - \sin^2 \theta_W Q_f}{\sin \theta_W \cos \theta_W}. \quad (6.2)$$

Q_f is the electric charge of the quark f ($f = u, d, c, s, t, b$) in units of the proton charge, τ_f^3 is the third component of the weak isospin, θ_W is the weak mixing angle, and \mathbf{V} is the CKM quark mixing matrix [114], which describes the transformation from the mass eigenstates to the weak-interaction eigenstates of the quarks.

In our calculation we only consider amplitudes containing a pair of Z bosons. Extending the calculation to a pair of W bosons does not pose a calculational problem, only the couplings of the vector boson to the fermions have to be adjusted and a few box diagrams due to the ZWW -vertex have to be included. We also set all appearing quark masses to zero and therefore use $\mathbf{V} = \mathbf{1}$.

The production of a pair of vector bosons in association with a large transverse momentum jet is studied in lowest order QCD in [112, 115]. At tree level, there are six Feynman diagrams contributing to the process, shown in Fig. 6.1. The virtual

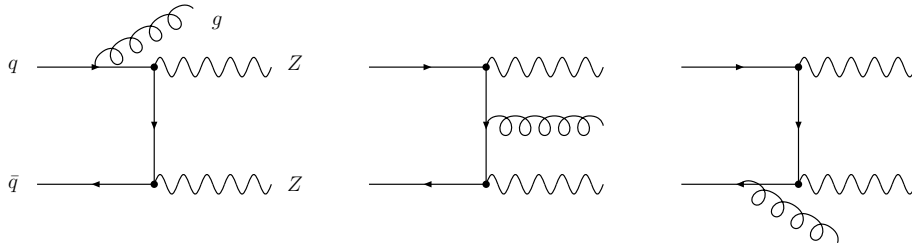


Figure 6.1: Leading order Feynman diagrams for $q\bar{q} \rightarrow ZZg$. Additional diagrams result from the exchange of the momenta of the vector bosons.

corrections modify the LO partonic processes. At NLO, these corrections are induced

by self-energy, vertex, box and pentagon corrections, one Feynman diagram for each of these corrections is shown in Fig. 6.2. The whole set of diagrams can be found in appendix B. The 't Hooft-Veltman regularisation scheme, see section 4.2, has been used, providing a consistent treatment of the Dirac matrix γ_5 in n -dimensional traces of gamma-matrices. The Feynman diagrams have been generated with QGRAF [95],

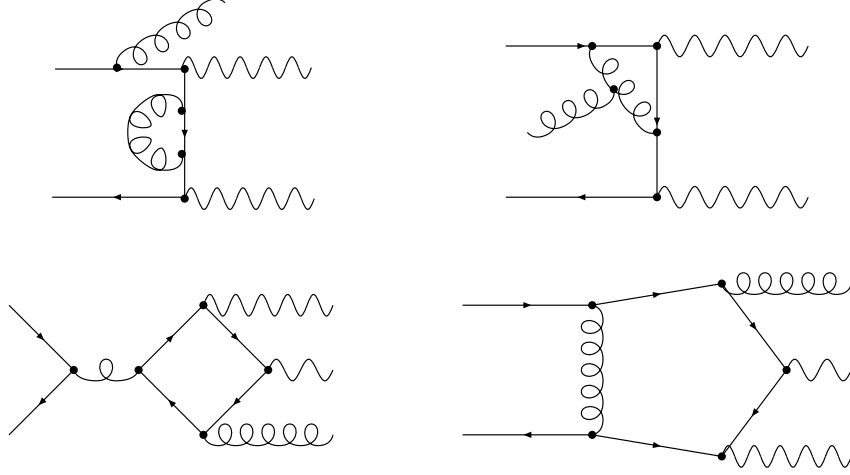


Figure 6.2: Generic Feynman diagrams contributing to the virtual corrections for $q\bar{q} \rightarrow ZZg$. One example for a self-energy, vertex, box and pentagon correction is shown. The whole set of diagrams can be found in appendix B.

and are further manipulated with Form [40] and MAPLE.

To set the notation, we consider the process

$$q(p_1, \lambda_1) + \bar{q}(p_2, \lambda_2) + V(p_3, \lambda_3) + \bar{V}(p_4, \lambda_4) + g(p_5, \lambda_5) \rightarrow 0. \quad (6.3)$$

For massless quarks the allowed helicities are $\lambda_1 = \lambda_2, \lambda_5 \in \{-, +\}, \lambda_3, \lambda_4 \in \{-, 0, +\}$ which leads in general to 36 different helicity amplitudes. For the W case, only 18 helicity amplitudes have to be evaluated, since the W boson couples only to left-handed fermions. In the spinor formalism, the amplitude can be written as $(|p_i^\lambda\rangle \equiv |i^\lambda\rangle)$

$$\mathcal{M}^{\lambda_1\lambda_2\lambda_3\lambda_4\lambda_5} = \varepsilon_{3,\mu_3}^{\lambda_3} \varepsilon_{4,\mu_4}^{\lambda_4} \varepsilon_{5,\mu_5}^{\lambda_5} \langle 2^{\lambda_2} | \Gamma^{\mu_3\mu_4\mu_5} | 1^{\lambda_1} \rangle. \quad (6.4)$$

Before turning to helicity methods we want to discuss the discrete symmetries which relate different helicity amplitudes with each other. Let us first discuss the ZZ case. Bose symmetry (\mathcal{B}) between the two Z bosons and the parity transformation (\mathcal{P}) act in the following way on the amplitude:

$$\begin{aligned} \mathcal{B}\mathcal{M}_{ZZ}^{\lambda_1\lambda_2\lambda_3\lambda_4\lambda_5}(1, 2, 3, 4, 5; g_Z^+, g_Z^-) &= \mathcal{M}_{ZZ}^{\lambda_1\lambda_2\lambda_4\lambda_3\lambda_5}(1, 2, 4, 3, 5; g_Z^+, g_Z^-) \\ \mathcal{P}\mathcal{M}_{ZZ}^{\lambda_1\lambda_2\lambda_3\lambda_4\lambda_5}(1, 2, 3, 4, 5; g_Z^+, g_Z^-) &= \mathcal{M}_{ZZ}^{-\lambda_1-\lambda_2-\lambda_3-\lambda_4-\lambda_5}(1, 2, 3, 4, 5; g_Z^-, g_Z^+) \end{aligned}$$

$$\mathcal{BPM}_{ZZ}^{\lambda_1\lambda_2\lambda_3\lambda_4\lambda_5}(1, 2, 3, 4, 5; g_Z^+, g_Z^-) = \mathcal{M}_{ZZ}^{-\lambda_1-\lambda_2-\lambda_4-\lambda_3-\lambda_5}(1, 2, 4, 3, 5; g_Z^-, g_Z^+)$$

Of course only Bose symmetry is a true symmetry of the amplitude. Parity is broken, as $g_Z^+ \neq g_Z^-$, but the parity transformation can be used to map amplitude representations onto each other. With these relations it is easy to see that only 12 helicity amplitudes are independent:

$$\begin{aligned} &\mathcal{M}_{ZZ}^{----\pm}, \mathcal{M}_{ZZ}^{--00\pm}, \mathcal{M}_{ZZ}^{--++\pm}, \\ &\mathcal{M}_{ZZ}^{--+\pm}, \mathcal{M}_{ZZ}^{--0\pm}, \mathcal{M}_{ZZ}^{--+0\pm} \end{aligned} \quad (6.5)$$

The others are obtained by applying \mathcal{B} to the second row and then \mathcal{P} to the resulting 18 amplitudes. For charged vector boson pairs the charge (\mathcal{C}) and parity transformation lead to:

$$\begin{aligned} \mathcal{CM}_{WW}^{\lambda_1\lambda_2\lambda_3\lambda_4\lambda_5}(1, 2, 3, 4, 5) &= \mathcal{M}_{WW}^{-\lambda_1-\lambda_2-\lambda_4-\lambda_3-\lambda_5}(1, 2, 4, 3, 5) \\ \mathcal{PM}_{WW}^{\lambda_1\lambda_2\lambda_3\lambda_4\lambda_5}(1, 2, 3, 4, 5) &= \mathcal{M}_{WW}^{-\lambda_1-\lambda_2-\lambda_3-\lambda_4-\lambda_5}(1, 2, 3, 4, 5) \\ \mathcal{CPM}_{WW}^{\lambda_1\lambda_2\lambda_3\lambda_4\lambda_5}(1, 2, 3, 4, 5) &= \mathcal{M}_{WW}^{\lambda_1\lambda_2\lambda_4\lambda_3\lambda_5}(1, 2, 4, 3, 5) \end{aligned} \quad (6.6)$$

Now we derive explicit expressions for the polarisation vectors for the gauge bosons. For the massive Z bosons, we introduce two light-like auxiliary vectors k_3, k_4 such that $p_3 + p_4 = k_3 + k_4$ [116]. One finds:

$$\begin{aligned} p_3 &= \frac{1}{2}[(1 + \beta)k_3 + (1 - \beta)k_4] \\ p_4 &= \frac{1}{2}[(1 + \beta)k_4 + (1 - \beta)k_3] \\ &\Leftrightarrow \\ k_3 &= \frac{1}{2\beta}[(1 + \beta)p_3 - (1 - \beta)p_4] \\ k_4 &= \frac{1}{2\beta}[(1 + \beta)p_4 - (1 - \beta)p_3] \end{aligned} \quad (6.7)$$

where $\beta = \sqrt{1 - \frac{4M_V^2}{s_{34}}}$. The polarisation vectors for the different helicities/spins of the massive vector bosons can now be written as

$$\begin{aligned} \varepsilon_{3\mu}^+ &= \frac{1}{\sqrt{2}} \frac{\langle 4^- | \mu | 3^- \rangle}{\langle 43 \rangle} \\ \varepsilon_{3\mu}^- &= \frac{1}{\sqrt{2}} \frac{\langle 3^- | \mu | 4^- \rangle}{[34]} \\ \varepsilon_{3\mu}^0 &= \frac{1}{2M_V} [(1 + \beta)k_{3\mu} - (1 - \beta)k_{4\mu}] \end{aligned}$$

$$\begin{aligned}
 \varepsilon_{4\mu}^+ &= \frac{1}{\sqrt{2}} \frac{\langle 3^- | \mu | 4^- \rangle}{\langle 34 \rangle} \\
 \varepsilon_{4\mu}^- &= \frac{1}{\sqrt{2}} \frac{\langle 4^- | \mu | 3^- \rangle}{[43]} \\
 \varepsilon_{4\mu}^0 &= \frac{1}{2M_V} [(1 + \beta)k_{4\mu} - (1 - \beta)k_{3\mu}].
 \end{aligned} \tag{6.8}$$

The two helicity states of the gluon are given as usual by

$$\begin{aligned}
 \varepsilon_{5\mu}^+ &= \frac{1}{\sqrt{2}} \frac{\langle j^- | \mu | 5^- \rangle}{\langle j5 \rangle} \\
 \varepsilon_{5\mu}^- &= \frac{1}{\sqrt{2}} \frac{\langle 5^- | \mu | j^- \rangle}{[5j]},
 \end{aligned} \tag{6.9}$$

where j is a reference vector to be chosen in a convenient way.

If $\lambda_1 = \lambda_2 = -$, a convenient choice for $\mathcal{M}^{-\lambda_3\lambda_4-}$ is $j = 2$ and for $\mathcal{M}^{-\lambda_3\lambda_4+}$ $j = 1$. In this way the spinor expression from the gluon can be attached to the spin chain. The product of the polarisation vectors of the vector bosons define projectors on the corresponding helicity states. We need

$$\begin{aligned}
 \varepsilon_3^{+\mu} \varepsilon_4^{+\nu} &= \frac{[34]}{\langle 34 \rangle} \frac{1}{4s_{34}} \text{tr}^-(3\nu 4\mu) \\
 \varepsilon_3^{-\mu} \varepsilon_4^{-\nu} &= \frac{\langle 34 \rangle}{[34]} \frac{1}{4s_{34}} \text{tr}^-(3\mu 4\nu) \\
 \varepsilon_3^{0\mu} \varepsilon_4^{0\nu} &= \frac{1}{4M_V^2} [(1 + \beta)k_3^\mu - (1 - \beta)k_4^\mu] [(1 + \beta)k_4^\nu - (1 - \beta)k_3^\nu] \\
 \varepsilon_3^{-\mu} \varepsilon_4^{+\nu} &= -\frac{\langle 35 \rangle [45]}{[35] \langle 45 \rangle} \frac{1}{32s_{34}k_3 \cdot p_5 k_4 \cdot p_5} \text{tr}^-(453\mu) \text{tr}^-(453\nu) \\
 \varepsilon_3^{-\mu} \varepsilon_4^{0\nu} &= \frac{1}{2\sqrt{8}M_V} \frac{\text{tr}^-(453\nu)}{[34] \langle 45 \rangle [53]} [(1 + \beta)k_4^\nu - (1 - \beta)k_3^\nu] \\
 \varepsilon_3^{+\mu} \varepsilon_4^{0\nu} &= \frac{1}{2\sqrt{8}M_V} \frac{\text{tr}^-(354\mu)}{\langle 35 \rangle [54] \langle 43 \rangle} [(1 + \beta)k_4^\nu - (1 - \beta)k_3^\nu]
 \end{aligned} \tag{6.10}$$

with

$$\text{tr}^-(3\nu 4\mu) = \text{tr}((1 - \gamma_5)(3\nu 4\mu)) = 4 [k_3^\mu k_4^\nu + k_3^\nu k_4^\mu - k_3 \cdot k_4 g^{\mu\nu} - \epsilon_{FORM}(3\nu 4\mu)].$$

By multiplying $\mathcal{M}^{-\lambda_3\lambda_4+}$ with $\langle 5^- | 1 | 2^- \rangle / \langle 5^- | 1 | 2^- \rangle$ and $\mathcal{M}^{-\lambda_3\lambda_4-}$ with $\langle 1^- | 2 | 5^- \rangle / \langle 1^- | 2 | 5^- \rangle$ one can close the spinor string to a trace:

$$\mathcal{M}^{-\lambda_3\lambda_4-} = -\frac{\varepsilon_3^{\lambda_3\mu_3} \varepsilon_4^{\lambda_4\mu_4}}{2\sqrt{2} \langle 12 \rangle [25]^2} \text{tr}^-(125\mu_5 2\Gamma^{\mu_3\mu_4\mu_5})$$

$$\mathcal{M}^{--\lambda_3\lambda_4+} = -\frac{\varepsilon_3^{\lambda_3\mu_3}\varepsilon_4^{\lambda_4\mu_4}}{2\sqrt{2}[12]\langle 15\rangle^2}\text{tr}^-(1\mu_5512\Gamma^{\mu_3\mu_4\mu_5}). \quad (6.11)$$

In this representation it is easy to extract a global spinorial phase for each helicity amplitude such that the remaining polynomial terms can be processed efficiently with standard computer algebra.

The colour structure of the amplitude is trivial, since it is simply proportional to the $SU(3)$ generator T^a , a being the colour index of the gluon. Three independent colour structures can be identified, being proportional to the group theoretical invariants C_F and C_A , while the third structure, proportional to N_f , the number of quark flavors, originates from box diagrams containing a fermion loop.

The scalar integral basis for the helicity amplitudes consists of 11, 25 and 26 two-, three- and four-point functions with massless internal lines. Analytical formulae can be found, for instance in [117]. Care has to be taken with these formulae, since the analytic continuation of certain dilogarithms is not trivial [60]. We evaluate the most complicated scalar box function in appendix A.

6.3 Checks of the calculation

We have applied several checks to our calculation. All Bose and Parity relations have been verified for the LO matrix elements. We numerically compared both LO cross sections and squared amplitudes (summed over all helicities) with Madgraph [118] and found complete agreement. The Ward identity of the amplitude, $\mathcal{M}^{\epsilon_3\epsilon_4p_5} = 0$, obtained by replacing the momentum of the gluon, p_5^μ , with its polarisation vector, ϵ_5^μ , has been verified. Finally, we compared Born and loop amplitudes with a second, completely independent implementation of a collaborating group. Agreement has been found for all helicity amplitudes with at least eight digits.

6.4 Results from the virtual contribution

In this section, we show numerical results for the virtual corrections for the scattering process $q\bar{q} \rightarrow ZZg$, which is the bottleneck for analysis of this process at NLO. The real corrections, which ensure the cancellation of the soft and collinear singularities, but also contribute to the finite part, are not yet implemented. In order to obtain a finite answer when integrating over the phase space, all coefficients of divergent basis integrals (two-point and singular three-point functions) have been set to zero. The fermionic contributions $\propto N_f$ are numerically small and are not included in the results shown below. The CTEQ6M parton distribution functions from the Les Houches Accord (LHAPDF) [98] for the initial quarks ($q = u, d, c, s, b$) have been used. The strong coupling α_s has been evaluated at the Z boson mass scale, via the LHAPDF routines. As electroweak input the Fermi coupling constant $G_F = 1.16639 \cdot$

10^{-5} GeV^{-2} , the W mass $m_W = 80.419 \text{ GeV}$ and the Z boson mass $m_Z = 91.188 \text{ GeV}$ have been used. From this, the electroweak mixing angle $\sin^2 \theta_W = 0.222$ and the fine structure constant $\alpha = 1/132.507$ are derived.

6.4.1 Total cross sections

Table 6.1 shows numerical results for the LO cross sections and additionally included virtual corrections for the helicity configuration $---$. Three different cuts on the scattering amplitude have been applied. Cut 1 requires the transverse momentum of the gluon to be larger than 20 GeV which is necessary for the observation of the jet in the detector. It turned out that this cut was not sufficient for obtaining a numerical stable result when evaluating the virtual amplitudes. Therefore, we additionally restricted the angles of the 3-momenta of the final particles to the beam axis and among each other. We required the angles to be larger than 1.5° (4.5°) in the lab frame for cut 2(3). We also required the volume calculated in the lab frame via $(p_i \times p_j) \cdot p_k / (|p_i||p_j||p_k|)$ of the 3-vectors to be larger than 0.0003 (0.0009) for cut 2(3). These two technical cuts provided a numerically stable total and differential cross section. The technical cuts 2 and 3 reduce the LO cross section by 13 (41)%.

	$\sigma_{LO}[fb]$	$\sigma_{LO+virt}[fb]$	$\sigma_{LO+virt}/\sigma_{LO}$
cut1	329		
cut2	287	475	1.65
cut3	194	319	1.64

Table 6.1: Total cross sections for $q\bar{q} \rightarrow ZZg$ for the helicity configuration $---$ with technical cuts

The calculated virtual contributions are sizable and increase the LO cross section by 65%, fairly independently of the two technical cuts. A further improvement of the analytical representation of the helicity amplitudes will potentially allow us to reduce or eventually discard the technical cuts completely. A direct cut of numerically unstable points in the Lorentz-invariant amplitude would also strongly reduce the effect of the technical cut.

6.4.2 Distributions

Figs. 6.3 to 6.14 show several differential cross sections of parameters which are often used in phenomenological studies of hadronic processes (see section 3.2 for the definitions). The red/solid curve always shows the LO contribution, the green/dashed curve includes the virtual corrections. The statistical error bars from the Monte-Carlo integration are also shown. The insets show the ratio of these two curves. Results are shown for cut 2 (see sec. 6.4.1). The distributions for cut 3 are not shown, but the

shape and the ratio do not change significantly. The results indicate that the NLO QCD corrections are sizable, for a decisive statement the contributions of the real emissions to the distributions have to be included.

A precise prediction at NLO for such distributions allows to reliably devise experimental cuts which help to distinguish the signal process $PP \rightarrow H+\text{jet}$ from the background. This potentially enhances the signal-to-background ratio and leads to a more precise extraction of model parameters from data. The signal process for instance would be visible as a peak in the invariant mass distribution $d\sigma/dM_{ZZj}$, its width depending on the decay width of the Higgs boson which increases with its mass.

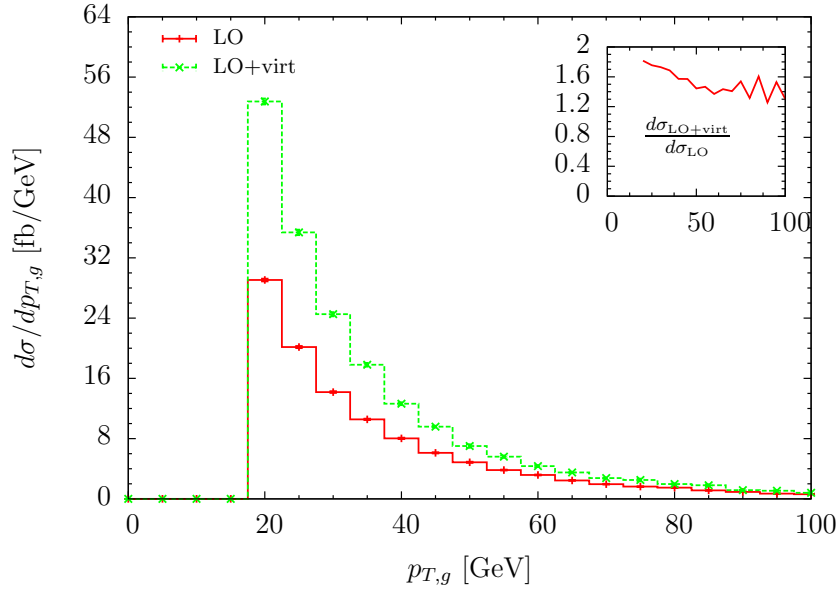


Figure 6.3: The gluon transverse momentum distribution for $q\bar{q} \rightarrow ZZg$ at the LHC for the helicity configuration $--+++$. Technical cuts have been applied. The red/solid line shows the LO contribution, the green/dashed line additionally includes virtual corrections. See the main text for more detailed information. The inset shows the ratio of the LO+virtual to the LO distribution.

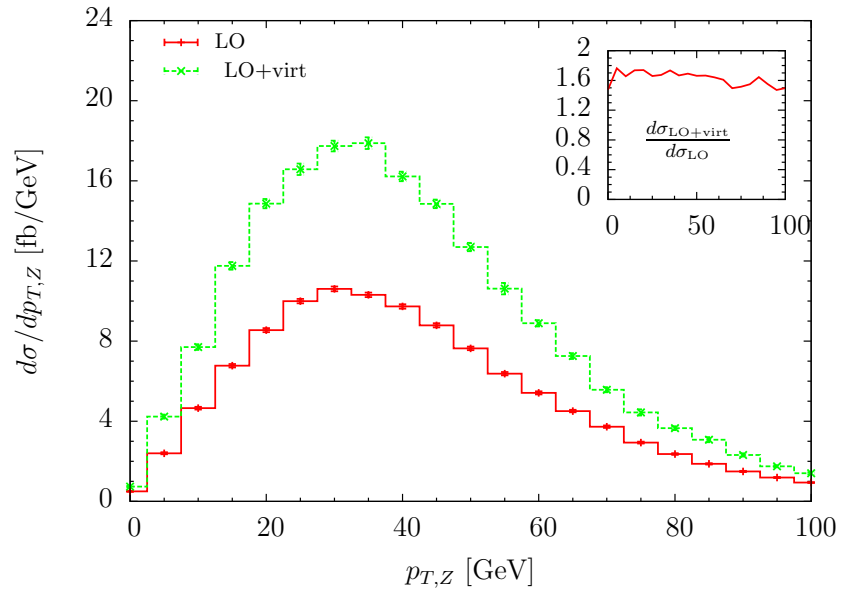


Figure 6.4: Transverse momentum distribution for a Z boson. Details as in Fig. 6.3.

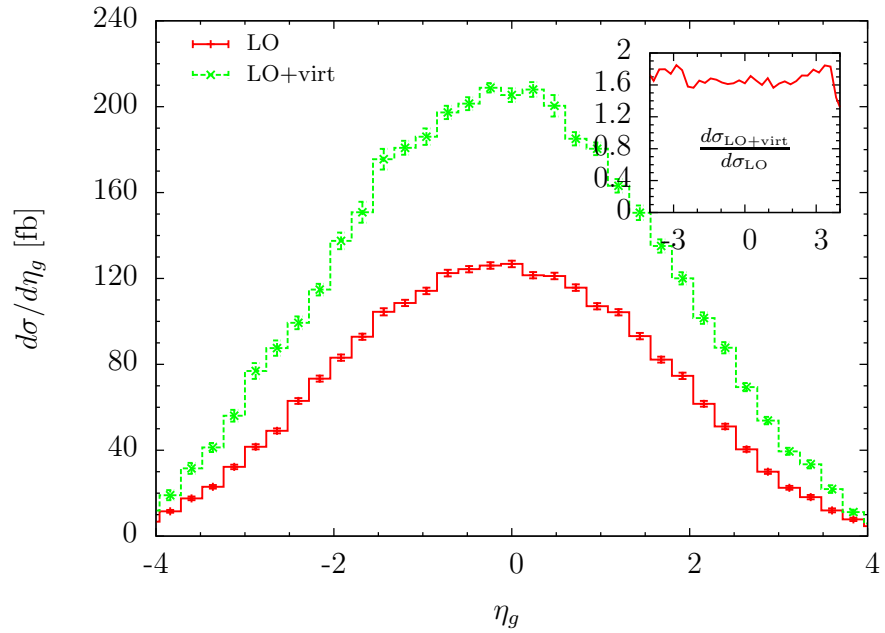


Figure 6.5: Pseudo-rapidity distribution for the gluon. Details as in Fig. 6.3.

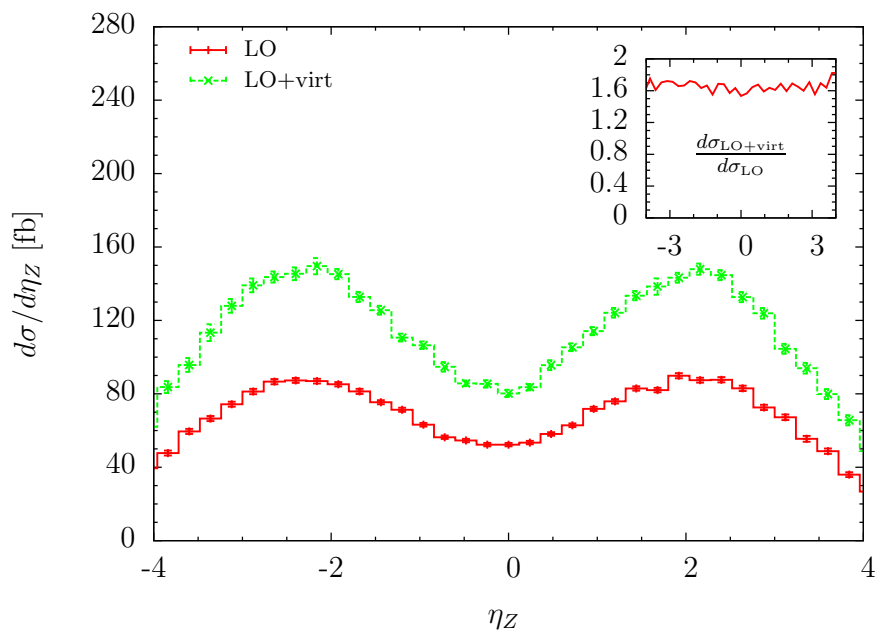


Figure 6.6: Pseudo-rapidity distribution for a Z boson. Details as in Fig. 6.3.

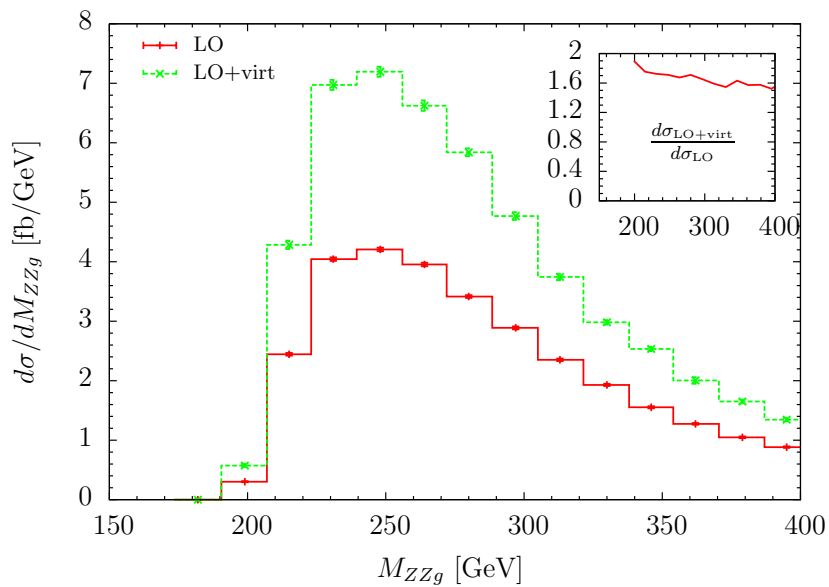


Figure 6.7: Invariant mass distribution for the sum of the three final states, ZZg . Details as in Fig. 6.3.

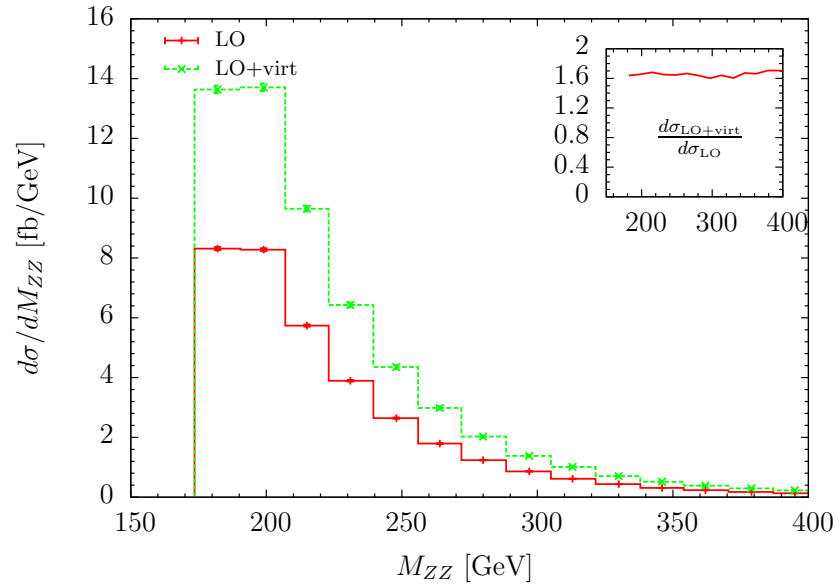


Figure 6.8: Invariant mass distribution for the Z boson pair. Details as in Fig. 6.3.

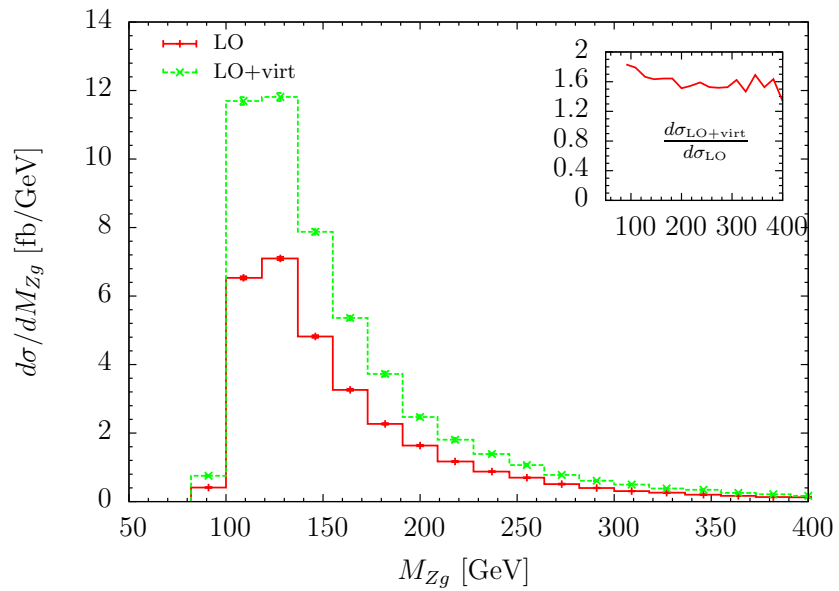


Figure 6.9: Invariant mass distribution for a Zg pair. Details as in Fig. 6.3.

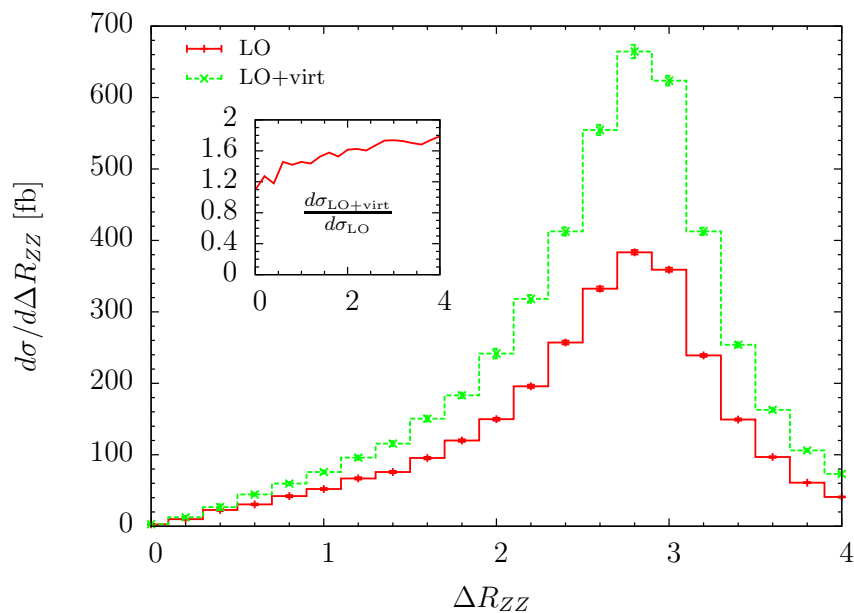


Figure 6.10: Distribution of the distance ΔR_{ZZ} of the Z boson pair. Details as in Fig. 6.3.

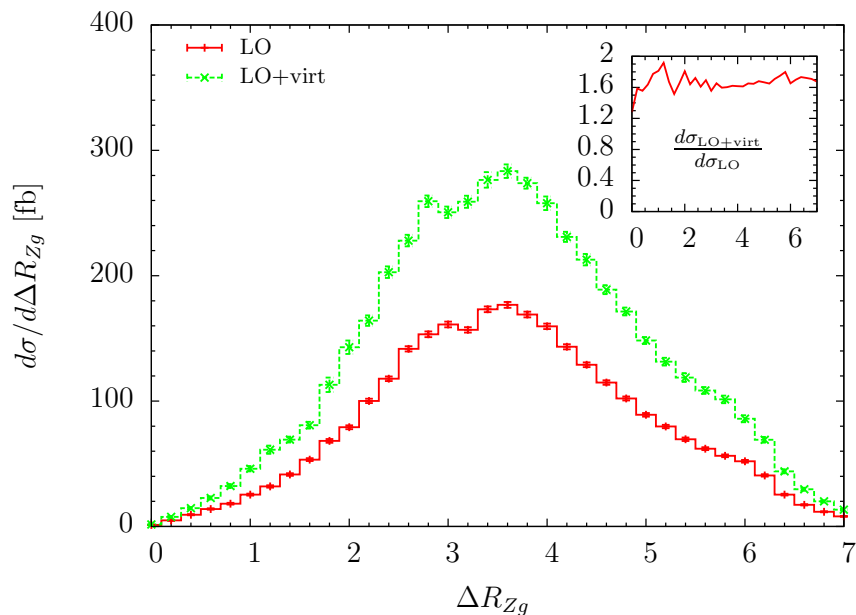


Figure 6.11: Distribution of the distance ΔR_{Zg} of a Z boson and the gluon. Details as in Fig. 6.3.

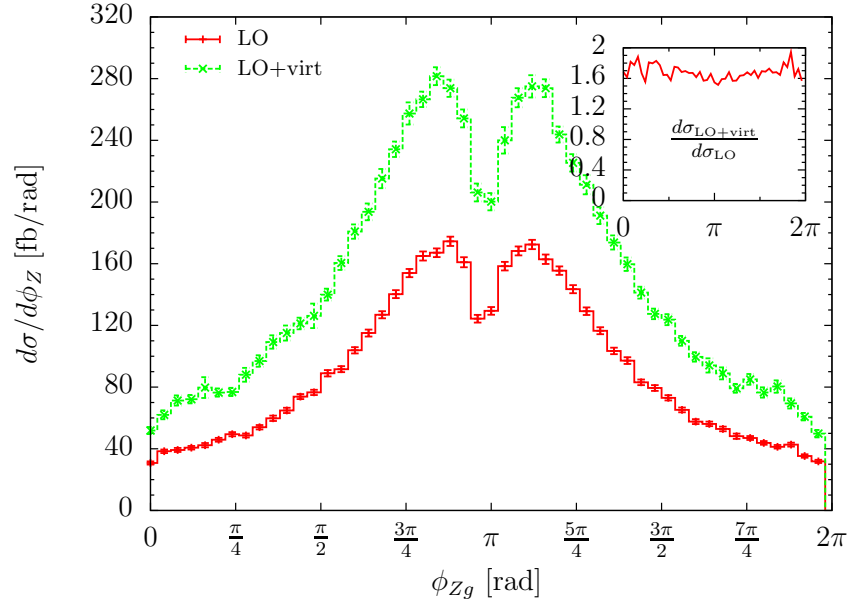


Figure 6.12: Distribution of difference of the azimuthal angles ϕ of a Z boson and a gluon. Details as in Fig. 6.3.

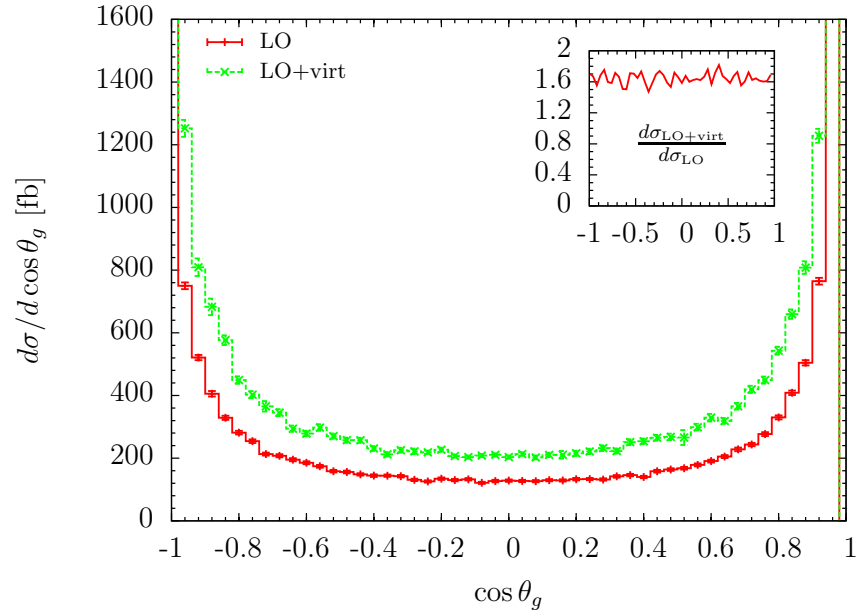


Figure 6.13: Distribution of the polar angle θ of the gluon. Details as in Fig. 6.3.

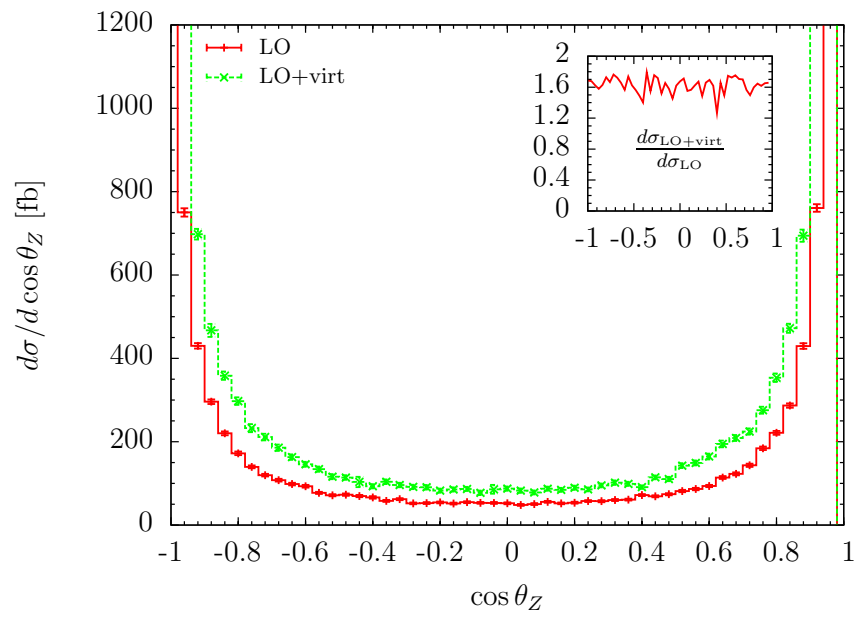


Figure 6.14: Distribution of the polar angle θ of a Z boson. Details as in Fig. 6.3.

Summary

In this thesis, production processes related to Higgs physics at the upcoming Large Hadron Collider at CERN were considered. The discussion of these processes requires a thorough introduction of the underlying theoretical aspects of Higgs physics in a quantum field theoretical framework and a description of Higgs phenomenology at the LHC. First, the Higgs mechanism and constraints on the mass of the SM Higgs boson were explained in detail. Moreover, production modes and decay channels of the Higgs boson, relevant at the LHC were presented. Subsequently, we described the framework for perturbative calculations of cross sections involving hadrons, the proton being an example and used as a projectile at the LHC. This is necessary since hadrons are bound states of quarks and gluons and not directly accessible with perturbative methods. Due to the property of asymptotic freedom of the underlying theory, high energy collisions of hadrons can be divided into a soft part and a hard scattering process, described by the parton model. The soft part is perturbatively inaccessible, but can be parameterised in terms of universal and measurable parton distribution functions. Contrary to the soft part, reliable theoretical predictions with perturbation theory can be obtained for the hard scattering process involving quarks and gluons. The conceptual complications appearing at higher orders were qualitatively discussed. Finally, special emphasis has been placed on the presentation of efficient methods of multi-leg one-loop amplitudes which are crucial for precise predictions of scattering processes at the LHC. The spinor helicity formalism and colour decomposition enables us to decompose scattering amplitudes into simpler pieces. At the loop level, these are usually divergent. Details have been given on the regularisation of these divergences and the required renormalisation of the theory. A detailed introduction into a new reduction algorithm for multi-leg one-loop integrals avoiding the deficiencies of standard algorithms finished the description of the theoretical framework and calculational methods needed in this thesis.

Two classes of scattering processes which involve multi-leg one-loop integrals were calculated and analysed in the phenomenological part of this work. The study of multi-Higgs boson production via gluon fusion principally enables us to reconstruct the SM Higgs potential, the basic ingredient of the Higgs mechanism which sheds light

on the question where elementary particles get their mass from. The SM Higgs potential implies trilinear and quartic self-interactions of the Higgs boson which have to be confirmed experimentally. The production of two or three Higgs bosons via gluon fusion is loop-induced, leading to complicated loop integrals. These were calculated with the application of new reduction methods. We studied the experimental accessibility at the LHC in the SM and beyond. We found that the contributions from pentagon, box and triangle topologies show a strong interference pattern, only the latter being sensitive to the quartic Higgs coupling for 3-Higgs production. The cross section for 3-Higgs production can be very sensitive to the variation of the quartic Higgs coupling. For a Higgs mass of $m_H = 200$ GeV for instance, it affects the cross section by -57.5%. We also studied the dependence of the cross sections on the unphysical renormalisation scale μ_R and factorisation scale μ_F . Setting $\mu_R = \mu_F$, a variation by a factor of 3 exhibited an uncertainty of about 50%, typical for LO QCD cross sections. The application of the heavy top approximation, important for single Higgs production, would allow for a NLO calculation, thereby reducing the scale uncertainties. However, a comparison of total cross sections for 2- and 3-Higgs production, computed with exact matrix elements and in the limit $m_t \rightarrow \infty$, proved that this approximation is not applicable for multi-Higgs production. In summary, the SM cross sections for 3-Higgs production are too small to be observed at the LHC, making the quartic coupling experimentally inaccessible. The experimental situation improves in certain extensions of the SM. Magnitude and sign of the trilinear and quartic coupling can be arbitrary, if one includes higher dimensional operators in the Higgs potential in the framework of an effective theory. This potentially leads to strongly enhanced cross sections. In 2-Higgs-doublet models, like the MSSM, two amplification effects were observed. Contributions to the cross sections from bottom quark loops, negligible in the SM, are strongly enhanced for large $\tan\beta$. Nevertheless, this amplification effect doesn't increase the 3-Higgs production cross section above 1 fb at the LHC. However, resonance effects due to an internal heavy Higgs boson decaying into two or three light Higgs bosons can enhance the 3-Higgs cross section into the $\mathcal{O}(10)$ fb region, which is potentially observable. Multi-Higgs boson production therefore is an interesting probe of Higgs sectors beyond the SM.

The second class of processes considers the hadronic production of a pair of electroweak vector bosons in association with a jet at NLO. This level of accuracy is mandatory for reliable theoretical predictions at the LHC. In fact, this process is of high phenomenological relevance. The decay of the Higgs boson to a pair of vector bosons is a promising channel for the Higgs search at the LHC in the low mass range, and a significant fraction of Higgs bosons is produced in association with a hard jet. The calculation of $PP \rightarrow VV + \text{jet}$ is important for understanding the background to this process. The virtual QCD corrections $q\bar{q} \rightarrow VVg$ are also needed for a complete NNLO QCD calculation for the production of a pair of electroweak vector bosons.

The calculation of $PP \rightarrow VV + \text{jet}$ is of considerable complexity. The most serious challenge is the computation of the virtual corrections, which has been solved in this

work by applying efficient reduction techniques for complicated one-loop (pentagon) diagrams. The resulting analytic expressions are generated with highly automated computer routines and translated into a flexible Fortran code, which can be employed in the computation of differential cross sections of phenomenological interest. The impact of these corrections has been shown for several differential distributions which are typically used in phenomenological studies. The results indicate that the QCD corrections are sizable and should be taken into account in experimental studies for the LHC. The inclusion of the real corrections, necessary for a complete NLO prediction, can be achieved with standard techniques and will be added in the near future.

Analytical evaluation of a one-loop scalar integral



In this appendix, we evaluate the 3-mass box function $I_4^n(s, t, s_1, s_2, s_3, 0)$ with massless propagators. The external momenta are denoted by $p_i, i = 1 \dots 4$, and the Mandelstam invariants by $s_i = p_i^2 = -S_i, s = (p_1 + p_2)^2 = -S, t = (p_1 + p_3)^2 = -T$. p_4 is chosen to be lightlike, $s_4 = 0$.

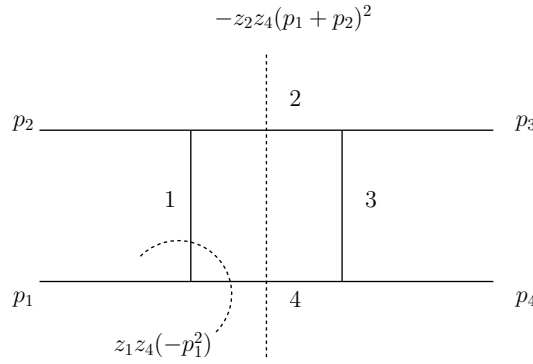


Figure A.1: Scalar box integral

After Feynman parametrisation and integration over the loop momentum, we obtain

$$I_4^n = \Gamma(4 - \frac{n}{2}) \int dz_1 dz_2 dz_3 dz_4 \delta(1 - \sum_{i=1}^4 z_i) \frac{1}{\mathcal{F}^{4-\frac{n}{2}}}$$

$$\mathcal{F} = S_1 z_1 z_4 + S_2 z_1 z_2 + S_3 z_2 z_3 + z_2 z_4 S + z_1 z_3 T - i\delta, \quad (\text{A.1})$$

where \mathcal{F} can be also obtained from the single- and double-cuts of the box diagram, as indicated in Fig. A.1. We apply the following parametrisation of the Feynman variables $(z_1 z_2 z_3 z_4) \rightarrow (u x z)$, where the Jacobian of transformation is denoted by $\det J$, and we use the notation $\bar{x} = (1 - x)$:

$$z_1 = u x z$$

$$\begin{aligned}
z_2 &= \bar{u} x z \\
z_3 &= v \bar{x} z \\
z_4 &= \bar{v} \bar{x} z \\
\det J &= x \bar{x}
\end{aligned}$$

The delta function transforms into $\delta(1-z)$, therefore we can substitute $z = 1$ and are left with three integrations. The above choice leads to a simple starting point which allows us to easily integrate over v . Performing the transformation, we obtain

$$\begin{aligned}
\mathcal{F} &= x \hat{\mathcal{F}} \\
\hat{\mathcal{F}} &= u \bar{v} \bar{x} S_1 + u \bar{u} x S_2 + \bar{u} v \bar{x} S_3 + \bar{u} \bar{v} \bar{x} S + u v \bar{x} T - i \delta.
\end{aligned} \tag{A.2}$$

With $n = 4 - 2\epsilon$, we get

$$\frac{\partial}{\partial v} \hat{\mathcal{F}}^{-1-\epsilon} = (-1 - \epsilon) \hat{\mathcal{F}}^{-2-\epsilon} \cdot \bar{x} (-u S_1 + \bar{u} S_3 - \bar{u} S + u T). \tag{A.3}$$

Using $\Gamma(4 - \frac{n}{2}) = \Gamma(2 + \epsilon) = (1 + \epsilon) \Gamma(1 + \epsilon)$, we obtain

$$\begin{aligned}
I_4^n &= -\Gamma(1 + \epsilon) \int_0^1 du dv dx \frac{\bar{x} x^{-1-\epsilon}}{\bar{x} \beta} \left(\frac{\partial}{\partial v} \hat{\mathcal{F}}^{-1-\epsilon} \right) \\
&= -\Gamma(1 + \epsilon) \int_0^1 du dx \frac{x^{-1-\epsilon}}{\beta} \left(\hat{\mathcal{F}}^{-1-\epsilon}(v=1) - \hat{\mathcal{F}}^{-1-\epsilon}(v=0) \right),
\end{aligned}$$

where we introduced the shorthand notation

$$\beta = -u S_1 + \bar{u} S_3 - \bar{u} S + u T = u(S_2 - U) - S + S_3.$$

In the next step, we perform the x -integration.

$$\hat{\mathcal{F}}(v=1) = u \bar{u} x S_2 + \bar{u} \bar{x} S_3 + u \bar{x} T - i \delta \tag{A.4}$$

$$\hat{\mathcal{F}}(v=0) = u \bar{x} S_1 + u \bar{u} x S_2 + \bar{u} \bar{x} S - i \delta \tag{A.5}$$

Both terms in the integral are not regular in the limit $x \rightarrow 0$, therefore we subtract (and add) $\hat{\mathcal{F}}^{-1-\epsilon}(v=1, 0)|_{x=0}$. For $(\hat{\mathcal{F}}^{-1-\epsilon}(v=1, 0) - \hat{\mathcal{F}}^{-1-\epsilon}(v=1, 0)|_{x=0})$ we can safely set $\epsilon = 0$. For the terms

$$\hat{\mathcal{F}}(v=1)|_{x=0} = \bar{u} S_3 + u T - i \delta = A - i \delta \tag{A.6}$$

$$\hat{\mathcal{F}}(v=0)|_{x=0} = u S_1 + \bar{u} S - i \delta = B - i \delta \tag{A.7}$$

the x integration is trivial, we only need

$$\int_0^1 dx x^{-1-\epsilon} = \int_0^1 dx \frac{-1}{\epsilon} \frac{d}{dx} (x^{-\epsilon}) \quad (\text{A.8})$$

$$\stackrel{\epsilon \leq 0}{=} -\frac{1}{\epsilon} (1^{|\epsilon|} - 0^{|\epsilon|}) = -\frac{1}{\epsilon}.$$

Now, we have

$$I_4^n = - \int_0^1 du dx \frac{1}{x} \frac{1}{\beta} [(u\bar{u}xS_2 - \bar{u}xS_3 + \bar{u}S_3 - uxT + uT - i\delta)^{-1} - (\bar{u}S_3 + uT - i\delta)^{-1}]$$

$$- [(-uxS_1 + uS_1 + u\bar{u}xS_2 - \bar{u}xS + \bar{u}S - i\delta)^{-1} - (uS_1 + \bar{u}S - i\delta)^{-1}]$$

$$+ \Gamma(\epsilon) \int_0^1 du \frac{1}{\beta} [(\bar{u}S_3 + uT - i\delta)^{-1-\epsilon} - (uS_1 + \bar{u}S - i\delta)^{-1-\epsilon}]. \quad (\text{A.9})$$

In the first two lines of A.9, the $1/x$ cancels by construction. We use $(ax+b)^{-1} - b^{-1} = -ax \cdot [(ax+b)b]^{-1}$, the Taylor expansion $y^{-1-\epsilon} = 1/y - \epsilon \log(y)/y$ and the trivial integral

$$\int_0^1 dx \frac{a}{ax+b-i\delta} = \log \left(\frac{a+b-i\delta}{b-i\delta} \right)$$

to get

$$I_4^n = \int_0^1 du \frac{1}{\beta} \left[\frac{1}{A} \log \left(\frac{u\bar{u}S_2 - i\delta}{A - i\delta} \right) - \frac{1}{B} \log \left(\frac{u\bar{u}S_2 - i\delta}{B - i\delta} \right) \right]$$

$$+ \Gamma(\epsilon) \left[\int_0^1 du \frac{1}{\beta} \left(\frac{1}{A} - \frac{1}{B} - \epsilon \frac{1}{A} \log(A - i\delta) + \epsilon \frac{1}{B} \log(B - i\delta) \right) \right]. \quad (\text{A.10})$$

The term $\epsilon \Gamma(\epsilon) = \Gamma(1 + \epsilon) = 1 + \mathcal{O}(\epsilon)$ contributes to the finite part. We can remove β by using

$$\frac{1}{\beta} \left(\frac{1}{A} - \frac{1}{B} \right) = -\frac{1}{AB} \quad (\text{A.11})$$

Furthermore, we use partial fractioning and obtain

$$\frac{1}{AB} = \frac{1}{ST - S_1S_3} \left(\frac{T - S_3}{S_3 + u(T - S_3)} - \frac{S_1 - S}{S + u(S_1 - S)} \right)$$

$$\begin{aligned}\frac{1}{\beta A} &= \frac{1}{ST - S_1 S_3} \left(\frac{S + T - S_1 - S_3}{\beta} - \frac{T - S_3}{A} \right) \\ \frac{1}{\beta B} &= \frac{1}{ST - S_1 S_3} \left(\frac{S + T - S_1 - S_3}{\beta} - \frac{S_1 - S}{B} \right).\end{aligned}$$

The divergent part of I_4^n is therefore given by

$$I_{4,div}^n = -\Gamma(\epsilon) \frac{1}{ST - S_1 S_3} \left(\log \left(\frac{T - i\delta}{S_3 - i\delta} \right) - \log \left(\frac{S_1 - i\delta}{S - i\delta} \right) \right). \quad (\text{A.12})$$

The finite part is given by

$$\begin{aligned}I_{4,fin}^n &= \frac{1}{ST - S_1 S_3} \int_0^1 du \left[\left(\frac{T - S_3}{A} - \frac{S_1 - S}{B} \right) \cdot (-\log(u\bar{u}) - \log(S_2 - i\delta)) \right. \\ &\quad + 2(T - S_3) \frac{\log(A - i\delta)}{A} - 2(S_1 - S) \frac{\log(B - i\delta)}{B} \\ &\quad \left. - 2 \frac{S + T - S_1 - S_3}{\beta} (\log(A - i\delta) - \log(B - i\delta)) \right]. \quad (\text{A.13})\end{aligned}$$

With the definition of the dilogarithm,

$$\text{Li}_2(z) = - \int_0^z dt \frac{\log(1-t)}{t}, \quad (\text{A.14})$$

and the identity

$$\text{Li}_2(z) + \text{Li}_2(\bar{z}) = \text{Li}_2(1) - \log(z) \log(\bar{z}), \quad (\text{A.15})$$

one shows

$$\int_0^1 du \frac{a \log(u)}{au + b} = \text{Li}_2\left(-\frac{a}{b}\right), \quad \int_0^1 du \frac{a \log(\bar{u})}{au + b} = -\text{Li}_2\left(\frac{a}{a+b}\right).$$

With the use of another dilog identity,

$$\text{Li}_2(1-x) + \text{Li}_2\left(1 - \frac{1}{x}\right) = -\frac{1}{2} \log^2(x), \quad (\text{A.16})$$

we get

$$\begin{aligned}
I_1 &= - \int_0^1 du \left(\frac{T - S_3}{A} - \frac{S_1 - S}{B} \right) (\log(u) + \log(\bar{u})) \\
&= \frac{1}{2} \log^2 \left(\frac{T}{S_3} \right) + 2 \text{Li}_2 \left(1 - \frac{S_3}{T} \right) + \frac{1}{2} \log^2 \left(\frac{S_1}{S} \right) + 2 \text{Li}_2 \left(1 - \frac{S_1}{S} \right).
\end{aligned} \tag{A.17}$$

The elementary integral

$$\int da \frac{\log(a)}{a} = \frac{1}{2} \log^2(a)$$

leads to

$$\begin{aligned}
I_2 &= 2 \int_0^1 du \left((T - S_3) \frac{\log(A - i\delta)}{A} - (S_1 - S) \frac{\log(B - i\delta)}{B} \right) \\
&= \log^2(T - i\delta) - \log^2(S_3 - i\delta) - \log^2(S_1 - i\delta) + \log^2(S - i\delta).
\end{aligned} \tag{A.18}$$

For the remaining terms, we introduce the R function [119], which is defined by

$$\begin{aligned}
R(y_0, \hat{z}) &= \int_0^1 dy \frac{\log(y - \hat{z}) - \log(y_0 - \hat{z})}{y - y_0} \\
&= \text{Li}_2(z_1) - \text{Li}_2(z_2) + \eta_1 \log(z_1) - \eta_2 \log(z_2),
\end{aligned} \tag{A.19}$$

where

$$\begin{aligned}
z_1 &= \frac{y_0}{y_0 - \hat{z}} \\
z_2 &= \frac{y_0 - 1}{y_0 - \hat{z}} \\
\eta_1 &= \eta(-\hat{z}, 1/(y_0 - \hat{z})) \\
\eta_2 &= \eta(1 - \hat{z}, 1/(y_0 - \hat{z})) \\
\eta(x, y) &= \log(xy) - \log(x) - \log(y).
\end{aligned} \tag{A.20}$$

The η function is nonzero, if one crosses the branch cut on the Riemann-sheet of the logarithm along the negative real axis when multiplying complex numbers. In the R function, y_0 is supposed to be real valued but \hat{z} needs to have a non-vanishing

imaginary part. For the integral

$$\int_0^1 du \frac{1}{u - u_0} \left(\frac{\log(A - i\delta)}{u - u_0} - \frac{\log(B - i\delta)}{u - u_0} \right)$$

with

$$\begin{aligned} a_1 &= T - S_3, & b_1 &= S_3, \\ a_2 &= S_1 - S, & b_2 &= S, & u_0 &= \frac{S - S_3}{T + S - S_1 - S_3} \end{aligned}$$

we can add a convenient $\log 1 = \log((a_1 u_0 + b_1 - i\delta)/(a_2 u_0 + b_2 - i\delta))$ and use $\log x - \log y = \log(x/y)$ to obtain

$$\begin{aligned} &\int_0^1 du \frac{1}{u - u_0} \left(\log(a_1 u + b_1 - i\delta) - \log(a_1 u_0 + b_1 - i\delta) \right. \\ &\quad \left. - \log(a_2 u + b_2 - i\delta) + \log(a_2 u_0 + b_2 - i\delta) \right) \\ &= \int_0^1 du \frac{1}{u - u_0} \left(\log \left(u + \frac{b_1 - i\delta}{a_1} \right) - \log \left(u_0 + \frac{b_1 - i\delta}{a_1} \right) \right. \\ &\quad \left. - \log \left(u + \frac{b_2 - i\delta}{a_2} \right) + \log \left(u_0 + \frac{b_2 - i\delta}{a_2} \right) \right) \\ &= R(u_0, -\frac{b_1 - i\delta}{a_1}) - R(u_0, -\frac{b_2 - i\delta}{a_2}). \quad (\text{A.21}) \end{aligned}$$

Combining all results, we arrive at

$$\begin{aligned} I_{4,fin}^n &= \frac{1}{ST - S_1 S_3} \left[\frac{3}{2} \log^2(T - i\delta) + \frac{3}{2} \log^2(S - i\delta) - \frac{1}{2} \log^2(S_1 - i\delta) - \frac{1}{2} \log^2(S_3 - i\delta) \right. \\ &\quad \left. - \log(T - i\delta) \log(S_3 - i\delta) - \log(S_1 - i\delta) \log(S - i\delta) - \log(S_2 - i\delta) \left(\log \left(\frac{T - i\delta}{S_3 - i\delta} \right) - \log \left(\frac{S_1 - i\delta}{S - i\delta} \right) \right) \right. \\ &\quad \left. + 2 \text{Li}_2 \left(1 - \frac{S_3 - i\delta}{T - i\delta} \right) + 2 \text{Li}_2 \left(1 - \frac{S_1 - i\delta}{S - i\delta} \right) - 2 R \left(u_0, -\frac{S_3 - i\delta}{T - S_3} \right) + 2 R \left(u_0, -\frac{S - i\delta}{S_1 - S} \right) \right]. \quad (\text{A.22}) \end{aligned}$$

A comparison with [117] shows that the first two lines of A.22 agree with the results in [117], only the last line is written as sum of three dilogs: (replacement rule:

$$(-s, -t, -m_{1,2,3,4}^2) \rightarrow (T, S, S_{4,1,2,3})$$

$$-2 \operatorname{Li}_2 \left(1 - \frac{S_1}{T} \right) - 2 \operatorname{Li}_2 \left(1 - \frac{S_3}{S} \right) + 2 \operatorname{Li}_2 \left(1 - \frac{S_1 S_3}{T S} \right) \quad (\text{A.23})$$

This is strictly only correct in the Euclidean region, where all Mandelstam invariants are negative. The analytic continuation to positive values for most terms is simply given by the replacement $s \rightarrow s + i\delta$. No cut will be hit by logarithms, dilogarithms and exponentials of the form $(-s - i\delta)^{-\epsilon}$. For dilogarithms of a product of ratios, more care has to be taken. The replacement rule in [60] reads:

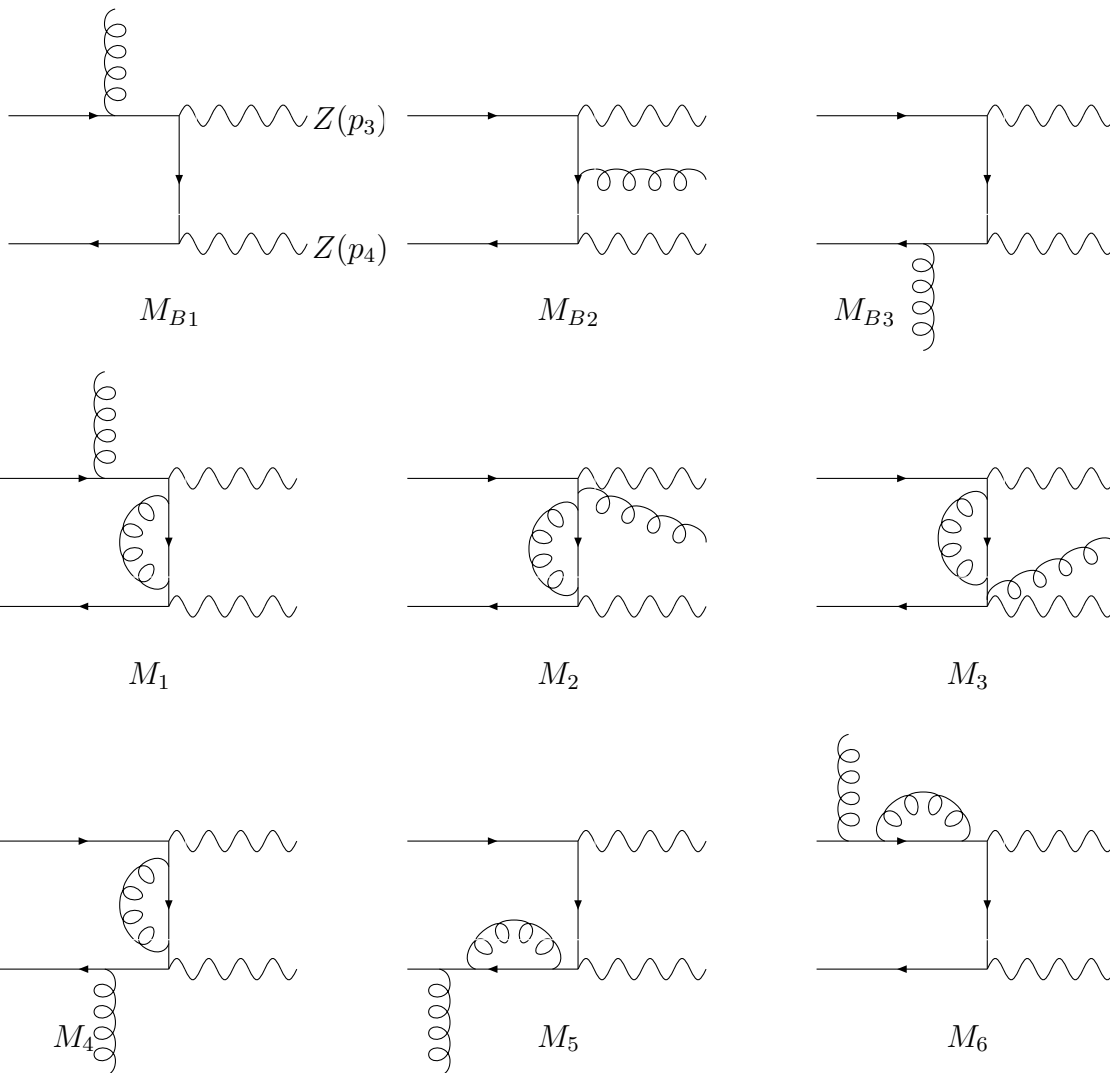
$$\begin{aligned} \operatorname{Li}_2 \left(1 - \frac{s_1 s_2}{s_3 s_4} \right) &\rightarrow \operatorname{Li}_2 \left(1 - \frac{s_1 + i\delta}{s_3 + i\delta} \frac{s_2 + i\delta}{s_4 + i\delta} \right) \\ &+ \eta \left(\frac{s_1 + i\delta}{s_3 + i\delta}, \frac{s_2 + i\delta}{s_4 + i\delta} \right) \log \left(1 - \frac{s_1 + i\delta}{s_3 + i\delta} \frac{s_2 + i\delta}{s_4 + i\delta} \right). \end{aligned} \quad (\text{A.24})$$

The final result A.22 agrees with the formulae in [117], if (A.24) is taken into account.

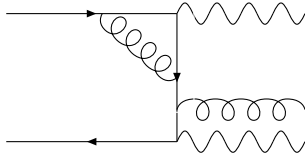
Feynman diagrams for $q\bar{q} \rightarrow ZZg$

B

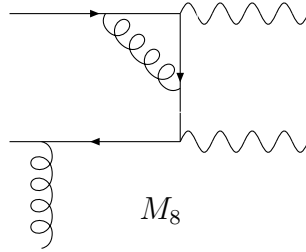
For each diagram shown below, one has to add a diagram with the exchange of the momenta of the vector bosons.



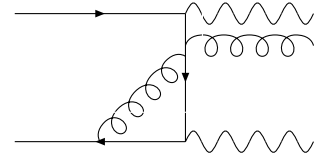
B Feynman diagrams for $q\bar{q} \rightarrow ZZg$



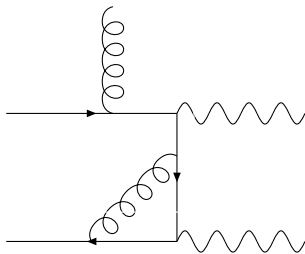
M_7



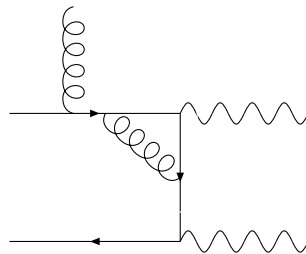
M_8



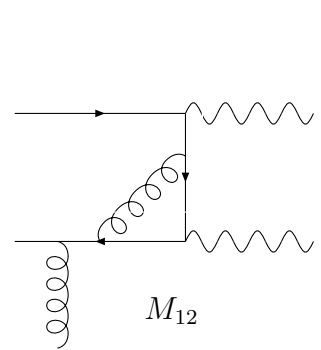
M_9



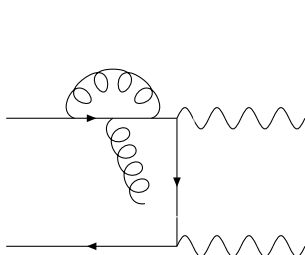
M_{10}



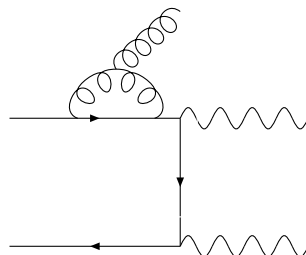
M_{11}



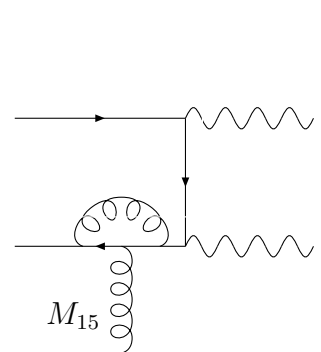
M_{12}



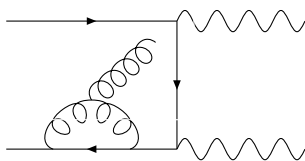
M_{13}



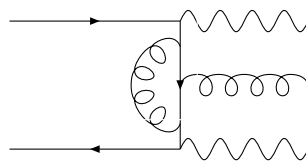
M_{14}



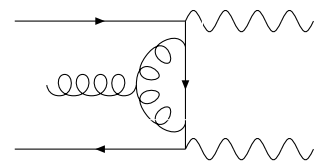
M_{15}



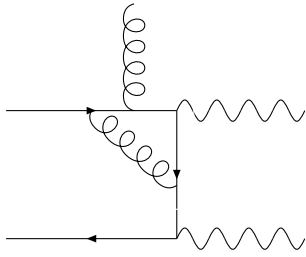
M_{16}



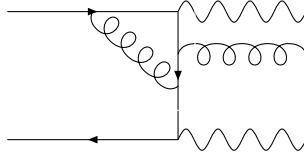
M_{17}



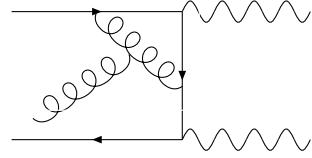
M_{18}



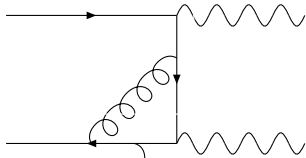
M_{19}



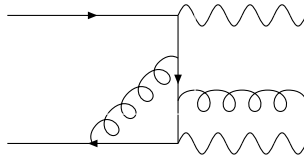
M_{20}



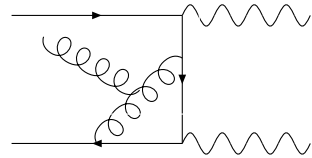
M_{21}



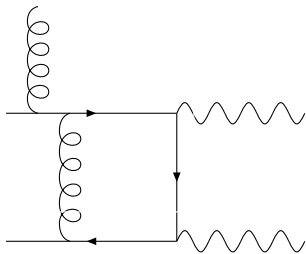
M_{22}



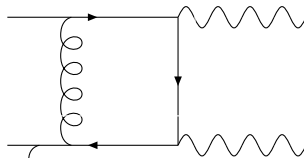
M_{23}



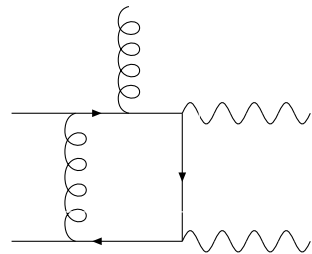
M_{24}



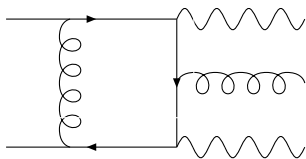
M_{25}



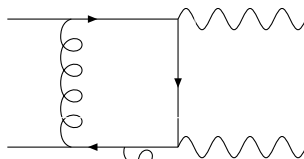
M_{26}



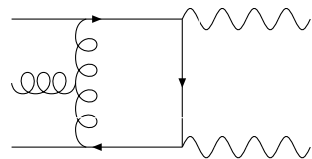
M_{27}



M_{28}

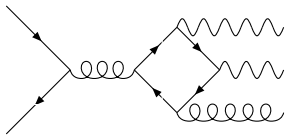


M_{29}

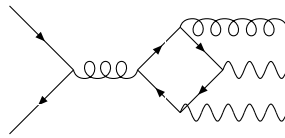


M_{30}

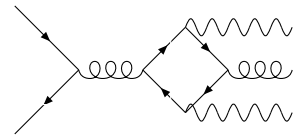
B Feynman diagrams for $q\bar{q} \rightarrow ZZg$



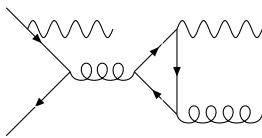
M_{31}



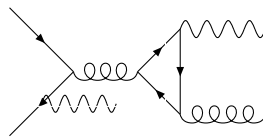
M_{32}



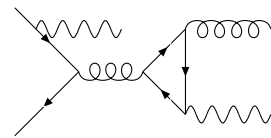
M_{33}



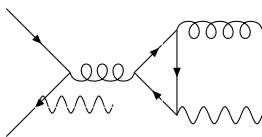
M_{34}



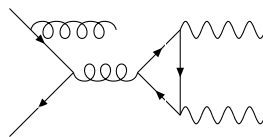
M_{35}



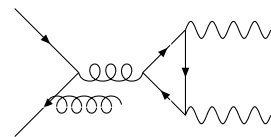
M_{36}



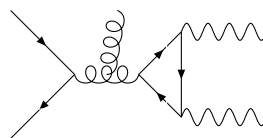
M_{37}



M_{38}



M_{39}



M_{40}

Bibliography

- [1] T. Binoth, S. Karg, N. Kauer and R. Rückl, Phys. Rev. D **74** (2006) 113008 [[arXiv:hep-ph/0608057](#)].
- [2] T. Binoth, A. Guffanti, J. P. Guillet, S. Karg, N. Kauer and T. Reiter, Nucl. Phys. Proc. Suppl. **160** (2006) 61 [[arXiv:hep-ph/0606318](#)].
- [3] P.W. Higgs, Phys. Rev. Lett. **12** (1964) 132 and Phys. Rev. **145** (1966) 1156; F. Englert and R. Brout, Phys. Rev. Lett. **13** (1964) 321; G.S. Guralnik, C.R. Hagen and T.W. Kibble, Phys. Rev. Lett. **13** (1964) 585.
- [4] M.E. Peskin, D.V. Schroeder, *An Introduction to Quantum Field Theory*, Westview Press, ISBN 0-201-50397-2.
- [5] Y. Nambu, Phys. Rev. Lett. **4** (1960) 380; Y. Nambu and G. Jona-Lasinio, Phys. Rev. **122** (1961) 345; *ibid.* Phys. Rev. **124** (1961) 246; J. Goldstone, Nuov. Cim. **19** (1961) 154; J. Goldstone, A. Salam and S. Weinberg, Phys. Rev. **127** (1962) 965.
- [6] T. Kugo and I. Ojima, Prog. Theor. Phys. **60** (1978) 1869; T. Kugo and I. Ojima, Prog. Theor. Phys. **61** (1979) 294; T. Kugo and I. Ojima, Prog. Theor. Phys. Suppl. **66** (1979) 1.
- [7] C. Becchi, A. Rouet and R. Stora, Phys. Lett. B **52** (1974) 344; C. Becchi, A. Rouet and R. Stora, Commun. Math. Phys. **42** (1975) 127.
- [8] W. J. Marciano and S. S. D. Willenbrock, Phys. Rev. D **37** (1988) 2509; S. Dawson and S. Willenbrock, Phys. Rev. Lett. **62** (1989) 1232.
- [9] K. Riesselmann and S. Willenbrock, Phys. Rev. D **55** (1997) 311 [[arXiv:hep-ph/9608280](#)].
- [10] M. Luscher and P. Weisz, Nucl. Phys. B **318** (1989) 705.
- [11] T. Hambye and K. Riesselmann, Phys. Rev. D **55** (1997) 7255 [[arXiv:hep-ph/9610272](#)].

- [12] R. Barate *et al.* [LEP Working Group for Higgs boson searches], Phys. Lett. B **565** (2003) 61 [[arXiv:hep-ex/0306033](#)].
- [13] LEP Electroweak Working Group, <http://lepewwg.web.cern.ch/LEPEWWG/>
- [14] J. Alcaraz *et al.* [ALEPH Collaboration], [arXiv:hep-ex/0612034](#).
- [15] J. Abdallah *et al.* [DELPHI Collaboration], Eur. Phys. J. C **28** (2003) 15 [[arXiv:hep-ex/0303033](#)].
- [16] [ALEPH Collaboration], Phys. Rept. **427** (2006) 257 [[arXiv:hep-ex/0509008](#)].
- [17] M. S. Carena *et al.* [Higgs Working Group Collaboration], [[arXiv:hep-ph/0010338](#)].
- [18] V. Buscher and K. Jakobs, Int. J. Mod. Phys. A **20** (2005) 2523 [[arXiv:hep-ph/0504099](#)].
- [19] R. Harlander and W. Kilgore, [[arXiv:hep-ph/0211380](#)].
- [20] W. Beenakker, S. Dittmaier, M. Krämer, B. Plümper, M. Spira and P.M. Zerwas, Phys. Rev. Lett. **87** (2001) 201805;
W. Beenakker, S. Dittmaier, M. Krämer, B. Plümper, M. Spira and P.M. Zerwas, Nucl. Phys. **B653** (2003) 151, [[arXiv:hep-ph/0211352](#)].
- [21] L. Reina, S. Dawson, Phys. Rev. Lett. **87** (2001) 201804;
L. Reina, S. Dawson, D. Wackerroth, Phys. Rev. **D65** (2002) 053017;
S. Dawson, L.H. Orr, L. Reina, D. Wackerroth, Phys. Rev. **D67** (2003) 071503.
- [22] T. Han, G. Valencia, S. Willenbrock, Phys. Rev. Lett. **69** (1992) 3274.
- [23] T. Figy, C. Oleari and D. Zeppenfeld, Phys. Rev. **D68** (2003) 073005, [[arXiv:hep-ph//0306109](#)];
E. L. Berger and J. Campbell, Phys. Rev. **D70** (2004) 073011, [[arXiv:hep-ph//0403194](#)].
- [24] T. Han, S. Willenbrock, Phys. Lett. **B273** (1991) 167;
A. Djouadi, M. Spira, Phys. Rev. **D62** (2000) 014004.
- [25] A. Djouadi, J. Kalinowski and M. Spira, Comput. Phys. Commun. 108 (1998) 56.
- [26] A. Djouadi, [[arXiv:hep-ph/0503172](#)].
- [27] ATLAS TDR, report CERN/LHCC/99-15 (1999).
- [28] S. Asai *et al.*, Eur. Phys. J. C **32S2** (2004) 19 [[arXiv:hep-ph/0402254](#)].

-
- [29] S. R. Coleman and D. J. Gross, Phys. Rev. Lett. **31** (1973) 851.
- [30] J. D. Bjorken, Phys. Rev. **179**, 1547 (1969).
- [31] R. P. Feynman, Phys. Rev. Lett. **23** (1969) 1415.
- [32] T. Kinoshita, J. Math. Phys. **3** (1962) 650.
- [33] T. D. Lee and M. Nauenberg, Phys. Rev. **133** (1964) B1549.
- [34] J. C. Collins, D. E. Soper and G. Sterman, Adv. Ser. Direct. High Energy Phys. **5** (1988) 1 [arXiv:hep-ph/0409313].
- [35] V. N. Gribov and L. N. Lipatov, Sov. J. Nucl. Phys. **15** (1972) 438 [Yad. Fiz. **15** (1972) 781]; G. Altarelli and G. Parisi, Nucl. Phys. B **126**, 298 (1977).
- [36] S. Catani and M. H. Seymour, Nucl. Phys. B **485** (1997) 291 [Erratum-ibid. B **510** (1998) 503] [arXiv:hep-ph/9605323].
- [37] A. D. Martin, R. G. Roberts, W. J. Stirling and R. S. Thorne, Eur. Phys. J. C **28** (2003) 455 [arXiv:hep-ph/021108]; A. D. Martin, R. G. Roberts, W. J. Stirling and R. S. Thorne, Eur. Phys. J. C **35** (2004) 325 [arXiv:hep-ph/0308087].
- [38] <http://durpdg.dur.ac.uk/hepdata/pdf3.html>
- [39] S. Weinzierl, arXiv:0707.3342 [hep-ph].
- [40] J. A. M. Vermaseren, arXiv:math-ph/0010025.
- [41] F.A. Berends, R. Kleiss, P. De Causmaecker, R. Gastmans and T.T. Wu, Phys. Lett. B103:124 (1981); P. De Causmaecker, R. Gastmans, W. Troost and T.T. Wu, Nucl. Phys. B206:53 (1982); R. Kleiss and W.J. Stirling, Nucl. Phys. B262:235 (1985); R. Gastmans and T.T. Wu, *The Ubiquitous Photon: Helicity Method for QED and QCD* (Clarendon Press, 1990).
- [42] Z. Xu, D. H. Zhang and L. Chang, Nucl. Phys. B **291** (1987) 392.
- [43] J.F. Gunion and Z. Kunszt, Phys. Lett. 161B:333 (1985).
- [44] L. J. Dixon, [arXiv:hep-ph/9601359].
- [45] F.A. Berends and W.T. Giele, Nucl. Phys. B294:700 (1987); M. Mangano, S. Parke and Z. Xu, Nucl. Phys. B298:653 (1988); M. Mangano, Nucl. Phys. B309:461 (1988).
- [46] Z. Bern and D.A. Kosower, Nucl. Phys. B362:389 (1991).

- [47] F. Maltoni, K. Paul, T. Stelzer and S. Willenbrock, Phys. Rev. D **67** (2003) 014026 [[arXiv:hep-ph/0209271](#)].
- [48] G. 't Hooft and M. J. G. Veltman, Nucl. Phys. B **44** (1972) 189.
- [49] C. G. Bollini and J. J. Giambiagi, Nuovo Cim. B **12** (1972) 20; J. F. Ashmore, Lett. Nuovo Cim. **4** (1972) 289; G. M. Cicuta and E. Montaldi, Lett. Nuovo Cim. **4** (1972) 329.
- [50] R. Gastmans and R. Meuldermans, Nucl. Phys. B **63** (1973) 277.
- [51] J. C. Collins, Cambridge, Uk: Univ. Pr. (1984).
- [52] W. Siegel, Phys. Lett. B **84** (1979) 193.
- [53] Z. Bern and D. A. Kosower, Nucl. Phys. B **379** (1992) 451.
- [54] S. Catani, M. H. Seymour and Z. Trocsanyi, Phys. Rev. D **55**, 6819 (1997) [[arXiv:hep-ph/9610553](#)].
- [55] M. J. G. Veltman, Nucl. Phys. B **319** (1989) 253.
- [56] F. Jegerlehner, Eur. Phys. J. C **18** (2001) 673 [[arXiv:hep-th/0005255](#)].
- [57] W. A. Bardeen, Phys. Rev. **184** (1969) 1848.
- [58] W.L. van Neerven, J.A.M. Vermaseren, Phys. Lett. B **137** (1984) 241.
- [59] R. Penrose, Proc. Cambridge Phil. Soc. **51**, 406-413, 1955.
- [60] T. Binoth, J. P. Guillet and G. Heinrich, Nucl. Phys. B **572** (2000) 361 [[arXiv:hep-ph/9911342](#)].
- [61] Z. Bern, L. Dixon, D.A. Kosower, Phys. Lett. B **302** (1993) 299; Nucl. Phys. B **412** (1994) 751.
- [62] T. Binoth, J. P. Guillet, G. Heinrich, E. Pilon and C. Schubert, JHEP **0510** (2005) 015 [[arXiv:hep-ph/0504267](#)].
- [63] M. Dührssen, S. Heinemeyer, H. Logan, D. Rainwater, G. Weiglein and D. Zepfenfeld, Phys. Rev. D **70** (2004) 113009 [[arXiv:hep-ph/0406323](#)].
- [64] G. Weiglein *et al.* [LHC/LC Study Group], “Physics interplay of the LHC and the ILC,” [[arXiv:hep-ph/0410364](#)].
- [65] A. Djouadi, W. Kilian, M. Muhlleitner and P. M. Zerwas, Eur. Phys. J. C **10** (1999) 27 [[arXiv:hep-ph/9903229](#)].

-
- [66] M. Battaglia, E. Boos and W. M. Yao, in *Proc. of the APS/DPF/DPB Summer Study on the Future of Particle Physics (Snowmass 2001)* ed. N. Graf, eConf **C010630** (2001) E3016 [[arXiv:hep-ph/0111276](#)].
- [67] A. Gutierrez-Rodriguez, M. A. Hernandez-Ruiz and O. A. Sampayo, [[arXiv:hep-ph/0601238](#)].
- [68] G. V. Jikia, Nucl. Phys. B **412** (1994) 57.
- [69] F. Boudjema and E. Chopin, Z. Phys. C **73** (1996) 85 [[arXiv:hep-ph/9507396](#)].
- [70] R. Belusevic and G. Jikia, Phys. Rev. D **70** (2004) 073017 [[arXiv:hep-ph/0403303](#)].
- [71] A. Djouadi, W. Kilian, M. Muhlleitner and P. M. Zerwas, Eur. Phys. J. C **10** (1999) 45 [[arXiv:hep-ph/9904287](#)].
- [72] U. Baur, T. Plehn and D. L. Rainwater, Phys. Rev. D **67** (2003) 033003 [[arXiv:hep-ph/0211224](#)].
- [73] U. Baur, T. Plehn and D. L. Rainwater, Phys. Rev. Lett. **89** (2002) 151801 [[arXiv:hep-ph/0206024](#)].
- [74] U. Baur, T. Plehn and D. L. Rainwater, Phys. Rev. D **68** (2003) 033001 [[arXiv:hep-ph/0304015](#)].
- [75] U. Baur, T. Plehn and D. L. Rainwater, Phys. Rev. D **69** (2004) 053004 [[arXiv:hep-ph/0310056](#)].
- [76] S. Dawson, C. Kao, Y. Wang and P. Williams, [[arXiv:hep-ph/0610284](#)].
- [77] L. G. Jin, C. S. Li, Q. Li, J. J. Liu and R. J. Oakes, Phys. Rev. D **71** (2005) 095004 [[arXiv:hep-ph/0501279](#)].
- [78] E. W. N. Glover and J. J. van der Bij, Nucl. Phys. B **309** (1988) 282.
- [79] T. Plehn, M. Spira and P. M. Zerwas, Nucl. Phys. B **479** (1996) 46 [Erratum-ibid. B **531** (1998) 655] [[arXiv:hep-ph/9603205](#)].
- [80] A. Krause, T. Plehn, M. Spira and P. M. Zerwas, Nucl. Phys. B **519** (1998) 85 [[arXiv:hep-ph/9707430](#)].
- [81] O. Brein and W. Hollik, Eur. Phys. J. C **13** (2000) 175 [[arXiv:hep-ph/9908529](#)].
- [82] T. Plehn and M. Rauch, Phys. Rev. D **72** (2005) 053008 [[arXiv:hep-ph/0507321](#)].
- [83] S. Kanemura, S. Kiyoura, Y. Okada, E. Senaha and C. P. Yuan, Phys. Lett. B **558** (2003) 157 [[arXiv:hep-ph/0211308](#)].

- [84] S. Kanemura, Y. Okada, E. Senaha and C. P. Yuan, Phys. Rev. D **70** (2004) 115002 [[arXiv:hep-ph/0408364](#)].
- [85] T. Appelquist and J. Carazzone, Phys. Rev. D **11** (1975) 2856.
- [86] V. Barger, T. Han, P. Langacker, B. McElrath and P. Zerwas, Phys. Rev. D **67** (2003) 115001 [[arXiv:hep-ph/0301097](#)].
- [87] C. O. Dib, R. Rosenfeld and A. Zerwekh, JHEP **0605** (2006) 074 [[arXiv:hep-ph/0509179](#)].
- [88] B. W. Lee, C. Quigg and H. B. Thacker, “Weak Interactions At Very High-Energies: The Role Of The Higgs Boson Mass,” Phys. Rev. D **16** (1977) 1519.
- [89] T. Binoth and J. J. van der Bij, Z. Phys. C **75** (1997) 17 [[arXiv:hep-ph/9608245](#)].
- [90] J. F. Gunion, H. E. Haber, G. L. Kane and S. Dawson, “The Higgs Hunter’s Guide,” SCIPP-89/13; “Errata for the Higgs hunter’s guide,” [[arXiv:hep-ph/9302272](#)].
- [91] H. E. Haber and R. Hempfling, Phys. Rev. D **48** (1993) 4280 [[arXiv:hep-ph/9307201](#)].
- [92] M. Carena, J. R. Espinosa, M. Quiros and C. E. M. Wagner, “Analytical expressions for radiatively corrected Higgs masses and couplings in the MSSM,” Phys. Lett. B **355** (1995) 209 [[arXiv:hep-ph/9504316](#)].
- [93] F. Boudjema and A. Semenov, Phys. Rev. D **66** (2002) 095007 [[arXiv:hep-ph/0201219](#)].
- [94] L. J. Dixon, [[arXiv:hep-ph/9507214](#)].
- [95] P. Nogueira, J. Comput. Phys. **105** (1993) 279.
- [96] T. Binoth, M. Ciccolini and G. Heinrich, [[arXiv:hep-ph/0601254](#)].
- [97] T. Hahn, Comput. Phys. Commun. **140** (2001) 418 [[arXiv:hep-ph/0012260](#)].
- [98] <http://hepforge.cedar.ac.uk/lhapdf/>
- [99] F. A. Berends, R. Pittau and R. Kleiss, Nucl. Phys. B **424** (1994) 308 [[arXiv:hep-ph/9404313](#)].
- [100] R. Kleiss and R. Pittau, Comput. Phys. Commun. **83** (1994) 141 [[arXiv:hep-ph/9405257](#)].
- [101] N. Kauer and D. Zeppenfeld, Phys. Rev. D **65** (2002) 014021 [[arXiv:hep-ph/0107181](#)].

-
- [102] N. Kauer, Phys. Rev. D **67** (2003) 054013 [[arXiv:hep-ph/0212091](#)].
- [103] <http://minami-home.kek.jp/>
- [104] S. Heinemeyer, W. Hollik and G. Weiglein, Comp. Phys. Commun. **124** (2000) 76; M. Frank, S. Heinemeyer, W. Hollik and G. Weiglein, [[arXiv:hep-ph/0202166](#)].
- [105] S. Dawson, Nucl. Phys. B **359** (1991) 283.
- [106] A. Djouadi, M. Spira and P. M. Zerwas, Phys. Lett. B **264** (1991) 440.
- [107] M. Spira, A. Djouadi, D. Graudenz and P. M. Zerwas, Nucl. Phys. B **453** (1995) 17 [[arXiv:hep-ph/9504378](#)].
- [108] E. W. N. Glover and J. J. van der Bij, CERN-TH-5022-88 *Presented at 23rd Rencontres de Moriond: Current Issues in Hadron Physics, Les Arcs, France, Mar 13-19, 1988*.
- [109] S. Dawson, S. Dittmaier and M. Spira, Phys. Rev. D **58** (1998) 115012 [[arXiv:hep-ph/9805244](#)].
- [110] F. Gianotti *et al.*, “Physics potential and experimental challenges of the LHC luminosity upgrade,” Eur. Phys. J. C **39** (2005) 293 [[arXiv:hep-ph/0204087](#)].
- [111] B. Mellado, W. Quayle and S. L. Wu, [arXiv:0708.2507 \[hep-ph\]](#).
- [112] U. Baur and E. W. N. Glover, Nucl. Phys. B **339** (1990) 38.
- [113] M. Czakon *et. al.*, in preparation.
- [114] M. Kobayashi and T. Maskawa, Prog. Theor. Phys. **49** (1973) 652.
- [115] U. Baur, E. W. N. Glover and J. J. van der Bij, Nucl. Phys. B **318** (1989) 106.
- [116] V. Lafage, Ph.D. thesis.
- [117] Z. Bern, L. J. Dixon and D. A. Kosower, Nucl. Phys. B **412** (1994) 751 [[arXiv:hep-ph/9306240](#)];
A. van Hameren, J. Vollinga and S. Weinzierl, Eur. Phys. J. C **41** (2005) 361 [[arXiv:hep-ph/0502165](#)].
- [118] F. Maltoni and T. Stelzer, JHEP **0302** (2003) 027 [[arXiv:hep-ph/0208156](#)].
- [119] G. J. van Oldenborgh, Ph.D. thesis;
G. J. van Oldenborgh and J. A. M. Vermaseren, Z. Phys. C **46** (1990) 425.

Danksagung

An dieser Stelle möchte ich mich bei all jenen bedanken, die zum Gelingen dieser Arbeit beigetragen haben.

Mein ganz besonderer Dank gilt Dr. Thomas Binoth und Dr. Nikolas Kauer für die hervorragende Betreuung dieser Arbeit. Ohne ihre Unterstützung und große Geduld in zahlreichen Diskussionen während meiner Promotionszeit wäre die vorliegende Arbeit in dieser Form nicht möglich gewesen. Thomas danke ich außerdem dafür, dass er mich auch in Edinburgh nicht vergessen hat und mir einen Forschungsaufenthalt in Edinburgh ermöglichte. Bei Nikolas möchte ich mich zusätzlich für die kompetente Unterstützung bei diversen Programmierproblemen, für das intensive Korrekturlesen dieser Arbeit und für hilfreiche Tipps jenseits promotionsspezifischer Fragen bedanken.

Mein Dank geht auch an Professor Dr. Reinhold Rückl, an dessen Lehrstuhl es mir ermöglicht wurde, mein großes Interesse an der Teilchenphysik zu verfolgen und mir durch die Teilnahme an Workshops und Konferenzen die Möglichkeit gab, meinen wissenschaftlichen Horizont zu erweitern.

Brigitte Wehner danke ich für die kompetente Unterstützung in allerlei Verwaltungsangelegenheiten.

Bei meinen Zimmerkollegen Radja Boughezal und Cristoph Uhlemann bedanke ich mich für die nette Arbeitsatmosphäre und die vielen kleinen Diskussionen.

Schließlich bedanke ich mich für die finanzielle Unterstützung durch den Graduiertenkolleg 1147 *Theoretische Astrophysik und Teilchenphysik* und der Universität Edinburgh, die mir zwei mehrmonatige Forschungsaufenthalte in Edinburgh ermöglichten.

Erklärung

Hiermit erkläre ich, dass ich die vorliegende Arbeit selbständig verfasst und keine anderen als die angegebenen Hilfsmittel verwendet habe.

Würzburg, den 28.08.2007

Stefan Karg

Lebenslauf

Persönliche Daten

Vor- und Zuname: Stefan Karg
Geburtsdatum: 16.10.1977
Geburtsort: Neumarkt i. d. OPf
Familienstand: ledig
Staatsangehörigkeit: deutsch

Ausbildung

08/1984 - 07/1988 Grundschule Neumarkt
08/1988 - 06/1997 Willibald-Gluck Gymnasium, Neumarkt
06/1997 Allgemeine Hochschulreife
07/1997 - 08/1998 Zivildienst
10/1998 - 07/2004 Diplomstudium der Physik an der Universität Würzburg
08/2001 - 08/2002 Studium der Physik an der Rutgers State University of New Jersey,
USA
08/2002 Master of Science
07/2004 Diplom im Fach Physik
08/2004 - 09/2007 Promotionsstudium im Fach Physik an der Universität Würzburg